

AFAL-TR-76-56

ED A 03028

INVESTIGATION OF OPTICAL AND ELECTRICAL PROPERTIES OF WIDE BAND GAP MATERIALS

✓ UNIVERSITY OF DAYTON
PHYSICS DEPARTMENT
DAYTON, OHIO

JUNE 1976



TECHNICAL REPORT AFAL-TR-76-56
FINAL REPORT FOR PERIOD - JUNE 1972 - DECEMBER 1975

Approved for public release; distribution unlimited

AIR FORCE AVIONICS LABORATORY
AIR FORCE WRIGHT AERONAUTICAL LABORATORY
AIR FORCE SYSTEMS COMMAND
WRIGHT-PATTERSON AIR FORCE BASE, OHIO 45433

NOTICE

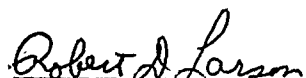
When Government drawings, specifications, or other data are used for any purpose other than in connection with a definitely related Government procurement operation, the United States Government thereby incurs no responsibility nor any obligation whatsoever; and the fact that the government may have formulated, furnished, or in any way supplied the said drawings, specifications, or other data, is not to be regarded by implication or otherwise as in any manner licensing the holder or any other person or corporation, or conveying any rights or permission to manufacture, use, or sell any patented invention that may in any way be related thereto.

This report has been reviewed by the Information Office (OI) and is releasable to the National Technical Information Service (NTIS). At NTIS, it will be available to the general public, including foreign nations. This technical report has been reviewed and is approved for publication.



DR. Y. S. PARK
Project Scientist

FOR THE COMMANDER



ROBERT D. LARSON, Chief
Electronic Research Branch
Electronic Technology Division
AF Avionics Laboratory

Copies of this report should not be returned unless return is required by security considerations, contractual obligations, or notice on a specific document.

UNCLASSIFIED

SECURITY CLASSIFICATION OF THIS PAGE (When Data Entered)

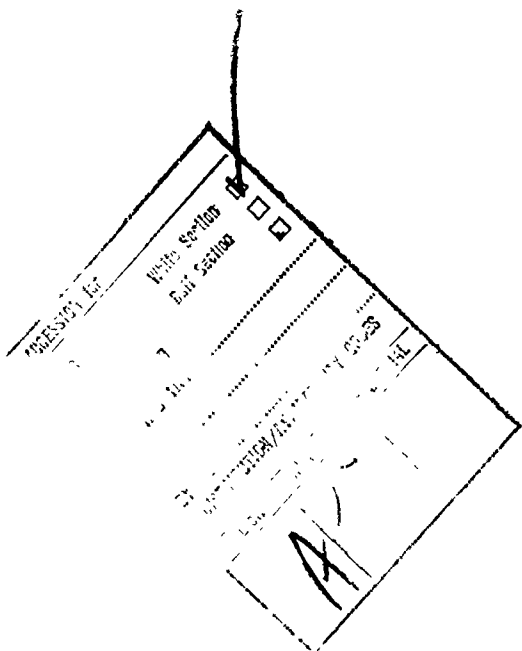
REPORT DOCUMENTATION PAGE		READ INSTRUCTIONS BEFORE COMPLETING FORM
1. REPORT NUMBER 181 AFAL-TR-76-56	2. GOVT ACCESSION NO.	3. RECIPIENT'S CATALOG NUMBER
4. TITLE (and Subtitle) INVESTIGATION OF OPTICAL AND ELECTRICAL PROPERTIES OF WIDE BAND GAP MATERIALS		5. TYPE OF REPORT & PERIOD COVERED FINAL REPORT (Jun 1972 - Dec 1975)
6. AUTHOR(s) Phil Won Yu, Samuel Faile, Hans Stocker, James Schneider		7. CONTRACT OR GRANT NUMBER(s) F33615-72-C-2114
8. PERFORMING ORGANIZATION NAME AND ADDRESS Air Force Avionics Laboratory (AFAL/DHR) Wright-Patterson AFB, OH 45433		9. PROGRAM ELEMENT, PROJECT, TASK AREA & WORK UNIT NUMBERS 61102F 78850666
10. CONTROLLING OFFICE NAME AND ADDRESS Air Force Avionics Laboratory (AFAL/DHR) Wright-Patterson AFB, OH 45433		11. REPORT DATE June 1976
12. MONITORING AGENCY NAME & ADDRESS (if different from Controlling Office)		13. NUMBER OF PAGES 152
		14. SECURITY CLASSIFICATION OF THIS REPORT 15a. DECLASSIFICATION/ DOWNGRADING SCHEDULE
16. DISTRIBUTION STATEMENT (of this Report) Approved for Public Release; Distribution Unlimited		
17. DISTRIBUTION STATEMENT (of the abstract entered in Block 20, if different from Report)		
18. SUPPLEMENTARY NOTES		
19. KEY WORDS (Continue on reverse side if necessary and identify by block number) Chalcopyrite materials (I-III-VI ₂) HgS GaAs Luminescence and absorption Electroluminescence Photovoltaic Detection Crystal Growth Electrical Transport Properties		
20. ABSTRACT (Continue on reverse side if necessary and identify by block number) This report concerns research on the optical and electrical properties of I-III-VI ₂ chalcopyrite compounds, HgS, ZnSe, and GaAs. Seventeen of the I-III-VI ₂ compounds were grown by melt-growth and vapor-phase method. HgS crystals were mainly grown by a modified iodine transport technique with small addition of NH ₄ Cl. Anomalous temperature dependence of energy gaps in I-III-VI compounds having d-electron was determined for AgGaS ₂ and CuInSe ₂ from photoluminescence, absorption, and reflection and was explained by the temperature dependent p-d		

401 556
167

UNCLASSIFIED

SECURITY CLASSIFICATION OF THIS PAGE(When Data Entered)

hybridization. Broad-band luminescence dominating in AgGaS_2 and CuInSe_2 was influenced by heat-treatment, which indicates that intrinsic defects are responsible for the band. The electrical transport measurements lead to an understanding of the role of intrinsic defects in conduction mechanisms in CuGaS_2 , AgGaS_2 , CuInSe_2 , and ZnSe . Homojunction diode in CuInSe_2 was prepared by both diffusion and implantation techniques using Cd, Br, Zn, and Cl. The p-n junction showed efficient electroluminescence as well as efficient photodetection characteristics. In GaAs, the oscillatory photoconductivity was observed.



UNCLASSIFIED

SECURITY CLASSIFICATION OF THIS PAGE(When Data Entered)

PREFACE

This is the final report covering the work performed under Contract F33615-72-C-2114 project and task number 78850666 by the University of Dayton between June 1972 and December 1975. The research was performed for the Solid State Research Laboratory of the Aerospace Research Laboratory and the the Electronic Research Branch of the Air Force Avionics Laboratory, Wright-Patterson Air Force Base, Ohio with the technical monitor of Dr. Y. S. Park, (AFAL/DHR).

The final report is the result of the efforts of research physicists Dr. Phil Won Yu, Dr. Samuel Faile and Dr. Hans Stocker. Dr. Yu was responsible for electrical transport measurements, optical characterization of the materials and device properties. Dr. Faile was mainly involved with material synthesis and single crystal growth of I-III-VI₂ compounds and HgS. Dr. Stocker was primarily concerned with ZnS electroluminescence study and GaAs photoconductivity. Dr. Richard Harmer, Research Ceramist and Assistant Professor of Materials Engineering, spent part-time on the project with efforts directed at analysis, preparation, and orientation of crystals. Some of I-III-VI₂ compounds (CuAlS₂, AgGaS₂, and CuGaS₂) were grown by Dr. J. Manthuruthil.

This work has been highlighted by presentation of results at conferences and through publication of technical papers. These publications are listed in References and Bibliography at the end of this final report.

TABLE OF CONTENTS

SECTION	PAGE
I INTRODUCTION	1
II THE CHALCOPYRITE STRUCTURE AND CRYSTAL GROWTH	4
1. CHALCOPYRITE COMPOUNDS (I-III-VI ₂ MATERIALS)	4
A. Chalcopyrite Structure	4
B. Electronic Structure	8
C. Technological Interest of I-III-VI ₂ Materials . .	12
2. CRYSTAL GROWTH OF I-III-VI ₂ COMPOUNDS	15
3. CRYSTAL GROWTH OF HgS	23
A. Background	23
B. Iodine Transport Method	25
C. Modified Iodine Transport Method	29
D. Hydrothermal Method	35
E. Other Crystal Growth	36
4. ANALYSIS OF PREPARED I-III-VI ₂ COMPOUNDS	37
A. Debye-Scherrer Powder Patterns	37
B. Single Crystal Orientation	40
III OPTICAL PROPERTIES	42
1. TEMPERATURE DEPENDENCE OF ENERGY GAP IN IN AgGaS ₂ and CuInSe ₂	42
A. AgGaS ₂	42
B. CuInSe ₂	49
2. LUMINESCENCE OF AgGaS ₂	51
A. Broad Emission Bands	51
B. Bound Exciton and Phonons	53
3. OPTICAL ROTATION IN AgGaS ₂	60
4. DONOR-ACCEPTOR PAIR BAND IN CuInSe ₂	62
5. ELECTROLUMINESCENCE AND PHOTOVOLTAIC DETECTION IN CuInSe ₂	73
A. Cd-diffused CuInSe ₂ Junction Diodes	73
B. Br, Cl, Cd and Zn Implanted Junctions	76

TABLE OF CONTENTS

SECTION	PAGE
6. PHOTOCONDUCTIVITY IN SEMIINSULATING GaAs	85
7. D. C. ELECTROLUMINESCENCE IN ZnS	90
IV ELECTRICAL TRANSPORT PROPERTIES	94
1. HIGH RESISTIVITY HALL SYSTEM	94
2. ELECTRICAL PROPERTIES OF CuGaS ₂	94
A. Resistivity and Hall Coefficient.	96
B. Concentration Dependence of Activation Energy..	102
C. Mobility	106
3. ELECTRICAL PROPERTIES OF AgGaS ₂	112
4. P-TYPE CONDUCTION IN UNDOPED ZnSe	114
V APPENDIX A COMPUTER PROGRAM; POWDER DIFFRACTION PATTERN . .	123
APPENDIX B CALCULATED X-RAY DIFFRACTION PATTERNS.	127
A. CuGaS ₂	127
B. AgGaS ₂	130
REFERENCES.	133
BIBLIOGRAPHY.	140

LIST OF ILLUSTRATIONS

FIGURE	PAGE
1 Formation of Ternary I-III-VI ₂ and II-IV-V ₂ Compounds from Their Binary II-VI and III-V Analogs	5
2 Structure of Cubic Zinc Blende and of Tetragonal ABC ₂ Chalcopyrite	7
3 Chalcopyrite Brillouin Zone Imbedded into that of Zinc Blende	9
4 Valence Band Structure of Zinc Blende and II-IV-V ₂ Chalcopyrite Compounds at Γ . With Spin-Orbit Coupling Included, the A and C Transitions also Become Allowed for $E \perp C$ and $E \parallel C$, Respectively	11
5 Trends in Band Gap Energy by Elemental Constituent	13
6 Location of Container in Furnace	17
7 I-III-VI ₂ Compounds Obtained from Various Runs (1 div=1 mm)	20
8 Iodine Transport of HgS. The Source Material in the Pyrex Tube is Composed of 150 g HgS and 3 g I ₂	27
9 A Typical Time-Temperature Relation for the Modified Iodine Transport Method	31
10 HgS Crystals from Various Run with the Modified Iodine Transport Method (1 div = 1 mm)	32
11 HgS Crystals from a Run Involving Large Amount of NH ₄ Cl and Iodine Enclosed in a Double Walled Tube (1 div = 1 mm)	33
12 The Reflectivity, Photoluminescence and Absorption Spectra of AgGaS ₂ Near the Band Edge at $T = 4.2$ °K. All of the Spectra Were Obtained by the Densitometer Tracing	43
13 The Temperature Dependence of the Position of the Main Exciton Reflectivity Maximum, the Three Emission Peaks (A-Exciton, A'-Exciton and P-Line) and the Main Absorption Peak	46
14 The Absorption Coefficient α_{\perp} Versus the Temperatures at 7, 150, 200 240 and 300 °K	47
15 The Lowest Energy Gap of AgGaS ₂ in the Temperature Range 4.2-300 °K	48

LIST OF ILLUSTRATIONS

FIGURE	PAGE
16 Luminescence Spectra (a)(b) from p-Type Crystals Grown from the Stoichiometric Melt and (c) from n-Type Crystals	50
17 Broad-Band Emission Spectra of AgGaS_2 at 4.2 and 77 $^{\circ}\text{K}$ (a) As-Grown Crystals Often Show the Bands at ~ 5000 and ~ 6800 \AA . The 6800 \AA Band is Quenched by Annealing in a Sulfur Atmosphere. (b) Successive Annealing in a Sulfur Atmosphere and Vacuum Results in the Band at ~ 5500 \AA	52
18 4.2 $^{\circ}\text{K}$ Photoluminescence Emission Spectrum of a Broad Band Peaking at ~ 5000 \AA Together with Other Emission Peaks. Many Phonon Lines are Superimposed on the Broad Band. The Repeat Interval for the Phonon Structure is Indicated by w_L (43.3 meV).	54
19 4.2 $^{\circ}\text{K}$ Photoluminescence Emission Spectra for a Phonon Structure in the Broad Band. The A Line is a Non-Phonon Line at 4775 \AA . The Phonon Energies are Indicated by X and Y	57
20 Raman Scattering from AgGaS_2	59
21 The Absorption of a AgGaS_2 Sample 0.13 mm Thick Placed Between Crossed Polarizers at 4.9 $^{\circ}\text{K}$	61
22 The Optical Rotatory Dispersion for AgGaS_2 Sample Used in Fig. 21	63
23 Effect of Excitation Intensity on the Band Position at 4.2 $^{\circ}\text{K}$. The Fractional Excitation Intensities are Shown on Each Spectrum. Maximum Power is 240 mW from the 6471 \AA Line of a Kr Laser. Emission Intensity Decreases with the Intensity of Excitation. Each Emission Spectrum Has Been Normalized	65
24 Excitation Intensity vs. Band Peak Energy. β is the Energy Change Per Decade of Excitation Intensity	67
25 Effect of Temperature on the Band. D - A \equiv Donor-Acceptor Pair Band. F - B \equiv Free Electron to Bound Hole to Acceptor Transition	68

LIST OF ILLUSTRATIONS

FIGURE	PAGE
26 Logarithmic Current-Voltage Characteristics for a Typical Sample at $T = 300, 275, 235$ °K for both Forward and Reverse Bias. Solid Lines are the Fitted Curves for the Relations $I \propto V^m$ for the Forward Bias, Where $m = 1$ for the Low-Voltage Region and $m = 3$ for the High-Voltage Region.	75
27 Spectral Dependence of the Photovoltaic Quantum Efficiency for a $\text{CuInSe}_2:\text{Cd}$ Homojunction. For Comparison Purposes, the Efficiency of a Commercial Si Detector is Presented.	77
28 The Room-Temperature Current-Voltage Characteristics of the p-n Junctions Prepared by Implanting Br , Cl , Cd and Zn	80
29 Electroluminescence Spectra Obtained from the p-n Junctions Prepared by Implanting Br , Cd , Cl and Zn for a Current of 10 mA at 77 °K.	81
30 Dependence of Relative Electroluminescence Intensity Upon the Forward Current. The Dotted Line Indicates the Relation $L \propto I^n$, with $n = 2$	83
31 Spectral Dependence of the Photovoltaic Quantum Efficiency for a $\text{CuInSe}_2:\text{Cd}$ Homojunction Having a Reverse Bias of 5 V.	84
32 Photoconductive Spectral Response Per Unit Photon for a Sample of Semi-Insulating GaAs at $T = 23$ °K	86
33 Wavenumber of the Minima vs the Number of the Minima for Three Samples of Semiinsulating GaAs.	87
34 Photoconductive Response of Six Samples at $T = 23$ °K	91
35 D. C. Electroluminescence Spectrum of Mn-Doped ZnS	92
36 Guarded Hall System Employing Three Unity Gain Amplifiers A_1 , A_2 , and A_3 . A_m is an Electrometer Ammeter Operated in a Feedback Mode.	95

LIST OF ILLUSTRATIONS

FIGURE	PAGE
37 Temperature Dependence of the Resistivity of the Samples Heat Treated at Different Temperatures as Shown in Table 8. M, Indicates the Melt-Grown Crystals. I, is for the Crystals Grown from the Vapor	98
38 Terperature Dependence of the Hole Concentration of the Samples Heat Treated at Different Temperatures as Shown in Table 8. The Symbols Represnt Experimental Points, While the Solid Lines Represent the Fit as Discussed in Text	99
39 The Acceptor Concentration vs the Inverse of Heat-Treatment Temperatu... The Solid Line Yields ~0.68 eV as a Forme on Energy of Cu Vacancies	103
40 The Acceptor Ionization Energy vs the Cube of Acceptor Concentration. The Dotted Line is Fitted for the Lower Activation Energies Than the Hydrogenic Acceptor Level (~0.12 eV) with $\beta = 2.4 \times 10^{-8}$ eV cm as Discussed in Text	105
41 The Temperature Dependence of the Experimental Hall Mobility for Selected Samples	107
42 The Hall Mobility vs Temperature for the Sample No. I66 with Various Scattering Mechanisms, $N_A = 2.4 \times 10^{18}$ cm ⁻³ and $N_D = 4.2 \times 10^{17}$ cm ⁻³	109
43 The Hall Mobility vs Temperature for the Sample No. IAS with Various Scattering Mechanisms, $N_A = 1.4 \times 10^{17}$ cm ⁻³ and $N_D = 6.8 \times 10^{16}$ cm ⁻³	110
44 Resistivity, Carrier Concentration, and Mobility as a Function of Reciprocal Temperature for a Typically As-Grown P-Type AgGaS ₂ Specimen. The Electrical Parameters were Also Measured on the Same Specimen Subsequent to Vacuum Annealing and Sulfur Baking.	113

LIST OF ILLUSTRATIONS

FIGURE	PAGE
45 Resistivity as a Function of Reciprocal Temperature for p-Type As-Grown AgGaS_2 Grown from the Melt Having a Shallow Acceptor.	115
46 Resistivity vs the Inverse of Temperature for a n-Type Samples Before the Heat-Treatment.	117
47 Hole Concentration and Resistivity vs the Inverse of Temperature for Sample No. I. The Solid Line Shows the Fitted Values with $E_A = 0.67$ eV, $N_A = 3.7 \times 10^{15} \text{ cm}^{-3}$, $N_D = 1.3 \times 10^{14} \text{ cm}^{-3}$, and $N_V/g = 1.2 \times 10^{14}$	118
48 Hole Hall Mobility vs the Inverse of Temperature After the Heat Treatment	119
49 Acceptor Level vs the Heat Treating Temperature.	120
50 Resistivity vs the Inverse of Temperature for Samples Nos. 2 and 3	122

LIST OF TABLES

TABLE	PAGE
1 ENERGY GAP AND VALENCE BAND PARAMETERS, in eV, OF TERNARY SULFIDES AND SELENIDES (300 °K)	14
2 VARIOUS TECHNICAL ASPECTS OF I-III-VI ₂ MATERIALS	16
3 SUMMARY OF CRYSTAL GROWTH FOR I-III-VI ₂ COMPOUNDS.	19
4 LATTICE PARAMETERS OF I-III-VI ₂ CRYSTALS	41
5 ENERGY POSITION OF VARIOUS EMISSION LINES AT 4.2 °K. THE ENERGY OF A LINE IS 2.59622 eV. X AND Y CORRESPOND TO TWO PHONON ENERGIES.	55
6 BAND-PEAK ENERGY VS THE HALF-WIDTH AND THE ENERGY SHIFT PER DECADE OF CHANGE OF EXCITATION INTENSITY (β) IN P-TYPE CRYSTALS GROWN UNDER AN EXCESS Se ATMOSPHERE (T = 4.2 °K)	70
7 SAMPLES OF Cr-DOPED GaAs	89
8 SAME ROOM-TEMPERATURE ELECTRICAL CHARACTERISTICS OF THE SAMPLES MEASURED AT DIFFERENT HEAT- TREATMENT TEMPERATURE.	97
9 LEAST-SQUARE-FITTED VALUES FOR IMPURITY DENSITY. ACTIVATION ENERGY, AND COMPENSATION RATIO	101

SECTION I

INTRODUCTION

This work reports on the results of our efforts directed toward an investigation of electrical and optical properties of semiconducting materials. The investigated crystals are I-III-VI₂ semiconductors with chalcopyrite structure, HgS, II-VI compounds, and GaAs. The study includes the investigation of possible uses of the materials in the area of injection luminescence, infrared nonlinear optics, photodetection. We give both theoretical and experimental results on growth techniques, material problems, optical and electrical properties, and also present device properties.

Anomalous temperature dependence of energy gaps in I-III-VI₂ compounds containing d-electron noble metals was explained, for AgGaS₂ and CuInSe₂, by the temperature dependent p-d hybridization; the lowest energy gap increases with the temperature from 4.2°K to ~100°K and decreases with the further increase of temperature. Below ~80°K the temperature coefficient of the energy gap is $+6 \times 10^{-5}$ eV/°K and $+6.8 \times 10^{-5}$ eV/°K, respectively, for AgGaS₂ and CuInSe₂.

Broad-band luminescence dominating in AgGaS₂ and CuInSe₂ at lower temperatures is influenced by heat-treatments, which indicates that intrinsic defects are responsible for the band. In CuInSe₂, the behavior of low temperature spectra of melt-grown p-type and Cd-implanted crystals with changes in temperature and excitation intensity have been investigated. The band was observed to shift to higher energy as the excitation intensity or temperature was increased. The spectral characteristics are explained by the presence of an acceptor level

($E_A = 85 \pm 2$ meV) and a donor level ($E_D = 65 \pm 2$ meV) and by compensation-dependent band shift in the p-type crystals. Acceptors and donors responsible for the pair band appear to be Cu and Se vacancy. In AgGaS_2 , a series of sharp emission lines was found to be superimposed on the broad band peaking at ~ 5000 Å. The series of emission lines are attributed to phonon-assisted transitions involving an unidentified impurity or defect.

The electrical transport measurements lead to an understanding of the role of intrinsic defects in conduction mechanism. Deep acceptor levels (0.65 - 0.75 eV) dominating in p-ZnSe are attributed to a zinc or a zinc vacancy complex. The presence of both deep acceptor and donor levels ($E_A = 0.72$ eV, $E_D \approx 0.70$ eV) causes a semiinsulating state in AgGaS_2 . Acceptor and donor appear to be Ag-vacancy and S-vacancy, respectively. In CuGaS_2 , an analysis of the hole concentration showed that acceptor ionization energy increases from 0.073 to 0.39 eV with the decrease of the acceptor concentration. The effective mass of the hole in CuGaS_2 was 0.69 me. The mobility shows the dominance of lattice scattering through a deformation potential. In GaAs, we observed the oscillatory photoconductivity with a period of 20.9 meV.

CuInSe_2 can readily be made either p- or n-type. Homojunction diodes have been prepared by both diffusion and implantation techniques using Cd, Br, Zn and Cl atoms. The p-n junctions showed efficient electroluminescence ($\lambda \approx 1.3 \mu$ at 77^0K) as well as efficient photodetection characteristics comparable to commercially available Si with more extended wavelength.

HgS single crystals with good optical quality were grown by a modified iodine transport with small addition of NH_4Cl . The sizes of these crystals of up to 4x4x2 mm indicate the effectiveness of the addition of NH_4Cl into iodine and show a promising aspect of this crystal for the non-linear optics applications.

SECTION II

THE CHALCOPYRITE STRUCTURE AND CRYSTAL GROWTH

1. CHALCOPYRITE COMPOUNDS (I-III-VI₂ MATERIALS)

A. Chalcopyrite Structure

Ternary semiconductors of type I-III-VI₂ are the logical extension of the zinc blende semiconductor families. These ternary compounds are formed from their binary parents by replacing the group-II cations in a binary compound with an equal number of group-I and -III. This substitution, leading to the "ternary generation" of semiconductors, is illustrated in Fig. 1. It is immediately seen that there will be many more members of the ternary semiconductor families than there are in the binary cases. Thus, all compounds formed by combination of the elements Cu, Ag; Al, Ga, In; S, Se, Te are known to exist chemically, leading to 18 ternary I-III-VI₂ chalcogenides.

The lattice structure, common to this large family of semiconductors, is D_{2d}¹² (I $\bar{4}2d$). It derives its name from the isomorphous mineral chalcopyrite, CuFeS₂, which is a semimetallic antiferromagnet. The chalcopyrite-lattice forms a tetragonal superlattice of the cubic zinc blende structure, T_d² (F $\bar{4}3m$). Fig. 1 also shows another ternary family, II-IV-V₂ compounds. These compounds are the ternary analogs of the III-V binary compounds as described with the I-III-VI₂ compounds.

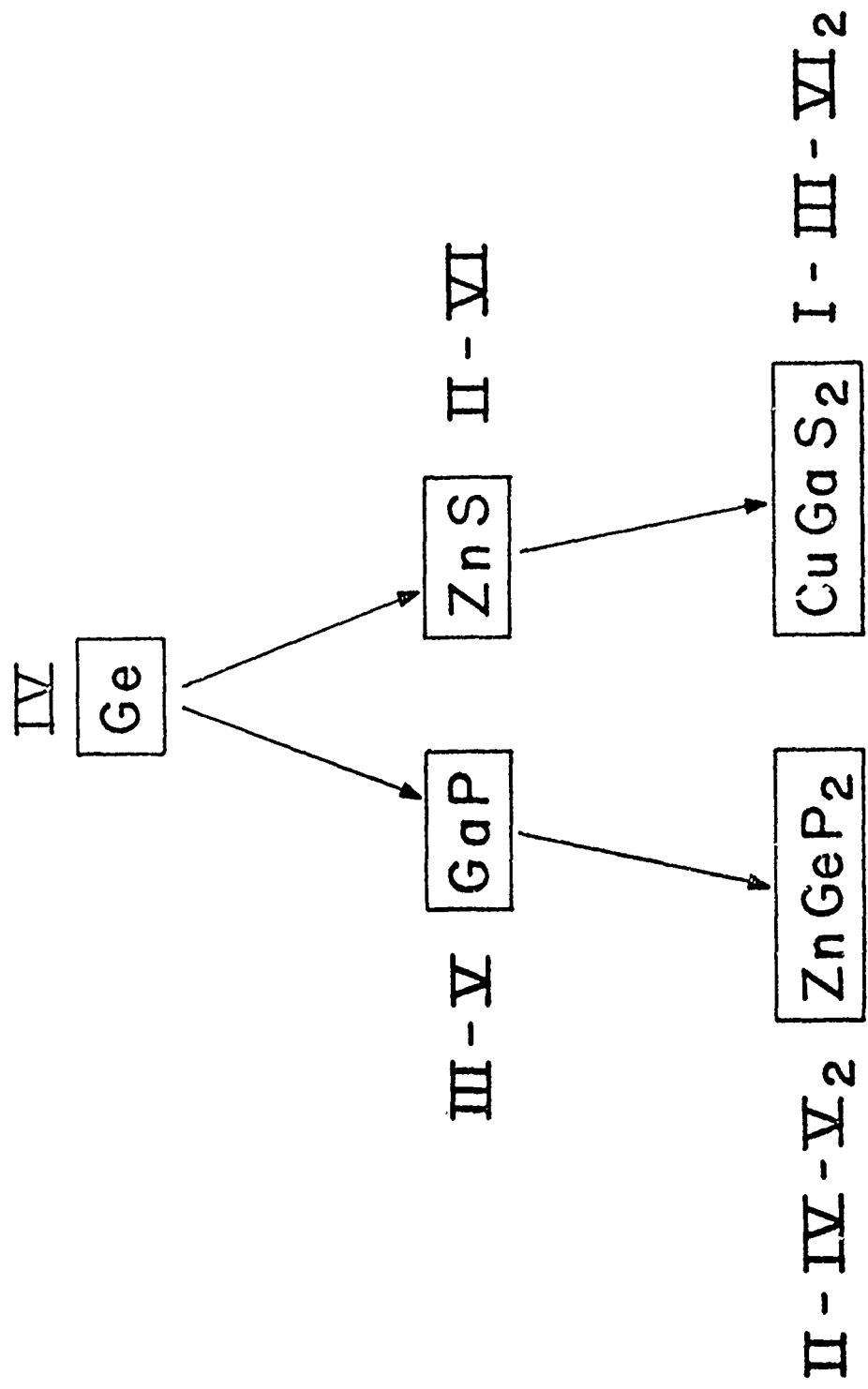


Figure 1. Formation of ternary I-III-VI₂, and II-IV-V₂ compounds from their binary III-VI and III-V analogs.

Research on these ternary materials is well motivated, both from physical and applicational points of view. The close resemblance of the chalcopyrite-structure to that of zinc blende allows, in many cases, an almost quantitative prediction of the physical properties of chalcopyrite compounds from those of the well-understood binary parents. This fact is quite fascinating and may lead to a more detailed understanding about the nature of the chemical bond in tetrahedrally coordinated crystals.

We have already mentioned that the crystal structure common to I-III-VI₂ semiconductors is that of the tetragonal chalcopyrite lattice. It belongs to the nonsymmorphic space group D_{2d}¹² which is a subgroup of the zinc blende space group T_d². Its point group is D_{2d}($\bar{4}2m$).

In such an ABC₂ compound, each A- or B-metal atom is coordinated by a slightly tetragonally distorted tetrahedron of anions C. The point symmetry at the metal sites is therefore S₄. At the anion sites, each C-atom is coordinated by two A- and by two B-metal ligands. Consequently, the point symmetry at the anion C-sites is lower, C₂. The ordered arrangement of A- and B-atoms in the tetragonal chalcopyrite-lattice is illustrated in Fig. 2.

The tetragonal unit cell of chalcopyrite is formed by roughly doubling the zinc blende unit cell along a <100> direction. This preferred direction is the tetragonal c-axis of chalcopyrite. Whereas the tetragonal unit cell contains four formula units, there are only two in the primitive unit cell.

The doubling of the crystallographic unit cell, along the tetragonal c-axis, will lead to a reduction of the Brillouin zone of chalcopyrite

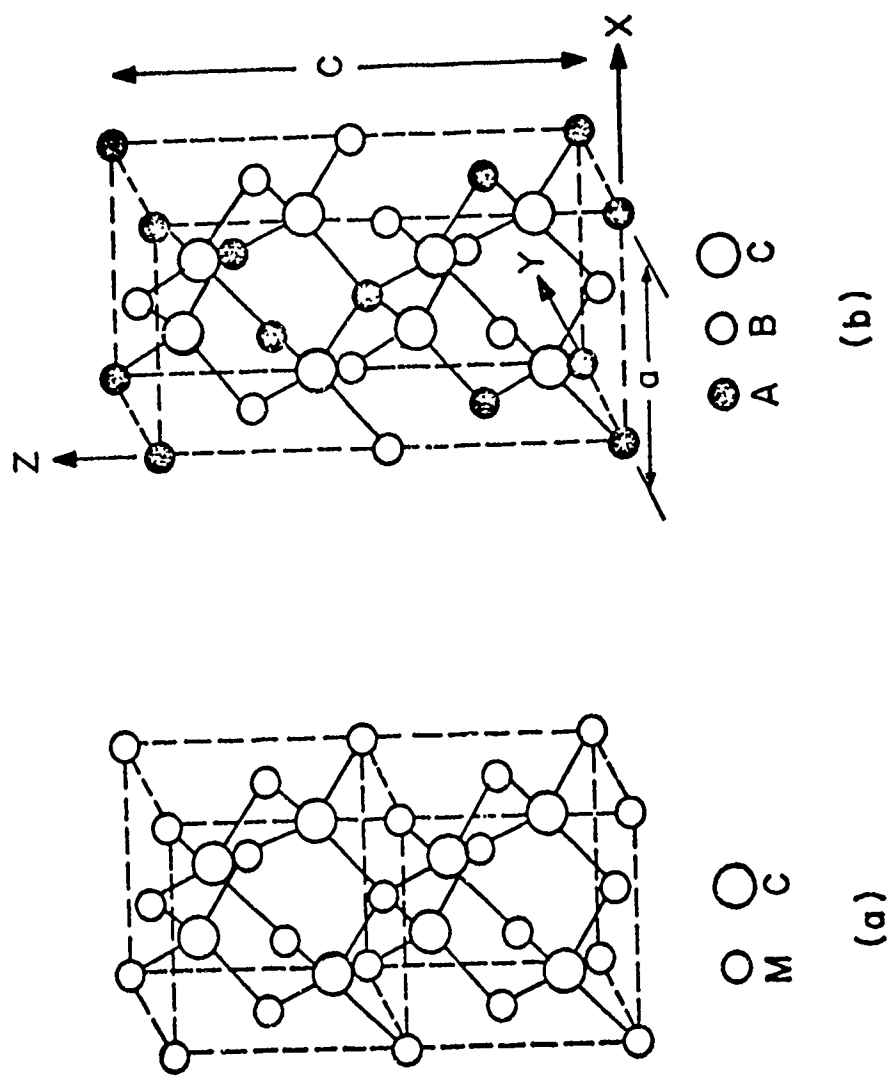


Figure 2. Structure of cubic zinc blende and of tetragonal ABC_2 chalcopyrite.

as compared to that of the cubic zinc blende-structure. This fact will account for some remarkable differences in the physical properties of ternary and binary semiconductors.

We now come to a more quantitative description of the atomic arrangement in the chalcopyrite structure. Following the conventions imposed by the International Tables of X-ray Crystallography, we place the cation of the lower charge state at the center of the tetragonal coordinate system, a_1 , a_2 , c . Thus, the positions of the atoms in an ABC_2 chalcopyrite compound are:

A:	(0, 0, 0)	(0, 1/2, 1/4)
B:	(0, 0, 1/2)	(0, 1/2, 3/4)
C:	(x, 1/4, 1/8)	(x, 3/4, 1/8)
	(3/4, x, 7/8)	(1/4, x, 7/8)

The quantity x , defining the position of the C- anions, is free parameters of the chalcopyrite structure. In the cubic zinc blende case, $A \equiv B$, we have $x = 1/4$ and $c = 2a$. In chalcopyrite structure, the parameter x deviates from its ideal value because of the difference in radii and charges of the A- and B- cation. The quality $2 - c/a$ is a measure of tetragonal distortion.

B. Electronic Structure

The simplest approximation to the energy band structure of a ternary compound is obtained by imbedding the band structures of the zinc blende binary analog into the chalcopyrite Brillouin zone.^{1,2} A comparison of the Brillouin zones is illustrated in Fig. 3.

The reciprocal lattice of chalcopyrite is, as its direct lattice, body-centered tetragonal. It is spanned by the translation vectors,

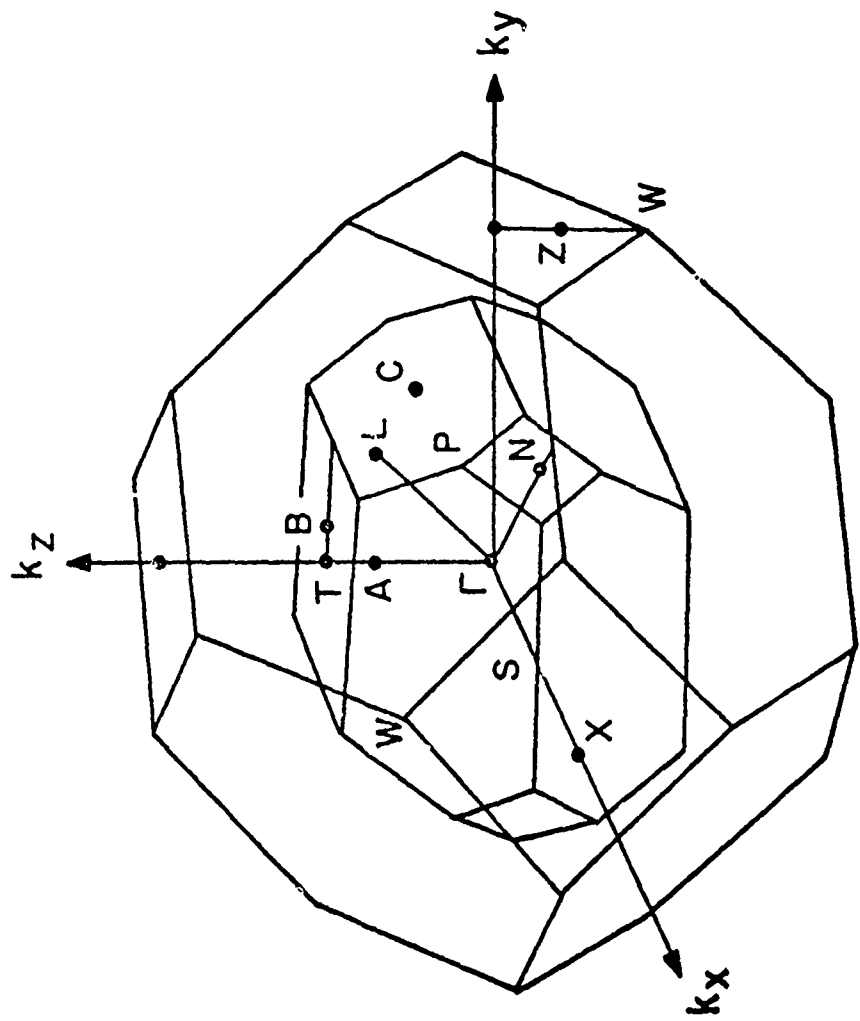


Figure 3. Chalcopyrite Brillouin zone imbedded into that of zinc blende.

$$b_1 = (0, \frac{2\pi}{a}, \frac{2\pi}{c}), b_2 = (\frac{2\pi}{a}, 0, \frac{2\pi}{c}), b_3 = (\frac{2\pi}{a}, \frac{2\pi}{a}, 0),$$

if

$$a_1 = 1/2 (-a, a, c), a_2 = 1/2 (a, -a, c), a_3 = 1/2 (a, a, -c),$$

are the primitive translations of the direct lattice. As can be seen from Fig. 3, the chalcopyrite Brillouin zone can be imbedded into that of zinc blende. Its volume is four times smaller than that of the zinc blende zone. Hence to every point of the chalcopyrite zone correspond four points of the zinc blende zone. This means that the number of energy levels (counted according to their degeneracy) associated with each point of the respective Brillouin zone is four times larger for chalcopyrite. Many high symmetry points of the zinc blende zone map into high symmetry points of the chalcopyrite zone.

Typical examples^{1,2} are:

$$\Gamma(0, 0, 0), X(0, 0, \frac{2\pi}{a}), W(\frac{2\pi}{a}, 0, \frac{\pi}{a}), W(0, \frac{2\pi}{a}, \frac{\pi}{a}) \rightarrow \Gamma(0, 0, 0)$$

$$L(\frac{\pi}{a}, \frac{-\pi}{a}, \frac{-\pi}{a}), L(\frac{\pi}{a}, \frac{-\pi}{a}, \frac{\pi}{a}), \Sigma(\frac{\pi}{a}, \frac{\pi}{a}, 0),$$

$$\Sigma(\frac{-\pi}{a}, \frac{-\pi}{a}, 0) \rightarrow N(\frac{\pi}{a}, \frac{\pi}{a}, 0)$$

$$X(\frac{2\pi}{a}, 0, 0), X(0, \frac{2\pi}{a}, 0), \Delta(0, 0, \frac{\pi}{a}), \Delta(0, 0, \frac{-\pi}{a}) \rightarrow T(0, 0, \frac{\pi}{a}).$$

Earlier studies³ have shown that the structure of the valence band maximum in a II-IV-V₂ chalcopyrite compound is simply related to the energy bands in its III-V analogs. Fig. 4 shows⁴ how the lowest direct

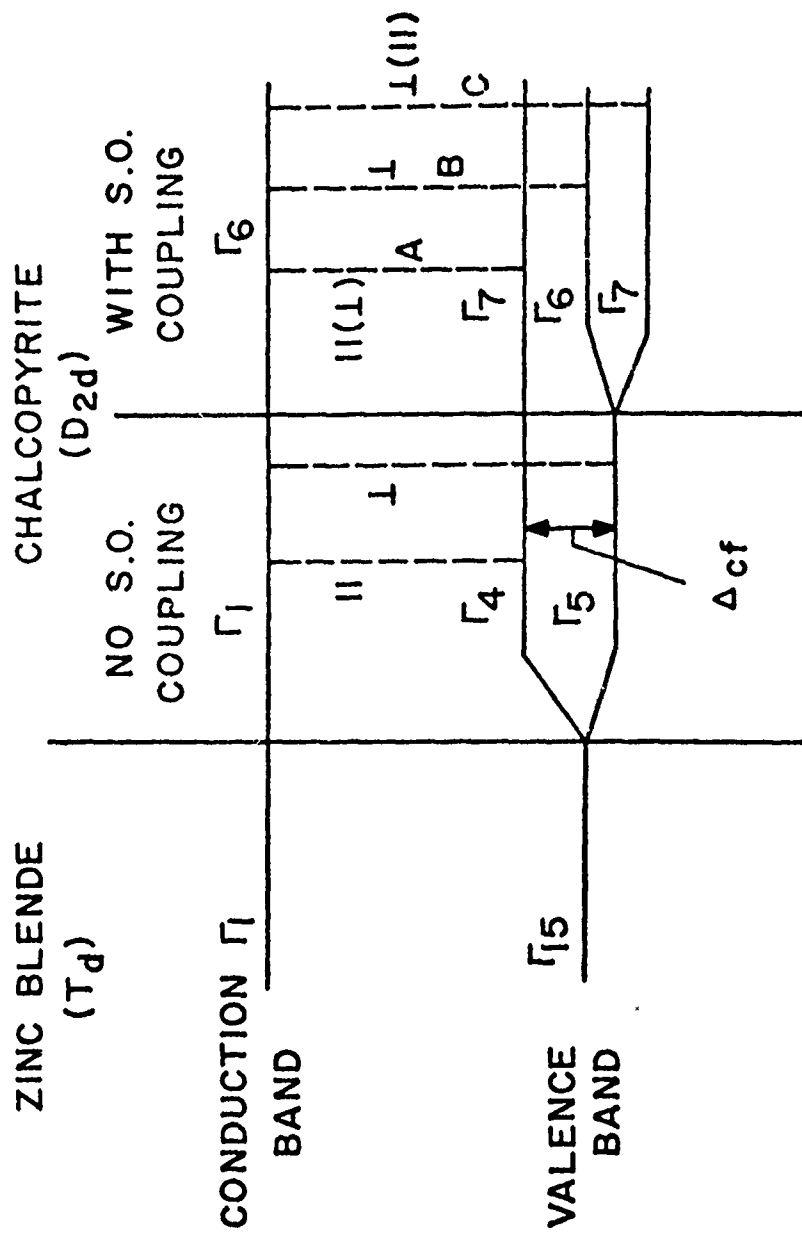


Figure 4. Valence band structure of zinc blende and $\text{II}-\text{IV}-\text{V}_2$ chalcopyrite compounds at Γ . With spin-orbit coupling included, the A and C transitions also become allowed for $E \perp c$ and $E \parallel c$, respectively.

gap of a chalcopyrite compound is related to that of a zinc blende. The combined action of spin-orbit coupling and tetragonal field completely removes the triple orbital degeneracy of the zinc blende Γ_{15} valence band. The ordering of the three spin-orbit levels originating from Γ_{15} has first been inferred from the polarization of the A, B and C transitions in the electroreflectance spectrum of CdSnP_2^4 . A very simple explanation of the valence-band splitting has been given by a quasi-cubic model.⁵ However, the uppermost valence bands of a I-III-VI₂ compound are profoundly influenced by the proximity of noble metal d-levels in the valence band.^{6,7} The direct energy gaps observed in the I-III-VI₂ compounds are low relative to the energy gaps in the II-VI analogs by amounts up to 1.6 eV, and the spin-orbit splittings of the uppermost valence band are reduced relative to binary compounds, owing to a partial cancellation of the positive spin-orbit parameters for p-levels and the negative spin-orbit parameter for d-levels. Quantitative estimates of the d-like character range from 16% to 45% over the compounds. Table I illustrates energy gap⁸ and valence band parameters. Figure 5 shows trends in band gap energy by elemental constituent in I-III-VI₂ compounds.

C. Technological Interest of I-III-VI₂ Materials

I-III-VI₂ compounds are currently of technological interest since they show promise for application in the area of visible and infrared light-emitting diodes, infrared detectors, optical parametric oscillators, up-converters, and far infrared generation. Several compounds were obtained both p- and n-type. This characteristics together with the direct nature of the band gaps generated activity in the area of heterojunction with large band gap II-VI compounds.

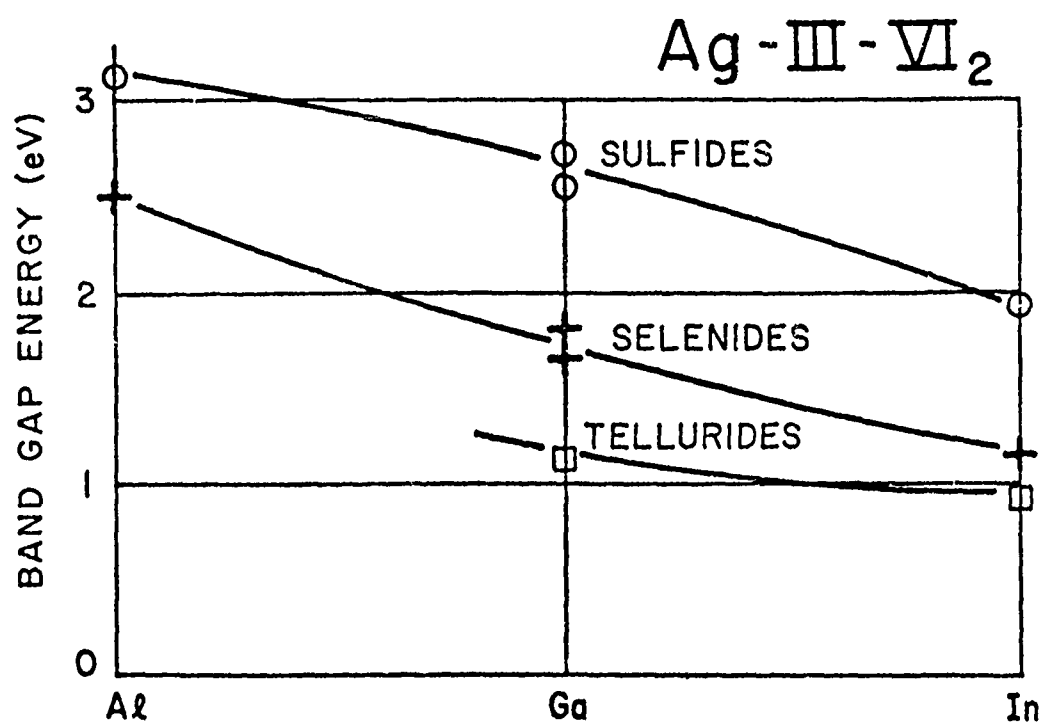
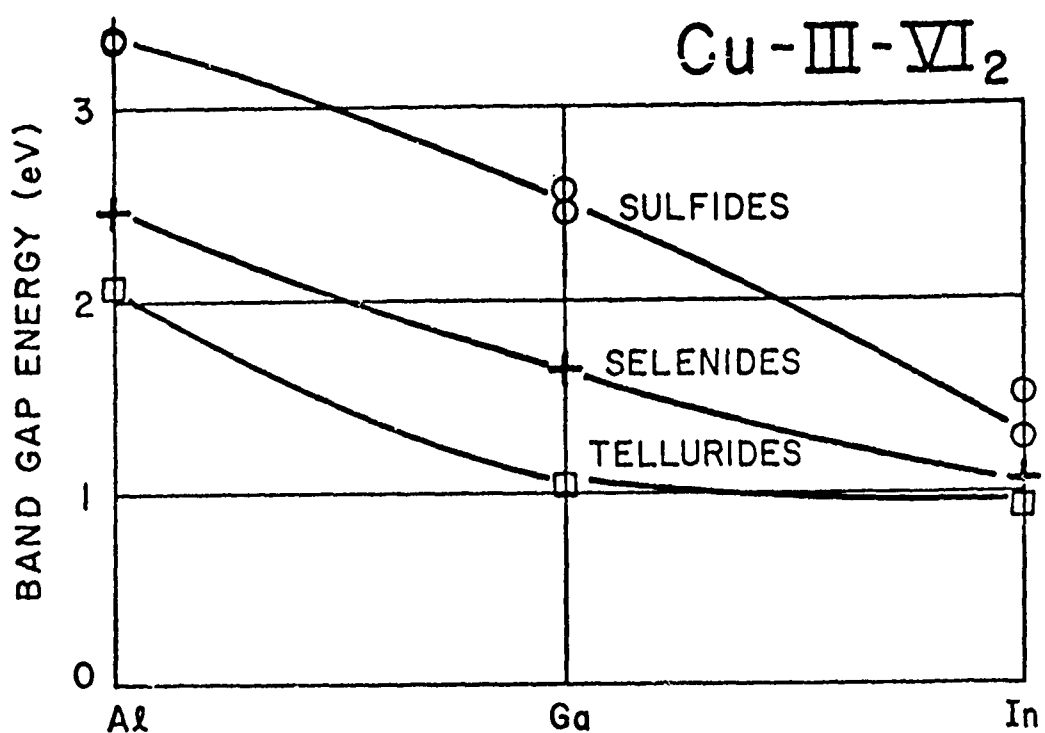


Figure 5. Trends in band gap energy by elemental constituent

TABLE 1. ENERGY GAP AND VALENCE BAND PARAMETERS, IN eV,
OF TERNARY SULFIDES AND SELENIDES (300 °K)

	E _g	Δ_{so}		d admix-ture (%)	Binary analog	E _g	Δ_{so}
		exp.	theor.				
CuAlS ₂	3.49	0	-0.08	35	—	3.17	0.07
AgGaS ₂ ⁺	2.73	0	-0.10	20	Zn _{0.5} Cd _{0.5} S	3.17	0.07
CuAlSe ₂	2.5	—	0.26	—	—		
CuGaS ₂	2.43	0	-0.06	35	ZnS	3.8	0.07
AgInS ₂	1.87	0	-0.04	20	CdS	2.53	0.07
AgGaSe ₂ ⁺	1.83	0.31	0.25	16	Zn _{0.5} Cd _{0.5} Se	2.33	0.43
CuGaSe ₂	1.68	0.23	0.28	36	ZnSe	2.8	0.43
CuInS ₂	1.53	-0.02	-0.02	45	Zn _{0.5} Cd _{0.5} S	3.17	0.07
AgInSe ₂	1.24	0.30	0.32	17	CdSe	1.85	0.43
CuInSe ₂ ⁺	1.04	0.23	0.34	34	Zn _{0.5} Cd _{0.5} Se	2.33	0.43

E_g : Energy Gap

Δ_{so} : Spin-Orbit Splitting

+ : 77 °K

Table: Ref. 8

Because of the noncubic crystal structure, I-III-VI₂ compounds are optically birefringent. Nonlinear optical interaction was possible. They have large nonlinear coefficients because these compounds are covalently bonded to a large extent. Summary of technologically interesting work is presented in Table 2.

2. CRYSTAL GROWTH OF I-III-VI₂ COMPOUNDS

The most common method of crystal growth has been crystal growth in a silica tube from a melt using as starting materials stoichiometric amounts of the elements with a purity of at least 99.999 %. The crystallization generally was achieved by cooling from a melt slowly such as 2 °C/h where the melt had a temperature gradient that caused the crystals to first form at the extreme end of the melt rather than in the middle.

There were many variations such as the use of carbon or graphite boats, the subsequent use of the resulting crystals as source material for iodine transported crystal growth of high melting compounds, and the remelting of the powdered crystals followed by cooling in a Bridgeman furnace.

For the growth of I-III-VI₂ compounds the elements were used as the starting materials with a purity of generally 99.9999 %. The metals were placed in a cleaned quartz (fused silica) boat. The S or Se was placed at the end of a cleaned fused quartz tube with a notch about 1 & 1/2 inches from the end, a diameter about one inch, a length of about 11 inches as shown in Fig. 6. The notch prevents the S or Se from running into the middle of the tube where vaporization could

TABLE 2. VARIOUS TECHNOLOGICAL ASPECTS OF I-III-VI₂ MATERIALS

Crystal	Experiment	Ref.
I-III-S ₂	Refractive Indices and Nonlinear Properties	9
I-III-Se ₂		10
AgGaS ₂	Infrared Generation (4.6 - 12 μ)	11
AgGaSe ₂	Infrared Generation (7 - 13 μ)	12
CuGaS ₂	Electroluminescence (~0.53 μ) Heterodiode with CdS	13
CuInSe ₂	Photodetection (0.5 - 1.3 μ), Heterodiode with CdS	14
CuInSe ₂	Electroluminescence (~1.3 μ), Se diffused	15
CuInSe ₂	Solar Cell (12%), Heterodiode with CdS	16
CuInSe ₂	Photodetection (0.7 - 1.2 μ), Cd diffused	17
CuInSe ₂	Electroluminescence (~1.3 μ) and Photodetection (0.7 - 1.2 μ), Cd implanted	18
CuInSe ₂	Electroluminescence (~1.3 μ), Br, Cl and Zn Implanted	To be published
CuInS ₂	Electroluminescence (~0.84 μ)	19

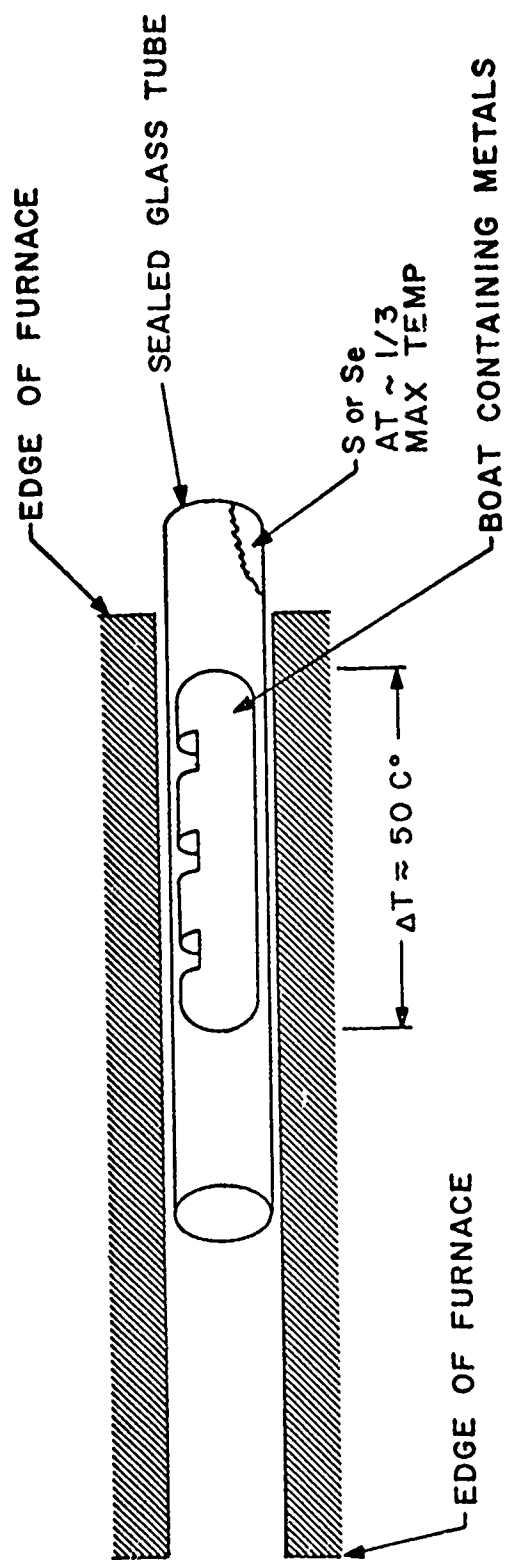


Figure 6. Location of container in furnace.

cause severe bumping. For Te, due to the low vapor pressure of Te, it is necessary to place the Te in the boat with the other metals. The compound is formed during heating where the voltaile S, Se or Te reacts with the metals in the boat.

For a typical compound such as CuInSe_2 , the temperature history would first involve the heating over a period of about seven hours where the temperature would be raised from room temperature to near 1075°C . After a soak period of about 12-15 h the material would be cooled at a rate of $10^{\circ}\text{C}/\text{h}$ to about 990°C , which is below the melting point of 980°C . The material would then be cooled to room temperature over a period of a few hours. In some instances it was necessary to use a slower cooling rate such as $5^{\circ}\text{C}/\text{h}$ or $2^{\circ}\text{C}/\text{h}$. If corrosive elements are involved such as Al or Li excessive attack would damage the fused quartz, which require either the lowering of the maximum temperature used or the use of a carbon coating of the quartz tube.

For iodine transport method, the crystals grown from the melt were crushed into powder and used as the initial charge for the vapor transport. This method involves placing the reacted material together with a small amount of iodine in an evacuated quartz ampoule and heating it in a temperature gradient, as described by Honeyman.²⁰ The volatile iodine serves as the transport agent. The temperature difference between the zone of the charge and crystallization was set at $\sim 50^{\circ}\text{C}$. The temperature of the charge zone was usually $\sim 1000\text{-}1050^{\circ}\text{C}$.

A summary of crystal growth techniques for I-III-VI₂ compounds grown is listed in Table 3. Some of the crystals grown are shown in Fig. 7.

TABLE 3. SUMMARY OF CRYSTAL GROWTH FOR I-III-VI₂ COMPOUNDS

Crystal	Melting Pt. (°C)	Method	Other Work
CuAlS ₂	~1300	M	20
CuAlSe ₂	~1200	M	21
CuGaS ₂	~1250	M, I, Br	21-23
CuGaSe ₂	~1050	M	24
CuInS ₂	~1050	M, I	21
CuInSe ₂	990	M	25
CuInTe ₂	780	M	25
CuTlSe ₂	405	M	25
AgAlSe ₂	—	M	22
AgGaS ₂	~1000	M, I	21
AgGaSe ₂	850	M	20, 25
AgGaTe ₂	720	M	25
AgInS ₂	—	M	26
AgInSe ₂	773	M	26
AgInTe ₂	680	M	25, 26
Cu _x Li _{1-x} InSe ₂	<990	M	—
Cu _x Li _{1-x} InS ₂	<~1050	M	—

M: Melt-grown

I, Br : Vapor-transported with I or Br

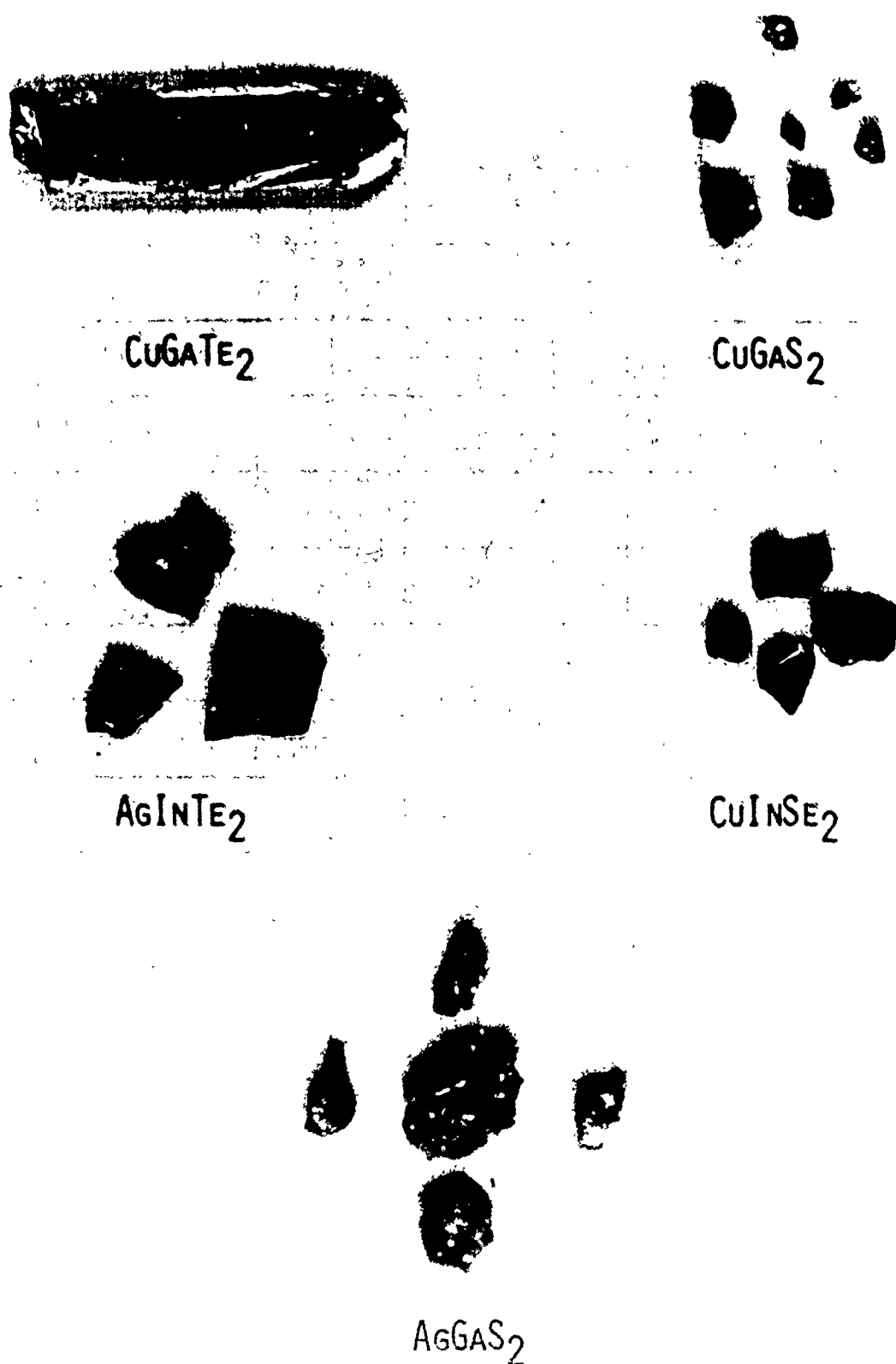


Figure 7. 1-III-VI₂ compounds obtained from various runs (1 div. = 1 mm).

CuInSe_2 was prepared both p- and n-type. P-materials were usually grown using about 0.1 mole of stoichiometric amounts of the element plus 2~3 g excess Se. A frequent problem was the reaction of the Se beads prior to use during storage with nitrogen producing a reddish powder contaminant. The higher pressure caused by the nitrogen resulted in the frequent rupture of the fused quartz container and porous crystals. A partial solution was achieved by fresh samples of Se and the amount of excess Se was changed.

$\text{Cu}_x \text{Li}_{1-x} \text{InSe}_2$ alloys were prepared for $x = 0.1, 0.25, 0.5, 0.6, 0.7$ and 1.0. To prevent excessive attack on the quartz tube, the tubes and boats were carbon coated at 1100°C prior to the run by cracking of methane. The 1100°C during a run where there had been a 10% substitution did not result in chemical attack on the tube. For higher concentration, there was some attack on the coating and glass tube even with 800°C .

CuInS_2 was prepared by the iodine transport method. The material was first synthesized by the melt-growth method. The powdered material was placed with ~5 atm pressure of iodine in a vertical or horizontal furnace. The usual crystal form was an adherent layer on the walls of the capsule. A more successful method involved a 10 mole % substitution of Li for Cu. This reduced the melting temperature to where it was possible to obtain large homogeneous crystals where the maximum temperature employed was only 1100°C and the cooling near the crystallization temperature of about $5^\circ\text{C}/\text{h}$. A typical run involved heating the furnace to 1100°C in 8 h followed by a soak period of 15 h at 1100°C after which the run was cooled to 500°C at a rate of $5^\circ\text{C}/\text{h}$.

The other I-III-VI₂ compounds that were successfully grown as indicated by single crystals as large as a cm across without porosity are CuGaSe₂, CuGaSe₂, CuInTe₂, and AgInTe₂. The crystals containing Ag although often forming big crystals were frequently porous such as for AgGaTe₂, AgGaSe₂, and AgInSe₂. For AgInS₂ there are at least two forms. A run with a maximum temperature of 950 °C followed by slow cooling at 4 °C/h to 700 °C at which the container was quenched in liquid nitrogen produced a few large black non-porous crystals. However, when the material was cooled slowly to 500 °C, the resulting product was porous and polycrystalline. The tendency towards phase change may be the problem for some other Ag containing compounds.

Due to the high melting points, some other compounds were produced in the form of crystals less than 1/2 cm across. This was the case for CuAlSe₂ and AgAlSe₂. Also for AgAlSe₂ the compound was unstable reacting with the during storage after the run apparently forming red Se₄N₄.

Near stoichiometric AgGaS₂ was prepared by heating at the temperature of 950 °C. As the heating temperature increased it was apparent that S-deficient crystals were formed. The high melting point of CuGaS₂ also led to difficulties. By using a fast start up employing rapid heating to 1050 °C where the temperature was held for 10 d, larger crystals of 4-8 mm in length instead of 3-4 mm were produced but they were poorly formed. Vapor transport was tried using CuGaS₂ powder and bromine and iodine. The iodine-transport method gave better crystals over the Br. The crystals were almost nearly stoichiometric.

A run involving CuTlSe₂ was tried but was not successful in producing chalcopyrite as shown by X-ray data. Much of the material was polycrystalline porous and heterogeneous.

3. CRYSTAL GROWTH OF HgS

A. Background

Mercury sulfide is a wide bandgap semiconductor which is of considerable interest because its unique properties offer excellent potential for non-linear optics and laser technology devices. It is the most optically active of all known mineral compounds, possessing the greatest birefringence, a remarkable rotary power and strong piezoelectric properties.

Sapriel²⁷ has reported that α -HgS has the highest acousto-optical figures of merit of any known crystal, making it an efficient material for acousto-optical applications, such as transducers, light modulators, deflectors, delay lines, etc. Ultra-sonic attenuation and the elastic and photoelastic constants in α -HgS have been measured.²⁸ Sapriel and Lancon²⁹ have pointed out that, since the electromechanical coupling coefficients of cinnabar are approximately two times larger than those of Quartz, piezoelectric α -HgS transducers bonded on a parallelepiped cinnabar crystal would realize perfect acoustical matching and therefore yield wide bands for acousto-optical deflection. Thus α -HgS should serve well as a good deflector of laser light. For example, if one assumes a frequency bandwidth of 250 MHz for a transducer made of cinnabar and an acoustic beam 1/2 mm square, it may be shown that only 210 mW of acoustic power is necessary to deflect all of the incident light of a He-Ne laser beam into 62,500 different positions with an access time of 1 μ s.

Mercury sulfide exists in two modifications, cinnabar (α -HgS) and metacinnabar (β -HgS). The α phase crystallizes in an unusual, dihedrally coordinated, red colored, low-symmetry (D_3) structure, the bandgap of which has been measured by Zallen³⁰ as 2.1 eV. This trigonal form is stable at 20 °C and is strongly piezoelectric with $a = 4.149 \text{ \AA}$ and $c = 9.495 \text{ \AA}$ at 26 °C. Metacinnabar, however, is black, metastable at 20 °C, and cubic (T_d^2) ($a = 5.817 \text{ \AA}$) at 26 °C, with $E_g = -0.15 \text{ eV}$.

An early technique, reported by Hamilton³¹, on the synthesis of single crystals of the sulphides of Zn, Cd and Hg was based on a vapor phase growth method utilized by Reynolds and Czyzack³² for the growth of ZnS and CdS crystals. Hamilton employed temperatures below 550 °C for the crystallization of HgS in a pyrex tube containing a pressure of 35 cm of H_2S prepared by triple vacuum distillation. A temperature of 490 °C was applied to the powder source while the region of normal growth was maintained at 440 °C with a value of 8 °C/cm for dT/dx and a minimum run time of 50 hours to produce a growth of crystals with a volume of 20 mm^3 . The deposited crystals were found to grow only in the form of hexagonal columns a few mm long and 1-2 mm thick, with crystal faces so poorly developed that it was difficult to determine structure. There was no evidence of dendrites in this growth. A rough theoretical estimate of the surface free energy according to the method of Harkins³³ (assuming nearest neighbor interactions only and covalent bonding) was found to be in excellent agreement with an experimental value of 300 ergs/cm² obtained for HgS assuming two-dimensional nucleation.

Curtis³⁴, while reproducing and extending Hamilton's experiment, observed a phase transformation at 335 °C above which mercury sulfide

deposited as a black, β -HgS, cubic phase and in cooling below, transferred to a red, α -HgS phase. He concluded that it was unlikely that the vapour phase growth techniques would lead to true single crystal cinnabar because of the phase transformation which served to prevent the growth.

However, Carlson³⁵ attempted the growth of cinnabar below the phase transformation. He obtained crystalline HgS above and below a 344 °C transition temperature, but below, only polycrystalline material or small single crystals were produced. He used 99.0 % pure HCl gas (at concentrations of 0.02 moles/liter) as the transporter gas, and 0.4 g of HgS pelletized charges synthesized from elements each with a purity of 99.999 %. Pyrex tubes having 11 and 8 mm bores, were used to obtain similar crystals with maximum dimensions of about 1.8 mm and crystals with plate like habit with dimensions up to 2.5 x 2.5 x 1.0 mm. He also observed a prismatic habit with dimensions as large as 3.0 x 0.5 x 0.5 mm at high HCl concentrations.

B. Iodine Transport Method³⁶

HgS powder was added in amounts of 50 to 200 g to pyrex containers with a diameter of about 1&3/4 inch and a length of 6 to 12 inches. Much of the powder used was technical grade from the Amend Drug Company who had refined it from the red vermillion paint pigment. In addition to the approximately 2 g of iodine there was added 200 to 500 mg of another chemical in an attempt to enhance the transport properties and resulting crystal growth (will be discussed in next section).

As mentioned earlier, a chief difficulty in growing HgS is that temperatures lower than approximately 330 °C are needed to prevent the material from transforming to the black, cubic phase. However, the low vaporization temperature of the metal iodide species allows one to overcome the transformation temperature limitation. In the past the iodine transport method³⁷ has been used at high temperature because many metal iodides are not very volatile. For ZnI₂ the vapor pressure is one atmosphere at 623 °C, and for CdI₂ it is at 796 °C in contrast to 354 °C for HgI₂. We have observed that the transport of HgS by iodine transport occurs as low as 200 °C. Some initial results on the growth of cinnabar crystals by iodine transport were reported recently.³⁸

Generally the experimental runs involved the use of technical grade HgS with a fairly high impurity content as a source material. The Na content was about 80 ppm, the K content 2.5 ppm and the Cd content 6.7 ppm. About 5 mg/cc of iodine was added to a pyrex tube. See Fig. 8.

The run is started by having the source end of the tube at a higher temperature than the deposition end. The transport species, HgI₂ and S₈, react to form HgS several weeks after a few grams of Hg₃S₂I₂ have been deposited. For a tube 1.5 inches in diameter about 60 g of material is transported in approximately 5 weeks to form cinnabar at temperatures less than approximately 330 °C and metacinnabar above 330 °C.

One of the more successful runs for transport in one direction only involved the use of an 8 inch long, 1.5 inch diameter pyrex tube which was run for 4 weeks over temperatures of from 315 °C to 260 °C and then run for 5 weeks from 400 to 290 °C. Single crystals as large as 5 x 4 x 1/2 mm and 7 x 2 x 1.5 mm were obtained.

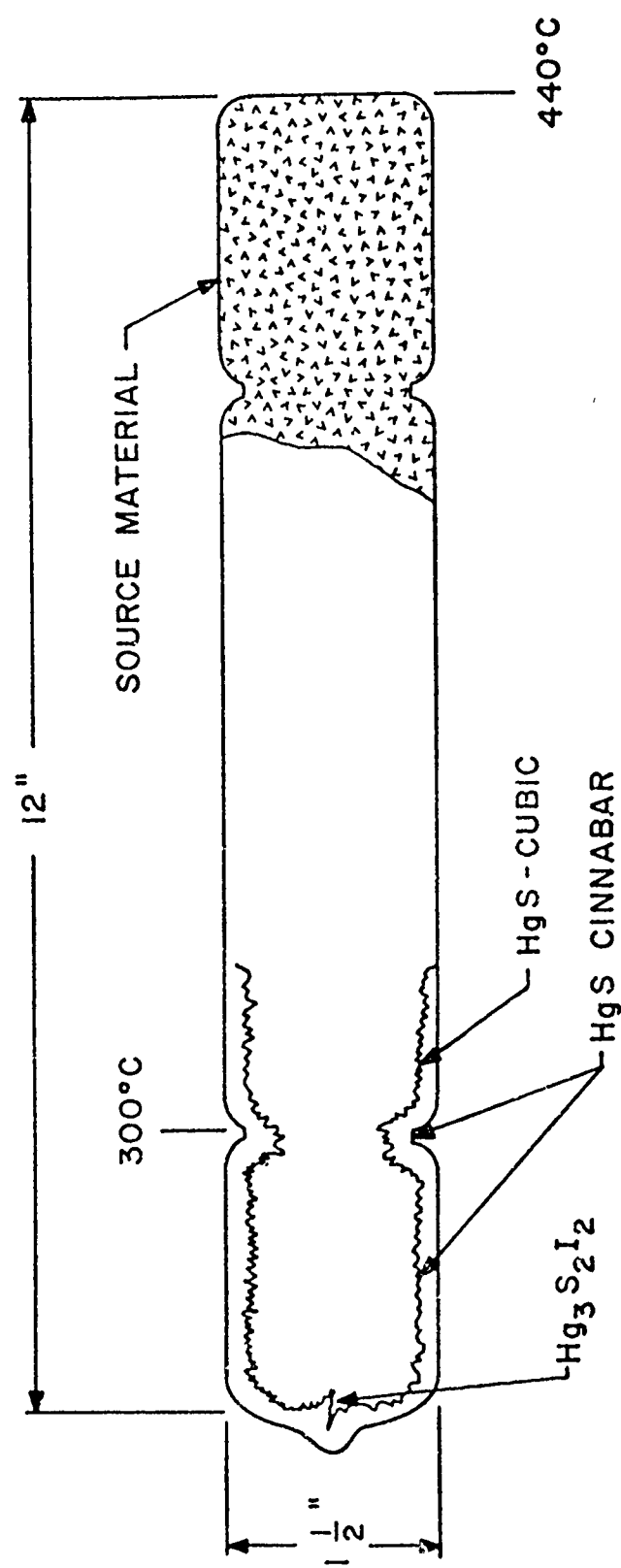


Figure 8. Iodine transport of HgS. The source material in the pyrex tube is composed of 150 g HgS and 3 g I₂.

The duration of the runs for I_2 transport of HgS can be reduced, either by increasing the diameter of the container tube, or by including a compound (containing hydrogen) in the starting material which reacts to form the transport gas H_2S . When the diameter of the 8 inch long tube is increased from 1 to 1.5 to 2.75 inches the transport of material increases respectively from about 3 to 1.5 months to about 3 weeks. This result is obtained for approximately the same depth of HgS powder (1 inch) initially at the warmer end of the tube. For the 1.5 inch diameter tube this corresponds to about 75 g of HgS. The hot end of the tube was held at $400^{\circ}C$ while the cool end was maintained at $300^{\circ}C$. For runs involving the use of containers with a diameter greater than 1.5 inches and an end temperature difference greater than $100^{\circ}C$, there was a tendency for small crystals of cinnabar to form at the cool end, followed later on by larger crystals of metacinnabar. For a 2.75 inch diameter tube this occurred even for deposition temperatures below $200^{\circ}C$.

For more rapid transport rates a higher proportion of impurities may be deposited resulting in a lowering of the transformation temperature. (In a proceeding paragraph we have already noted Ohmiya's observations³⁹ of the lowering of the transmission temperature by an increased impurity content.) Towards the end of a typical run this effect should become more pronounced because, during the early stages, a higher ratio of HgS to impurities is transported. As the HgS is depleted relative to the impurities at the source end, the concentration of the impurities in the transport gas should increase. According to atomic absorption analysis, the source material contains an excess of 70 ppm Na while initial amounts of deposited HgS crystals were found to contain approximately 7 ppm Na.

The iodine transported HgS has also been found to be useful as a substrate for hydrothermally grown HgS. A dendritic formation develops against the pyrex surface as a layer of polycrystalline cinnabar is deposited during iodine transport. This formation of small thickness and generally less than 7 mm width is converted during hydrothermal growth to a wider and thicker mass yielding crystals approximately 1 cm in length.

C. Modified Iodine Transport Method

Various additions of chemicals along with the iodine were added to the starting material such as thioacetamide, 1-dodecanol NH_4Cl , NH_4I , $\text{NH}_4\text{S}_2\text{O}_6$, H_2SO_4 , and H_2O . Also there were runs involving modified HgS. In one instance a mixture of 20 % CdS and 80 % HgS was run using iodine transport where the powder had been made by the precipitation from a solution of boiling HgBr_2 , CdCl_2 and 0.1 mole HCl by the addition of thioacetamide. In another run powdered HgS precipitated from solution was also tried in an attempt to duplicate the results obtained from the Apache Chemical Company which had a volatile contaminant that improved the transport properties and increased the size of the crystals of HgS.

Most of these additions and changes in the HgS powder did not produce substantially larger crystals when the transport was only in one direction for the duration of the run. The transport rate involving the additions was faster than for iodine alone during the first week of the run but generally slowed down considerably later on. In contrast by only using the iodine, at first after the $\text{Hg}_3\text{S}_2\text{I}_3$ compound had deposited, the deposition would be slow but would increase after a couple of weeks. The crystals produced were rarely larger than 1 mm across.

When there were many reversals in the direction of transport the overall transport of HgS to the deposition end in the form of cinnabar greatly increased. Less of the black metacinnabar formed. Best of all for the additions to the iodine there was a general improvement in the size and quality of the crystals produced.

The best results have been obtained for additions of thioacetamide or NH_4Cl in amounts of 200 mg or more. Shown in Fig. 9 is a typical time-temperature relationship of the source and deposition ends for runs involving the addition of NH_4Cl and iodine where the mass flow was periodically reversed.

Shown in Figs. 10 and 11 are crystals from various runs where much of the intermediate sized crystals are from an experiment using 100 g HgS (technical grade), 2 g iodine, and 200 mg NH_4Cl that lasted three weeks during which the mass transport reversals were employed. Over a gram of the HgS was found to be in the form of cinnabar crystals over a mm wide which is a higher yield than for the earlier runs. The size of these crystals is indicated by the small squares in the background which are equivalent to a mm across.

It was found that by increasing the amount of HgS powder to 200 g, the transport rate was greatly reduced. Large crystals generally can only be grown over a duration of over 6 weeks. By increasing the amount of NH_4Cl and iodine there is some improvement in the rate of transport. Fig. 11 shows the results for a later run employing mass transport reversals and involving the use of eight times the amount of NH_4Cl and iodine enclosed in a double walled tube. Due to the limited time of only 4 weeks duration only about a third of the HgS had transported. However, this

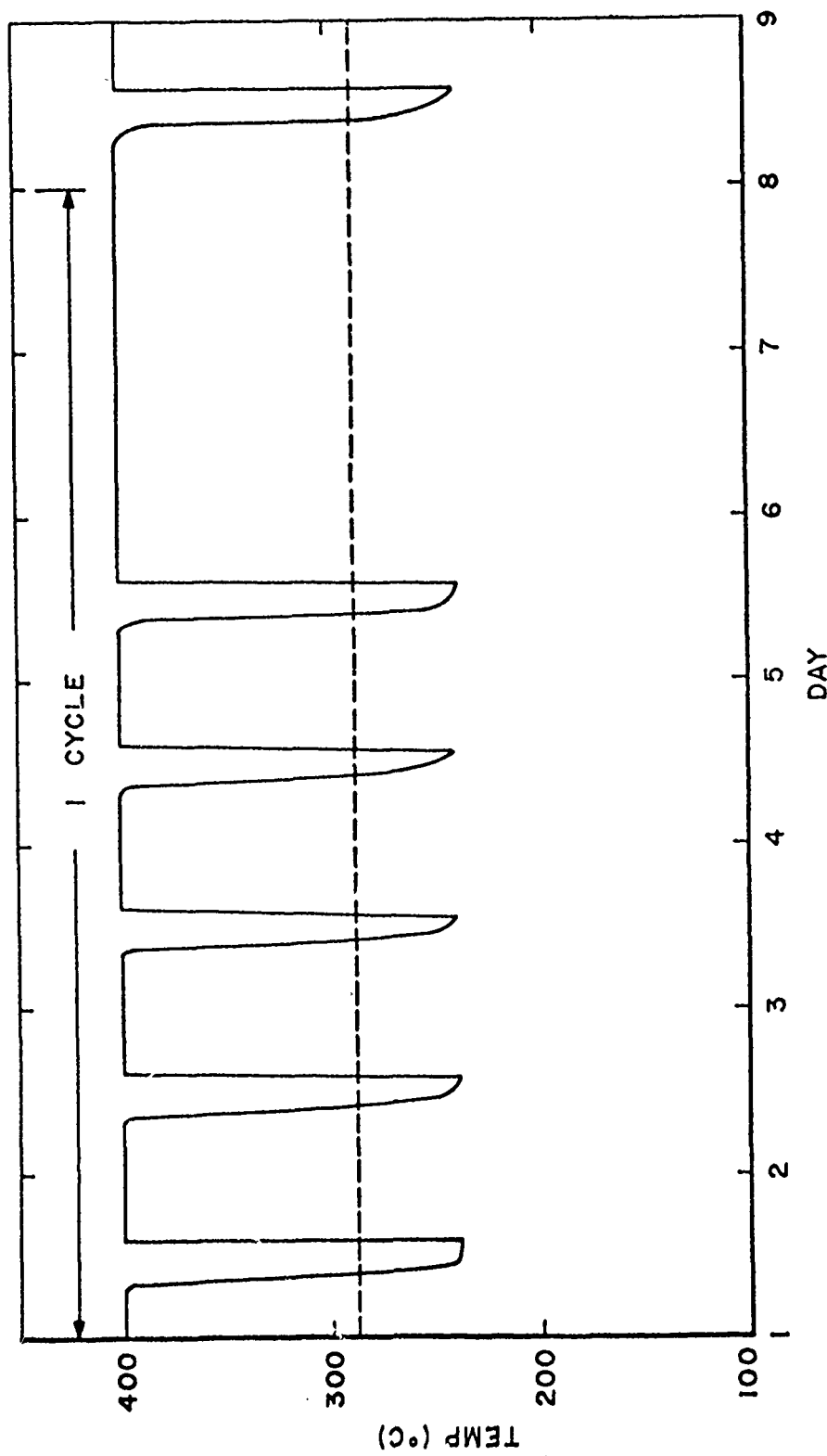


Figure 9. A typical time-temperature relation for the modified iodine transport method.



Figure 10. HgS crystals from various runs with the modified iodine transport method (1 div. = 1 mm).

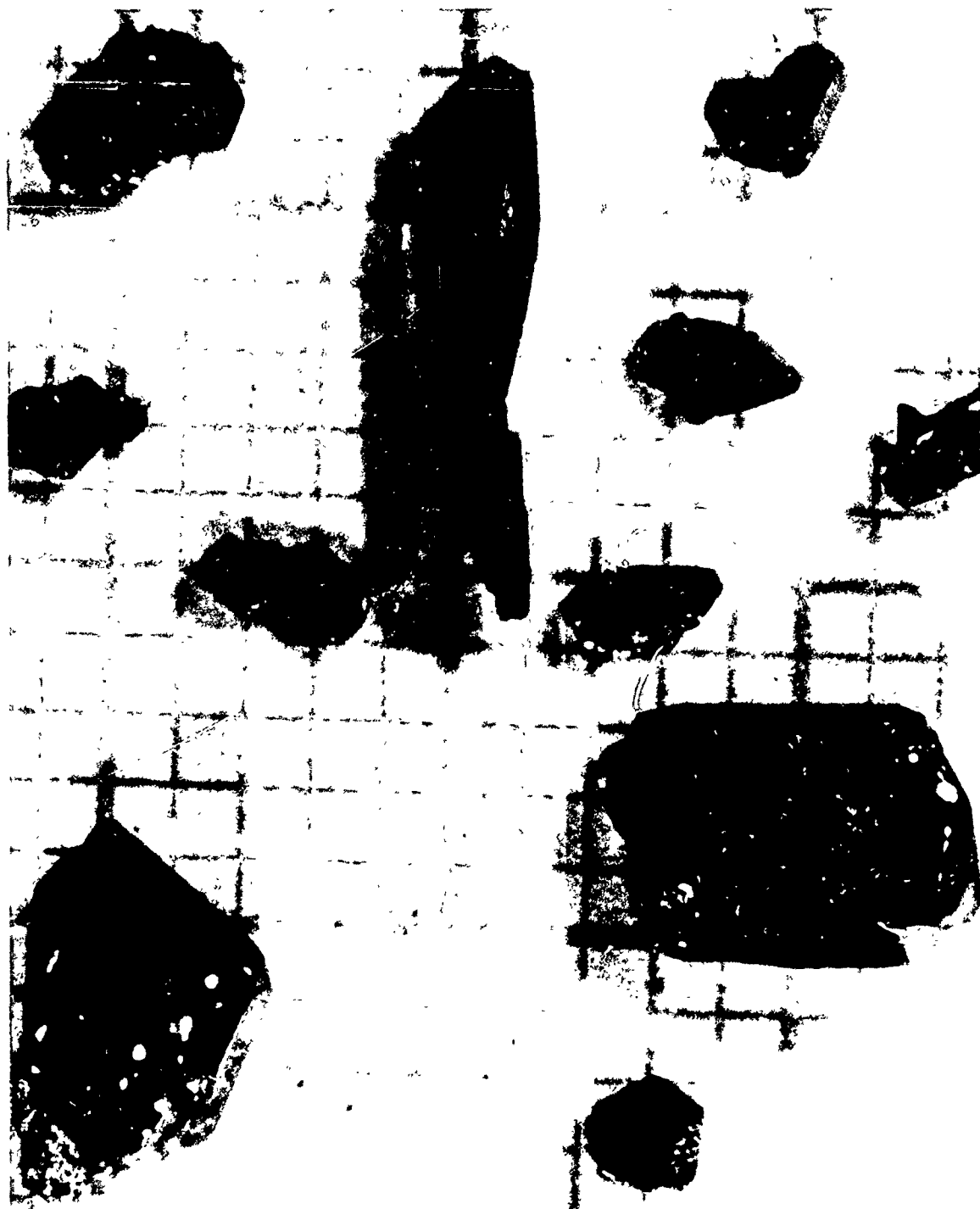


Figure 11. HgS crystals from a run involving large amount of NH_4Cl and iodine enclosed in a double walled tube (1 div. = 1 mm).

was enough to produce the heaviest crystals so far which were up to 4 mm across and 2 mm thick. Since the crystal surface was clean it appears that a longer run could have produced substantially larger crystals. This is in contrast to the runs using iodine only as the transport agent where there would be a tendency for small crystals to form on the surface of the larger ones.

Recent data indicates that faster transport of the 200 g of HgS can be achieved where a large amount of NH₄Cl of over 600 mg is used while not increasing the amount of iodine by leaving the weight at about 2 g.

The achievement of satisfactory reverse flow is a fairly critical process in that the temperature should be high enough, over 280 °C, for there to be significant breakdown of the Hg₃S₂I₂ compound but should not be too high in order to avoid metacinnabar formation. To obtain fairly reproducible results, the deposition end temperature is increased at the start of the run until the condition is achieved during reverse flow where the reddish-orange Hg₃S₂I₂ compound is no longer visible at the deposition end after a few hours.

There are probably many reasons why the modifications are improvements on the basic iodine transport method. The chlorine is lighter than iodine which probably speeds the transport. The hydrogen reacts to form H₂S which diffuses faster than S₈. Other transport species that may have formed that would diffuse faster than S₈, HgI₂ and I₂ are HgCl₂, HgNH₂Cl, HgNH₂I, HI, HCl, and others. That the volatile transport species form is indicated by the pressure remaining after a run which is in excess of one atmosphere pressure and by the H₂S order upon opening the capsule. The higher volatility of the transport species resulting in a

high vapor pressure probably produced a higher concentration of transport material in the vapor phase. As an example sulfur in form of H_2S can be transported to the vicinity of deposition as a vapor at $290^{\circ}C$ at a much higher concentration than could S_8 which would be largely condensed.

The change in the direction of the transport may have a cleaning effect on the already formed cinnabar crystals as the high surface area sites with defects that would develop into new crystals are removed during the reversal of the mass flow. This would allow the crystals to subsequently grow larger without interference from other new crystals.

The overall increased transport rate caused by the transport reversals is probably caused by the breakup of the $Hg_3S_2X_2$ (where X is a halogen) to produce a higher concentration of volatile species such as HgI_2 and $HgCl_2$ that would otherwise be tied up in the compound. The periodic reversals would result in enough additional transport material to increase the overall deposition of HgS .

The periodic decreases in the source temperature subjects more of the deposited material to low temperatures where cinnabar is favored. Even though for most of the time much of the deposited material is above $310^{\circ}C$ much more of the material remains in the cinnabar phase as opposed to metacinnabar apparently due to the pronounced metastability of cinnabar at these temperatures.

D. Hydrothermal Method

Hydrothermal crystal growth of cinnabar was conducted using a method similar to that of Toudic.⁴⁰ The source material was technical grade HgS and polycrystalline plates of HgS obtained from iodine transport runs. The seed crystals were single crystals obtained from the iodine transport work. About seven runs were done after the assembly of the

furnace, controller, pressure vessel, water reservoir, argon gas tank, and fittings into a hydrothermal system was accomplished around October of 1974. The hydrothermal solution, which was held over a temperature gradient of 330 °C to 290 °C, consisted of HgS ions in 0.5 molar Na₂S that was held in a sealed teflon capsule for a run lasting one to three months. The larger single crystals measure about 2 mm across while poorly formed crystals in the form of floral growth were as much as a cm across but were less than a mm thick.

E. Other Crystal Growth

The use of iodine and bromine transport was employed in an attempt to grow Nb₃Ge crystals and others with substitutions of aluminum. The transport was slow producing crystals in the mm size range after two weeks over a temperature gradient from 900 °C to 700 °C.

Crystals of ZnSe, ZnS, and ZnS-ZnSe alloys were grown in horizontal and vertical furnaces using iodine transport and in some cases seed crystals orientated to grow on the (111) plane. A typical run for growing ZnSe involved the use of a 6 cc silica capsule containing 12 g of ZnSe, 1 mg Se/cc, and 5 mg I₂/cc. Good quality crystals were grown for a mixture of 15 weight percent substitution of ZnS in ZnSe grown over a temperature range of 820 °C to 720 °C in a vertical furnace. The crystals were about 5 mm thick and 20 mm long.

The components for an epi-growth reactor were ordered but due to changing priorities the parts were turned over to others to use in constructing a pyrolytic reactor.

Polycrystalline GaAs was grown by iodine transport at temperature ranging from 350 °C to 800 °C. The material, which contained Cr as a

dopant generally consisted of crystals 1 mm across. The runs with thioacetamide as a transport enhancer had low electrical resistance while the ones with the NH_4Cl had a high electrical resistance similar to the Cr doped source material.

4. ANALYSIS OF PREPARED I-III-VI₂ COMPOUNDS

X-ray diffraction analysis techniques provide the most useful methods for the analysis of prepared I-III-VI₂ compounds. Powder methods, such as the Debye-Scherrer diffraction method, are the most useful ways to confirm the formation of desired compounds. From powder diffraction data, precision measurements were made of the lattice constants of the compounds. In addition, the indexing of the diffracted lines, observation of the systematic absence of certain (h k l) reflections and the determination of the diffracted intensities of the lines allowed the determination of the compound's space group and the atomic arrangement within the crystal. Single crystal methods, specifically, back-reflection Laue techniques, made it possible to determine the existence of a single crystal and to orient the crystals along any desired specific crystallographic direction for subsequent experimental investigations.

A. Debye-Scherrer Powder Patterns

In order rapidly to identify or confirm the formation of I-III-VI₂ compounds by Debye-Scherrer techniques it is necessary to have standard X-ray diffraction patterns to compare with the experimental data. Since standard X-ray diffraction patterns are not readily available, theoretical X-ray powder patterns may be computed if the space group, crystal structure, and lattice constants are known or assumed for the compounds.

A computer program was written to compute the theoretical X-ray diffraction patterns for the I-III-VI₂ (I = Cu, Ag; III = Al, Ga, In; VI₂ = S, Se, Te) compounds which crystallize in the chalcopyrite structure. The input data required for the program are: (1) the lattice constants, a_0 and c_0 , (2) identification of the atoms present in the compounds, and (3) the X-radiation used in the experiment (CuK α or CrK α). The output from the program is a list of Miller indices h , k , ℓ of the reflecting planes, d_{hkl} , $1/d_{hkl}^2$, the intensity of the diffraction line, and the relative intensity of the diffracted line (I/I_0). This list is printed in order of decreasing d_{hkl} values.

For the I-III-VI₂ compounds being investigated, the interplanar spacings, d_{hkl} , were computed from Eq. 1 for all hkl values from (0, 0, 1) to (9, 9, 15) which satisfied the extinction rules for the space group I42d, namely, $h^*k\ell$: ($h+k+\ell = 2n$), $0k\ell$: ($k+\ell = 2n$), $hh\ell$: ($\ell = 2n$) and ($2h+\ell = 4n$), $h00$: ($h = 2n$) and $hh0$: ($h = 2n$).

$$\frac{1}{d_{hkl}^2} = \frac{h^2+k^2}{a_0^2} + \frac{\ell^2}{c_0^2} \quad (1)$$

The diffracted intensities of the allowed hkl reflections were computed from Eq. 2.

$$I_{hkl} = |F_{hkl}|^2 \cdot p \cdot LP \quad (2)$$

where F_{hkl} is the structure factor; p is the multiplicity; and LP is the Lorentz-Polarization correction. No attempt was made to make the relatively minor temperature correction.

The structure factor was computed in the usual manner, Eq. 3, where u_N , v_N , and w_N for the undistorted chalcopyrite structure are as follows: for Type I atoms, $uvw = (000)$, $(1/2 1/2 1/2)$, $(1/2 0 1/4)$ and $(0 1/2 3/4)$; for Type III atoms, $uvw = (1/2 1/2 0)$, $(0 0 1/2)$, $(1/2 0 3/4)$ and $(0 1/2 1/4)$; for Type VI_2 atoms, $uvw = (1/4 1/4 1/3)$, $(3/4 3/4 1/8)$, $(3/4 1/4 3/8)$, $(1/4 3/4 3/8)$, $(1/4 1/4 5/8)$, $(3/4 3/4 5/8)$, $(3/4 1/4 7/8)$, and $(1/4 3/4 7/8)$.

$$|F_{hkl}| = \left[\left\{ \sum_1^N f_N \cos 2\pi (hu_N + kv_N + \ell w_N) \right\}^2 + \left\{ \sum_1^N f_N \sin 2\pi (hu_N + kv_N + \ell w_N) \right\}^2 \right]^{1/2} \quad (3)$$

$$+ \left[\sum_1^N f_N \sin 2\pi (hu_N + kv_N + \ell w_N) \right]^2$$

The atomic scattering factors, f_N , were computed from fourth, fifth, and sixth order polynomial fits to f_N vs. $\sin \theta/\lambda$ data tabulated in the International Tables for X-ray Crystallography, Vol. III, pp. 210-211.

The multiplicities for the various hkl reflections were taken from Azaroff's Elements for X-ray Crystallography, p. 201. The Lorentz-Polarization factor was computed according to Eq. 4.

$$LP = (1 + \cos^2 (2\theta)) / (\sin^2 \theta \cos \theta) \quad (4)$$

where θ is the Bragg angle for the (hkl) reflection.

Appendix I is a listing of the computer program used for these computations and Appendix IIa and IIb present the "standard" diffraction patterns calculated for AgGaS_2 and CuGaS_2 .

These crystals were analyzed by X-ray diffraction and found to have the desired chalcopyrite crystal structure. Precision lattice constants obtained from the X-ray data are listed in Table 4. Alloys

of $\text{Cu}_x\text{Li}_{1-x}\text{InSe}_2$ ($x = 0\text{-}1$) were analyzed. The compounds of $x = 1\text{-}0.5$ have a chalcopyrite structure. However, the alloys of $\text{Cu}_{40}\text{Li}_{60}\text{InSe}_2$ and $\text{Cu}_{30}\text{Li}_{70}\text{InSe}_2$ were mixed form of the chalcopyrite and LiInSe_2 (orthorombic) structure. The results of the x-ray diffraction were used to identify $\alpha\text{-HgS}$ and $\beta\text{-HgS}$.

B. Single Crystal Orientation

Crystals of material samples were evaluated and oriented for subsequent optical and electrical properties investigations throughout the report period. Using Laue back-reflection procedures, crystals could be identified as single crystals and oriented readily once the familiarity with the patterns was established. Since standard stereographic projections do not exist for crystals other than members of the cubic and hexagonal crystal classes, it was necessary initially to compute and construct several stereographic projections for the tetragonal I-III-VI₂ materials. Projections were constructed for the [100], [010], and [001] for the crystal. A set of Laue backreflection patterns along the important crystal directions was made for use during subsequent crystal orientations.

TABLE 4. LATTICE PARAMETERS OF I-III-VI₂ CRYSTALS

	<u>a</u> (\AA)	<u>c</u> (\AA)
AgGaS ₂	5.756 \pm .001	10.301 \pm .002
CuAlS ₂	5.330 \pm .001	10.415 \pm .002
CuGaS ₂ (green)	5.3491 \pm .0005	10.477 \pm .001
CuGaS ₂ (orange)	5.2357 \pm .0006	10.472 \pm .004
CuInS ₂	5.463 \pm .004	11.160 \pm .009
CuInSe ₂	5.604 \pm .003	10.93 \pm .01
CuInSe ₂	5.775 \pm .004	11.595 \pm .006

SECTION III
OPTICAL PROPERTIES

In this section we describe the lowest energy gap variation in AgGaS_2 and CuInSe_2 , radiative recombination in these crystals, injection luminescence in CuInSe_2 and ZnS , and the oscillatory photoconductivity in Cr-doped semiinsulating GaAs.

1. TEMPERATURE DEPENDENCE OF ENERGY GAP⁴¹ IN AgGaS_2 AND CuInSe_2

A. AgGaS_2

The photoluminescence, reflectivity and absorption studies were performed with single crystals of p-type AgGaS_2 grown from the melt. They were oriented with X-rays and cut with a (100) surface for the polarization study. As-grown crystals were also used (commonly (112) surfaces). Photoluminescence, reflectivity, and absorption peak were measured photographically with a 2 m Bausch and Lomb spectrograph with a dispersion of 2.5 \AA/mm . The excitation source for the luminescence was a Hg-lamp. Absorption spectra were measured using a Cary Model 14 spectrophotometer.

Near normal incidence exciton reflectivity spectra of AgGaS_2 were obtained for incident light polarized parallel to the optic axis ($E \parallel C$). The $4.2 \text{ }^\circ\text{K}$ reflectivity is shown in Fig. 12(a). The main reflectivity peak's maximum is at 4597 \AA and the maximum of the weak structure is observable at 4564 \AA . The position of the oscillator energy relative to the reflectivity maximum⁴² depends on many factors such as the line width and strength. In our data, the maximum of the main reflectivity anomaly corresponds to the emission peak of the lowest energy exciton (A-exciton). The strong and weak reflectivity

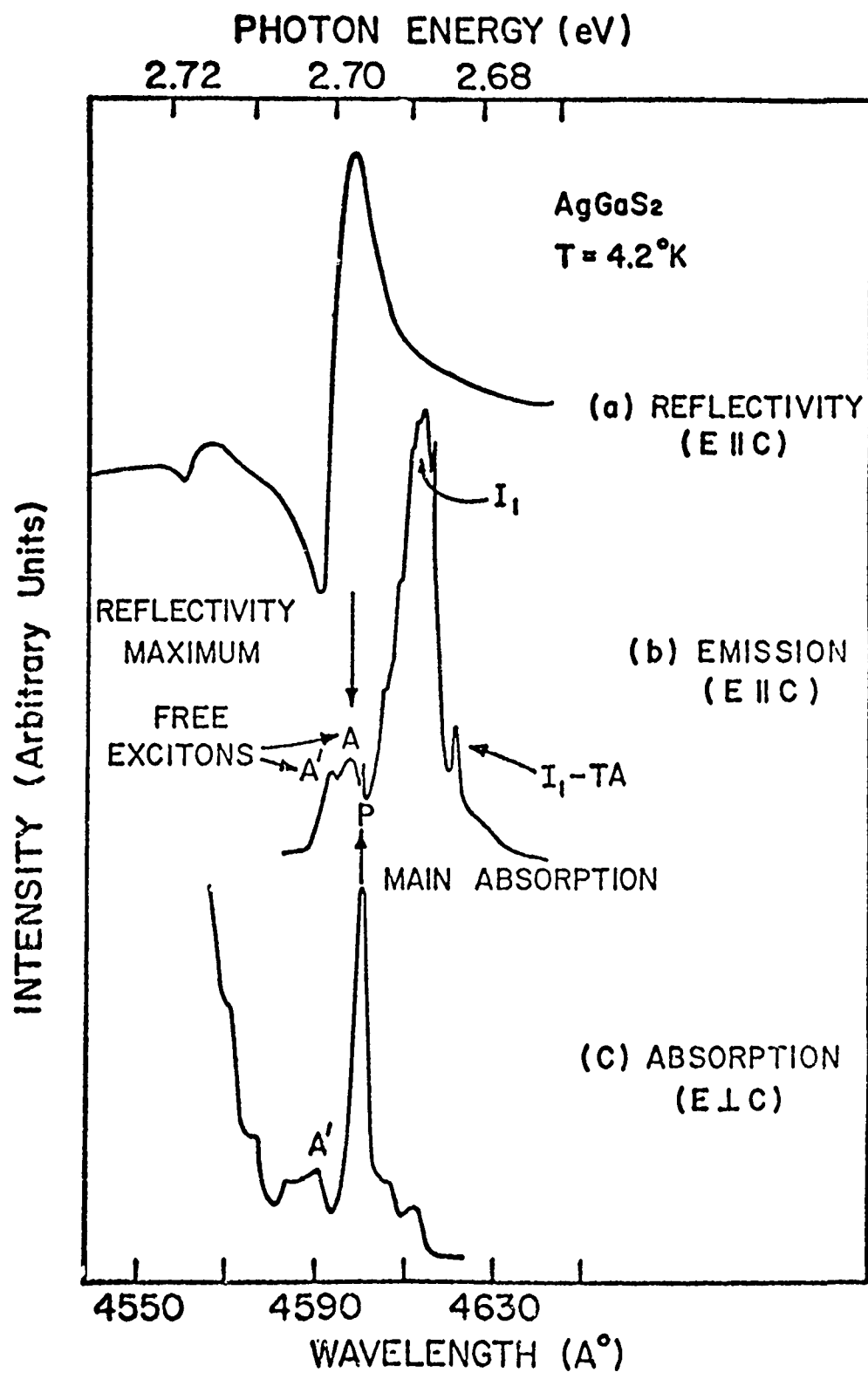


Figure 12. The reflectivity, photoluminescence and absorption spectra of AgGaS_2 near the band edge at $T = 4.2^\circ\text{K}$. All of the spectra were obtained by the densitometer tracing.

peaks correspond respectively to the ground and excited state of the lowest energy exciton. Using these peaks as the energies of the exciton state, the lowest gap is calculated as 2.723 eV at 4.2 °K. The binding energy of the exciton is 26 meV.

In the photoluminescence spectrum, three emission lines at 4592, 4597 and 4600 Å are observed around the maximum of the main reflectivity peak at 4.2 °K. The spectrum is presented in Fig. 12(b). These lines are active predominantly for light polarized parallel to the optic axis ($E \parallel C$). This is consistent with the reflectivity spectra and the selection rule. The polarization ratio ($I \parallel / I_{\perp}$) for these lines is ~ 14 . The energy of the emission line at 4597 Å corresponds to the maximum of the main reflectivity peak. Therefore, this line is due to the free exciton (A-exciton) involving the smallest gap between the lowest conduction band and the uppermost valence band.

The emission line at 4592 Å is separated by ~ 3.3 meV from the A-exciton peak. This may be another exciton (A'-exciton) related with a band below the A-band. The other line at 4600 Å is about 4.6 meV from the A'-exciton. The emission at 4612 Å was assigned⁴¹ as the radiative decay of the exciton bound to a neutral acceptor (I_{\perp} -line). This emission is accompanied by a phonon replica at 4621 Å. This phonon is also observed in the phonon-replicas of other bound excitons at 4662 and 4683 Å. The energy of this phonon is 4.9 ± 0.4 meV. The phonon can be assigned as an acoustical phonon at the N point⁴³ if the consistency relationship (between the chalcopyrite and the zinc-blende structures) and the phonon energies⁴⁴ of ZnS (II-VI analog) are considered. With this consideration, the emission at 4600 Å (P-line) maybe a phonon-assisted transition of the A'-exciton.

The 4.2 $^{\circ}\text{K}$ absorption spectrum is shown in Fig. 12(c). The absorption lines are experimentally observed for light polarized perpendicular to the optic axis ($E \perp C$) even though they are active predominantly for $E \parallel C$. The main absorption peak rises $\sim 40-50 \text{ cm}^{-1}$ at 4600 \AA . The energy of the line corresponds to that of the P-line in the emission spectrum. The weak absorption peak, which corresponds to the emission line of the A'-exciton is at 4591 \AA . Other absorption lines at higher energies than 4591 \AA are the phonon-assisted transitions of the A'-absorption line.

The main reflectivity anomaly, the three emission lines, and the main absorption peak were observed as the temperature increased. The result is shown in Fig. 13. All of the peaks go to higher energies with an increase of temperature up to $\sim 80 \text{ }^{\circ}\text{K}$ and then move down to lower energies for higher temperatures. The temperature coefficient is $+ 6 \times 10^{-5} \text{ eV/}^{\circ}\text{K}$ at lower temperature. The absorption coefficient was measured for light polarized perpendicular to the optic axis for temperatures above 150 $^{\circ}\text{K}$. The absorption spectra are shown in Fig. 14. The small size of the crystals limited the maximum absorption coefficient measurements to $\sim 400 \text{ cm}^{-1}$. The lowest energy gap was determined with the calculated energy of the A-exciton and the energy gaps determined by fitting the absorption curves above $T = 150 \text{ }^{\circ}\text{K}$ with a direct allowed transition. The result is shown in Fig. 15. The temperature coefficient of the lowest gap is $+ 6 \times 10^{-5} \text{ eV/}^{\circ}\text{K}$ over the temperatures 4.2-80 $^{\circ}\text{K}$ and $- 1.8 \times 10^{-4} \text{ eV/}^{\circ}\text{K}$ in the temperature range 80-300 $^{\circ}\text{K}$.

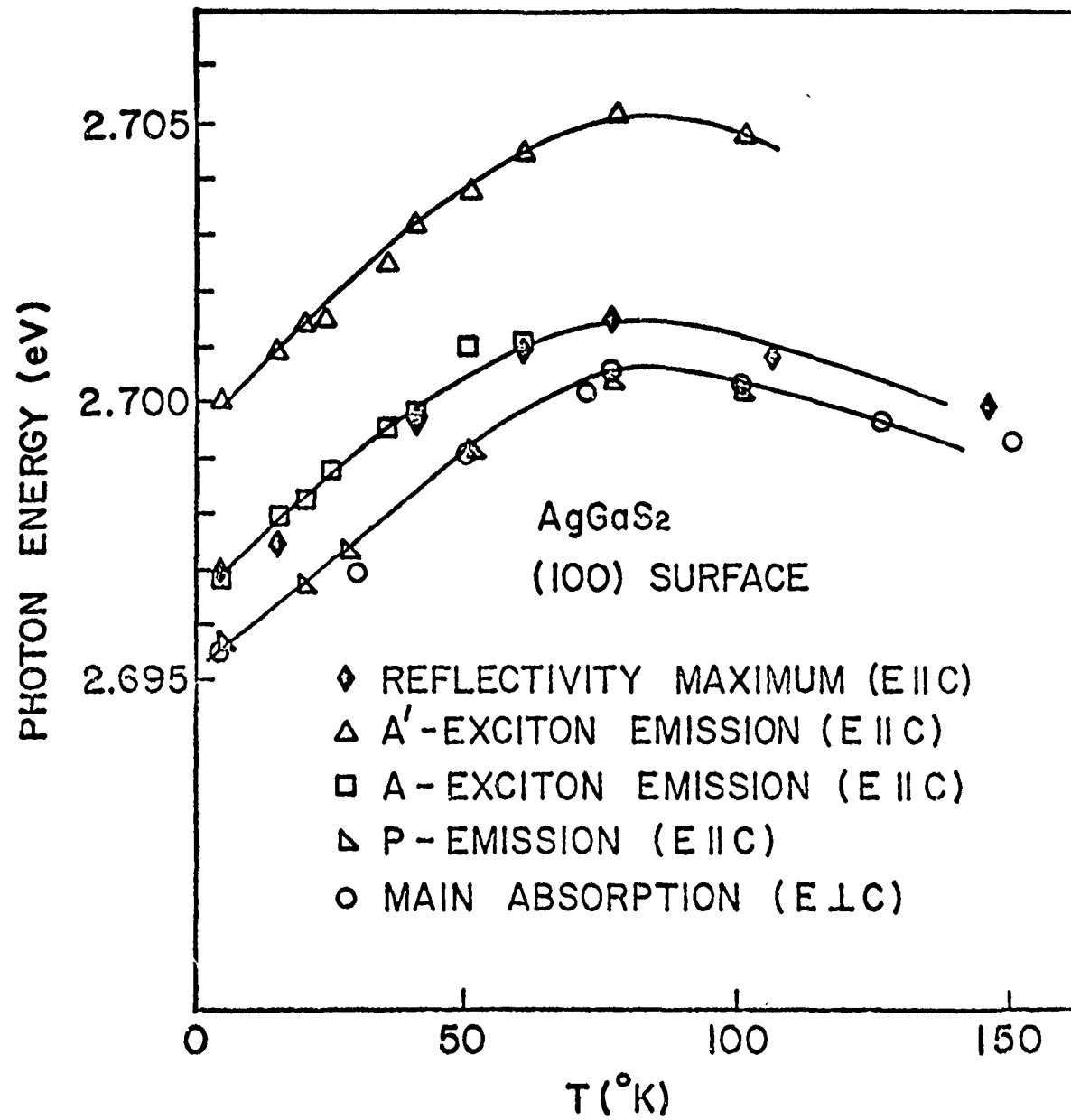


Figure 13. The temperature dependence of the position of the main exciton reflectivity maximum, the three emission peaks (A-exciton, A'-exciton and P-line) and the main absorption peak.

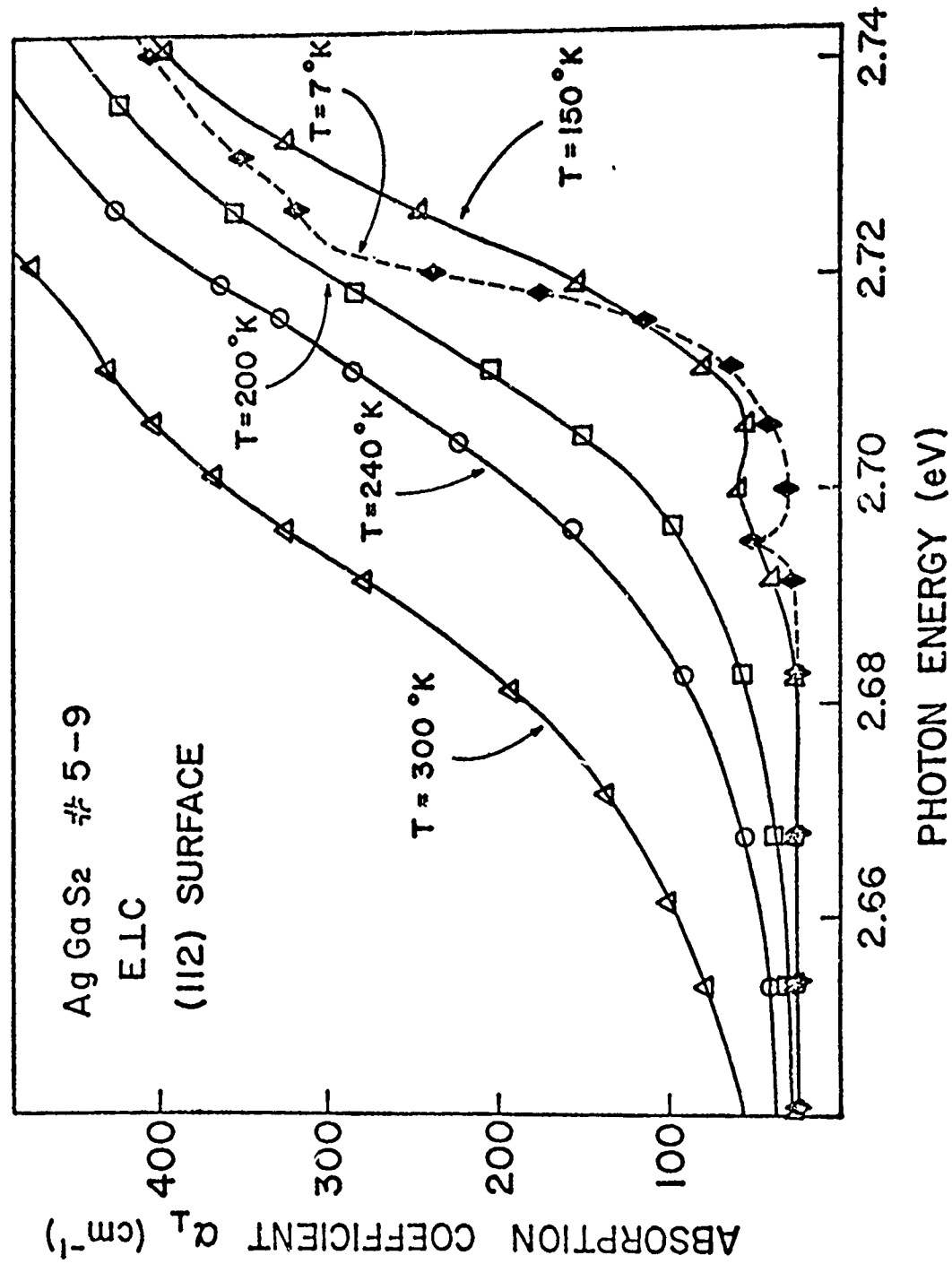


Figure 14. The absorption coefficient α_L versus the temperatures at 7, 150, 200, 240 and 300 °K.

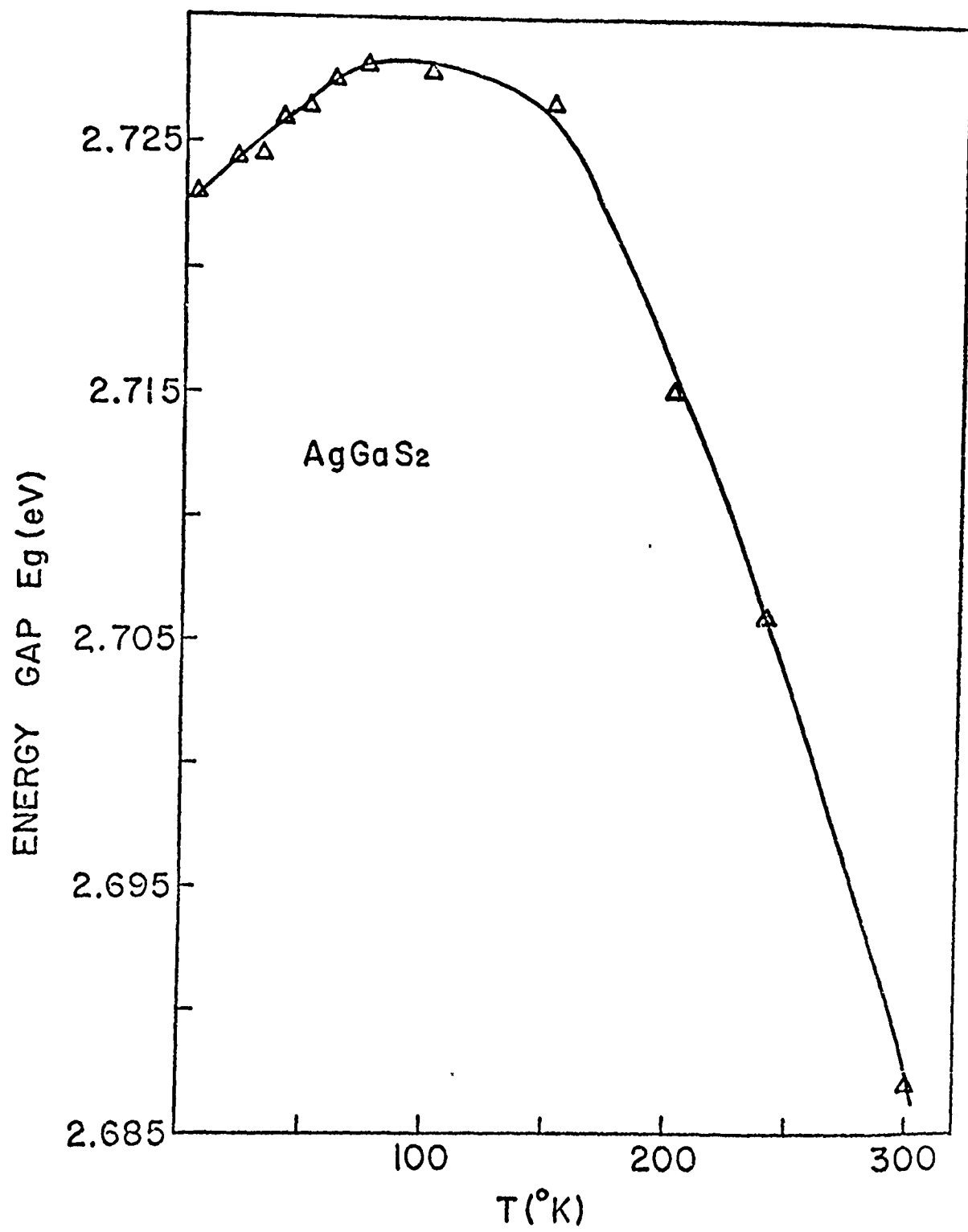


Figure 15. The lowest energy gap of AgGaS_2 in the temperature range 4.2-300 $^{\circ}\text{K}$.

The temperature dependence of energy gaps is caused by the thermal expansion of the lattice (volume effect) and the electron-phonon interaction. The small temperature coefficient and the change of the sign mean that the two effects are compensating each other. Since the sign due to the electron-phonon interaction⁴⁵ is expected to be negative, the positive sign can be attributed to the volume effect. The temperature dependence of the AgGaS_2 lattice constants is not known. However, it can be assumed that the lattice constants increase with the temperature. The p-d hybridization of the materials containing d-electron metals such as AgCl and AgBr have been discussed⁴⁶ earlier. With the increase of the lattice constants the contribution of the Ag wave function to the valence band wave function decreases, which could produce an increase of the energy gap. Along this line of interpretation, the positive value can be explained by the volume effect being a dominant mechanism for the energy gap variation at lower temperatures. This contrasts with the usual explanation⁴⁵ that the temperature dependence is mainly caused by the electron-phonon interaction.

B. CuInSe_2

The positive temperature coefficient of the lowest energy gap was also observed in CuInSe_2 . Fig. 16(a) and (b) show typical emission spectra at 4.2 °K and 77 °K obtained from p-type crystals which were grown from the stoichiometric melt. Fig. 16 (c) also shows a similar emission band. Excitation was made with a Kr laser operating at a wavelength of 6471 Å. The energy of the band E_x is 1.037 eV at 4.2 °K and 1.042 eV at 77 °K. The emission band is very

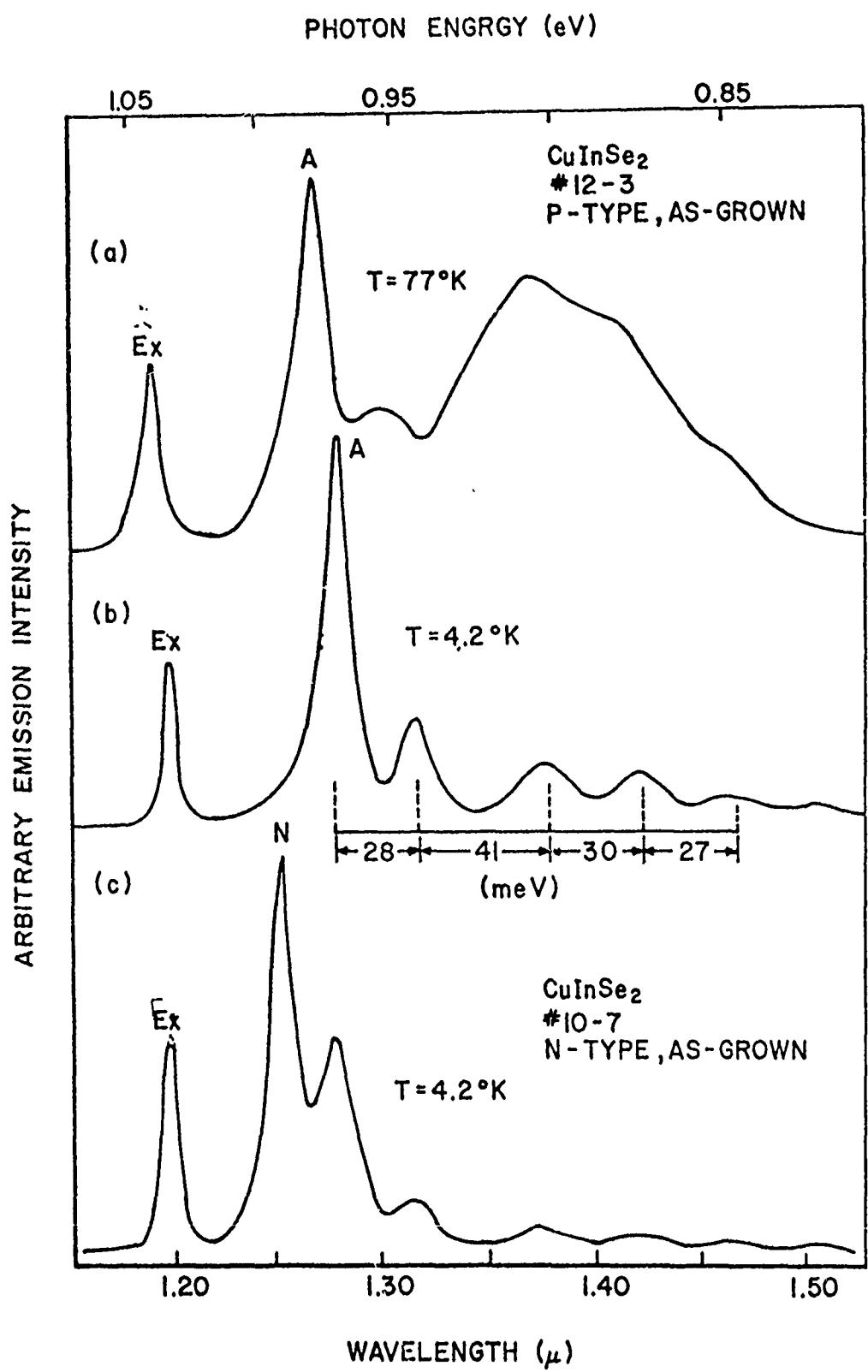


Figure 16. Luminescence Spectra (a) (b) from p-type crystals grown from the stoichiometric melt and (c) from n-type crystals.

near to the reflectivity peak by Shay, et. al.⁴⁷. The emission is, therefore, due to the decay of a free exciton from the conduction band to the uppermost valence band. The free exciton binding energy of CuInSe_2 is not known. However, assuming the free exciton binding energy of 18 meV obtained from $1/2 (E_x|\text{CdSe} + E_x|\text{ZnSe})^{48,49}$, the band gap energy of CuInSe_2 is 1.055 eV at 4.2 °K. Also, the calculated free exciton binding energy is ~18 meV with $m_e^* \approx 0.15$, $m_h^* \approx 0.6 m_e$, and the dielectric constant $\epsilon \approx 9.3$ in CuInSe_2 , which are taken analogously from the binary analogs ZnSe and CdSe. The energy of the free exciton peak shifts to higher energy from 4.2 °K to 77 °K with a small change in energy (5 meV). The temperature coefficient of the lowest energy gap is $+ 6.8 \times 10^{-5} \text{ eV/}^\circ\text{K}$.

2. LUMINESCENCE OF AgGaS_2

Many sharp lines as well as broad band emission bands were observed⁵⁰ at lower temperature. One of the most striking features of the luminescence spectra was a series of sharp lines (half-width $\sim 10^{-3}$ eV) at wavelength greater than 4775 Å. These lines are superimposed on a broad band peaking at ~5000 Å. The analysis of these lines enabled the determination of lattice phonon energies. Experimental set-up was discussed earlier. A spex 1702 spectrometer ($f = 3/4 \text{ m}$) was used for broad band instead of a 2 m Bausch and Lomb spectrograph.

A. Broad Emission Bands

At 4.2 °K, most of the as-grown crystals are dominated by broad green emission peaking at ~5000 Å. Fig. 17(a) shows the spectra at 4.2 and 77 °K. The peak shifts to higher energy with an increase

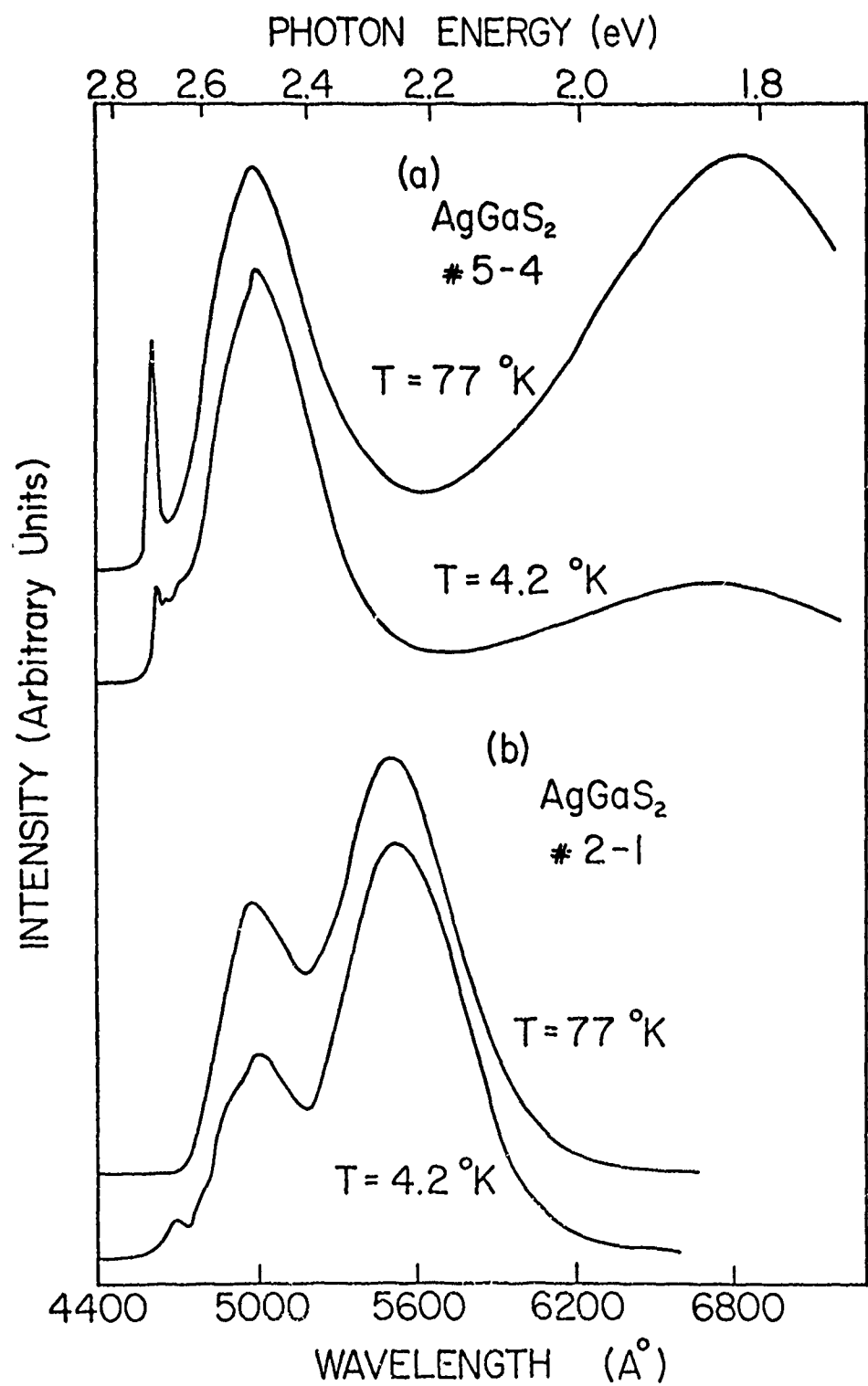


Figure 17. Broad-band emission spectra of AgGaS_2 at 4.2 and 77 $^{\circ}\text{K}$
 (a) As-grown crystals often show the bands at ~ 5000 and ~ 6800 \AA . The 6800- \AA band is quenched by annealing in a sulfur atmosphere. (b) Successive annealing in a sulfur atmosphere and vacuum results in the band at ~ 5500 \AA

of temperature. This agrees with the observation of the dependence of the lowest gap on temperature. Another broad red peak at $\sim 6800 \text{ \AA}$ is seen as shown in Fig. 17(a) with the green peak. This red peak is observed to be quenched by annealing in a sulfur atmosphere. However, annealing in argon resulted in the enhancement of this emission. The crystals showing the red peak as a dominating emission normally indicate n-type conductivity. Therefore, this may indicate that the sulfur vacancies are responsible for this emission.

Another broad emission is seen as presented in Fig. 17(b). As-grown crystals seldom show this peak. Successive annealing in a sulfur atmosphere and vacuum results in this band at $\sim 5500 \text{ \AA}$. The appearance of this peak upon annealing is in contrast with the red band. The chemical nature of this center is not clear at the present.

B. Bound Exciton and Phonons

In Fig. 18 the general picture of photoluminescence spectra in the region from the free excitons to the broad green peak is shown. The most striking feature of this peak is the sharp lines which are superimposed on this emission. Some of the lines are equally spaced with the two distinct phonon energies of 5.4 and 7.2 meV. The lines start from a sharp line (A line at 4775 \AA) and become broader at longer wavelengths. The energy of 43 meV, as indicated in Fig. 18, appears to mark the repetition of the repeat interval for the structure which becomes more diffuse as the number of repetitions increase. Three such repetitions are shown in Fig. 18. Figure 18 shows a high-resolution spectrum of the lines in one structure with energies listed in Table 5. The resemblance of the spectrum to that reported for ZnTe^{51} with oxygen, GaP^{52} with Cd-O complexes and ZnSiP_2^{53} is very striking.

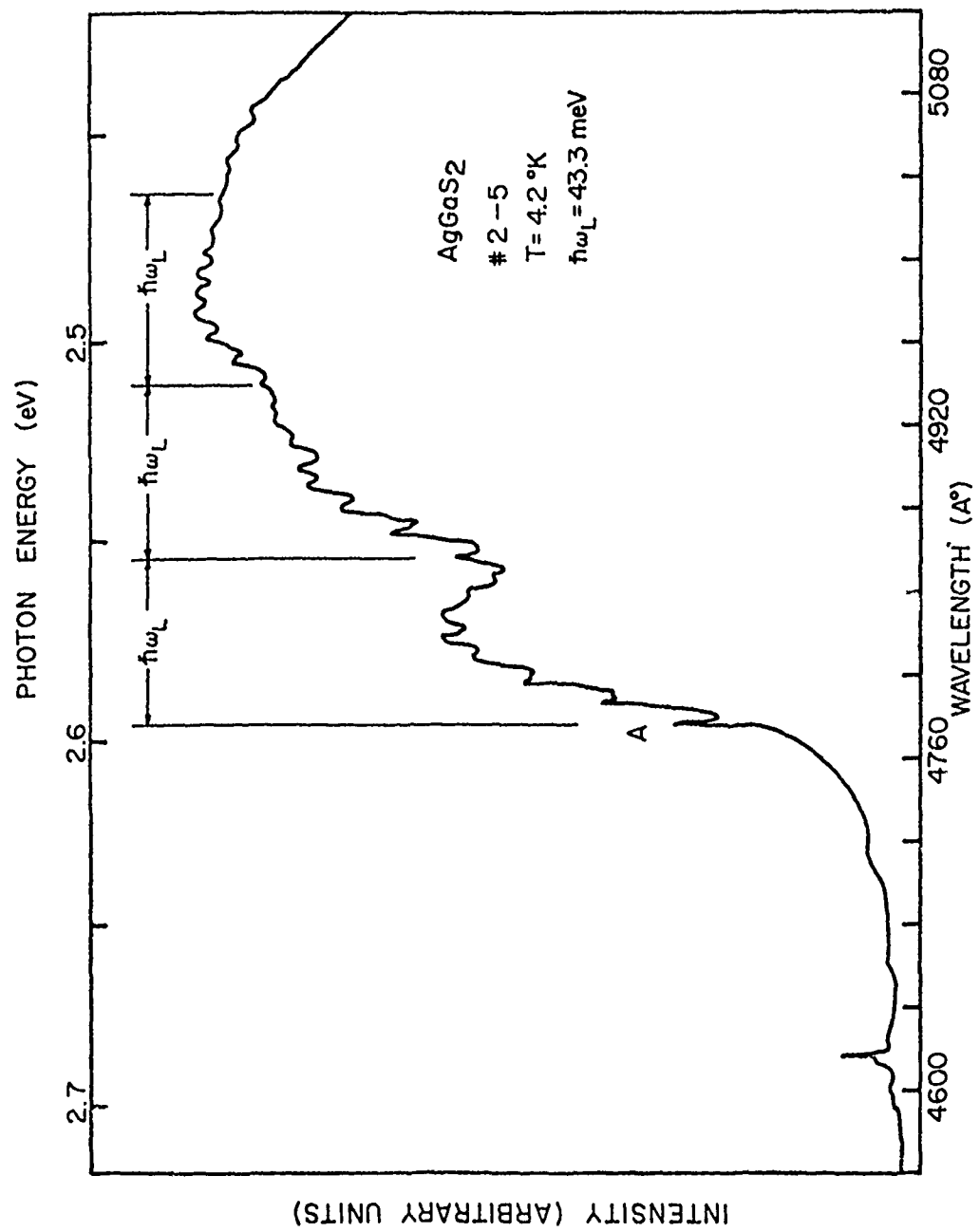


Figure 18. 4.2 °K photoluminescence emission spectrum of a broad band peaking at ~5000 Å together with other emission peaks. Many phonon lines are superimposed on the broad band. The repeat interval for the phonon structure is indicated by ω_L (43.3 meV).

TABLE 5. ENERGY POSITION OF VARIOUS EMISSION LINES AT
4.2 °K. THE ENERGY OF THE A LINE IS 2.59622 eV.
X AND Y CORRESPOND TO TWO PHONON ENERGIES.

Line	Energy difference from A line	Assignment	Phonon energy (meV) (Raman)	Phonon energy (meV) (ir) ^a
A	0			
B	1.6			
1	5.2	X		
2	7.2	Y	7.9	
3	10.9	2X		
4	12.2	X + Y	11.9	
5	15.7	3X		
6	18.1	2X + Y		
7	20.6	X + 2Y	19.9	20.6
8	21.7	4X, 3Y		
9	23.1	3X + Y		
10	26.4	5X		
11	29.3	4X + Y, 4Y	27.8	29.1
12	32.9	6X		
13	34.7	5X + Y		
14	37.1	7X	36.9	
15	41.5	6X + Y		
16	43.3	$h\nu_L = 8X$	45.5	43.1
17	48.9	$h\nu_L + X$	48.9	48.8
18	50.7	$h\nu_L + Y$		
19	54.4	$h\nu_L + 2X$		
20	55.8	$h\nu_L + X + Y$		

^aReference 54.

The A line at the wavelength of 4775 Å is very sharp (half-width 0.5 meV). This is possibly a no-phonon transition associated with an impurity or a defect. This center is very deep. Also, the dominance of the phonon-assisted transition suggests that the potential involved is of a very short-range nature. A weak B line is seen 1.6 meV apart from the A line in Fig. 19. The splitting may result from the coupling of a $j = 3/2$ hole with a $j = 1/2$ electron. The A line is a dipole-allowed transition from $J = 1$ to $J = 0$. This center appears to be related with an isoelectronic impurity as in the case of ZnTe doped with an oxygen.

Consider the numbered lines in the photoluminescence spectrum as indicated in Fig. 18. The energy separation between certain peaks is the same, with energy of 5.4 ± 0.3 meV (X). This indicates that these peaks are due to transitions with emission of one or more phonons of energy 5.4 meV. The other lines which do not belong to this category can be explained with the possible combination of another phonon of energy 7.2 ± 0.3 meV (Y) and the phonon of energy 5.4 meV. Therefore, the basic elements of phonon structure are the phonons of 5.4 and 7.2 meV.

Annealing studies have also been done for this structure of the numbered lines. The crystals were annealed under a maximum sulfur pressure or a minimum sulfur pressure with silver and gallium. The annealing temperatures were in the range $450\text{--}700$ °C for 2-4 days. The spectra taken with the annealed crystals were compared with those from the untreated crystals. The structure remains unchanged in energies as well as in the shape of lines.

Since the appearance of the spectrum suggests the presence of phonons, a Raman scattering study was performed at 300 °K with the 562-nm

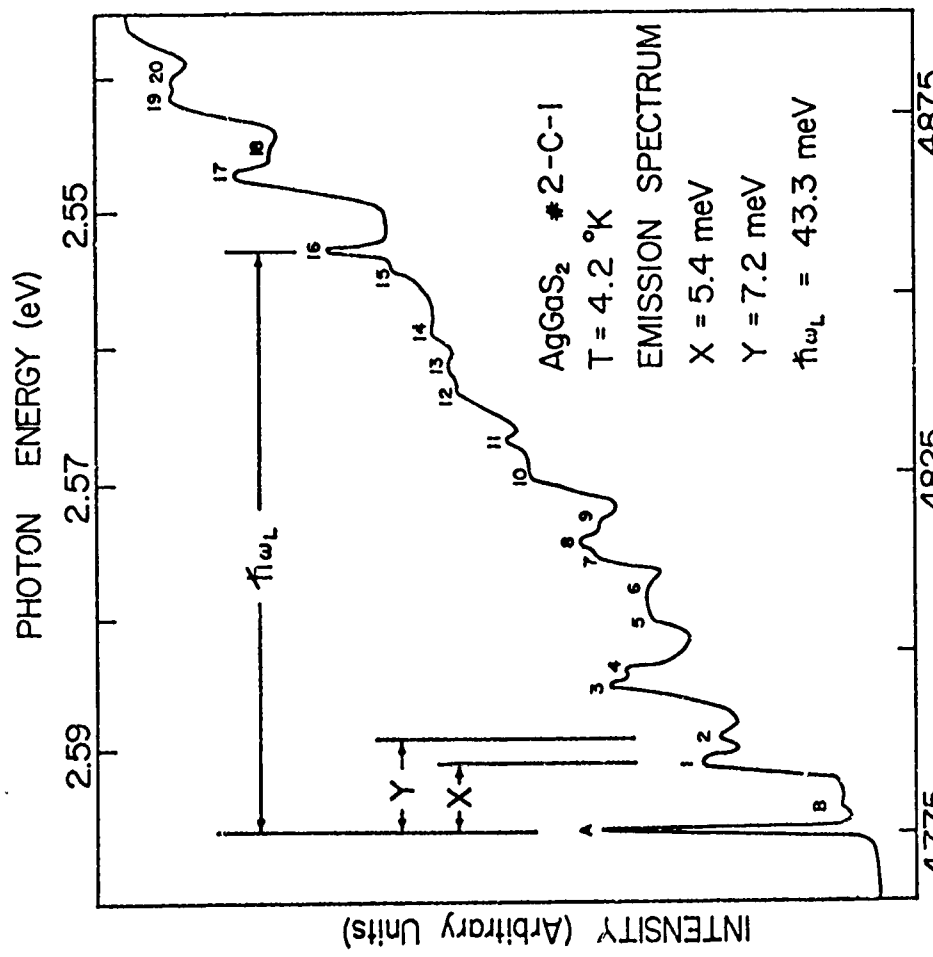


Figure 19. 4.2 °K photoluminescence emission spectra for a phonon structure in the broad band. The A line is a no-phonon line at 4775 Å. The phonon energies are indicated by X and Y.

line of a frequency-doubled Nd:YAG pulsed laser. A typical spectrum is shown for the polarization with Z(YZ)Y in Fig. 20. It shows seven Raman active phonons. The phonon energies are listed in Table 5. The 7.9 meV is probably the 7.2 meV mode observed in the luminescence spectra.

The above experimental facts indicate that these phonons are evidently lattice modes. Table 5 summarizes the phonon energies involved in the structure. The phonon energies obtained from our Raman experiment and from the infrared reflectivity by Holah⁵⁴ are also listed in Table 5. The phonon with energy 43 meV, which makes the repetition of the interval for the phonon structure, could be regarded as a longitudinal optical phonon.

There are two basic phonons in the phonon-assisted transitions. The energies are 5.4 and 7.2 meV. The phonon energies for large k are not known for AgGaS_2 . However, a rough comparison may be obtained by the analysis of the consistency relationship of the symmetry groups of the lattice under consideration. The zone-edge transverse acoustical phonon energies in ZnS ⁴⁴ are 9 meV (L) and 11.5 meV (X). The zone-edge phonon energies in the chalcopyrite structure can be smaller compared to those of the zinc-blende zone. This is due to the folding of the Brillouin zones. The phonon with energy 5.4 meV could be an acoustical phonon at the zone edge. The X point in the zinc-blende zone can be expected to map into the Γ point in the chalcopyrite zone. These phonons have energies comparable to the transverse acoustical phonon energy at the X point in ZnS . Possibly the two smallest phonons (5.4 and 7.2 meV) are the acoustical and optical phonons at the zone edge in AgGaS_2 .

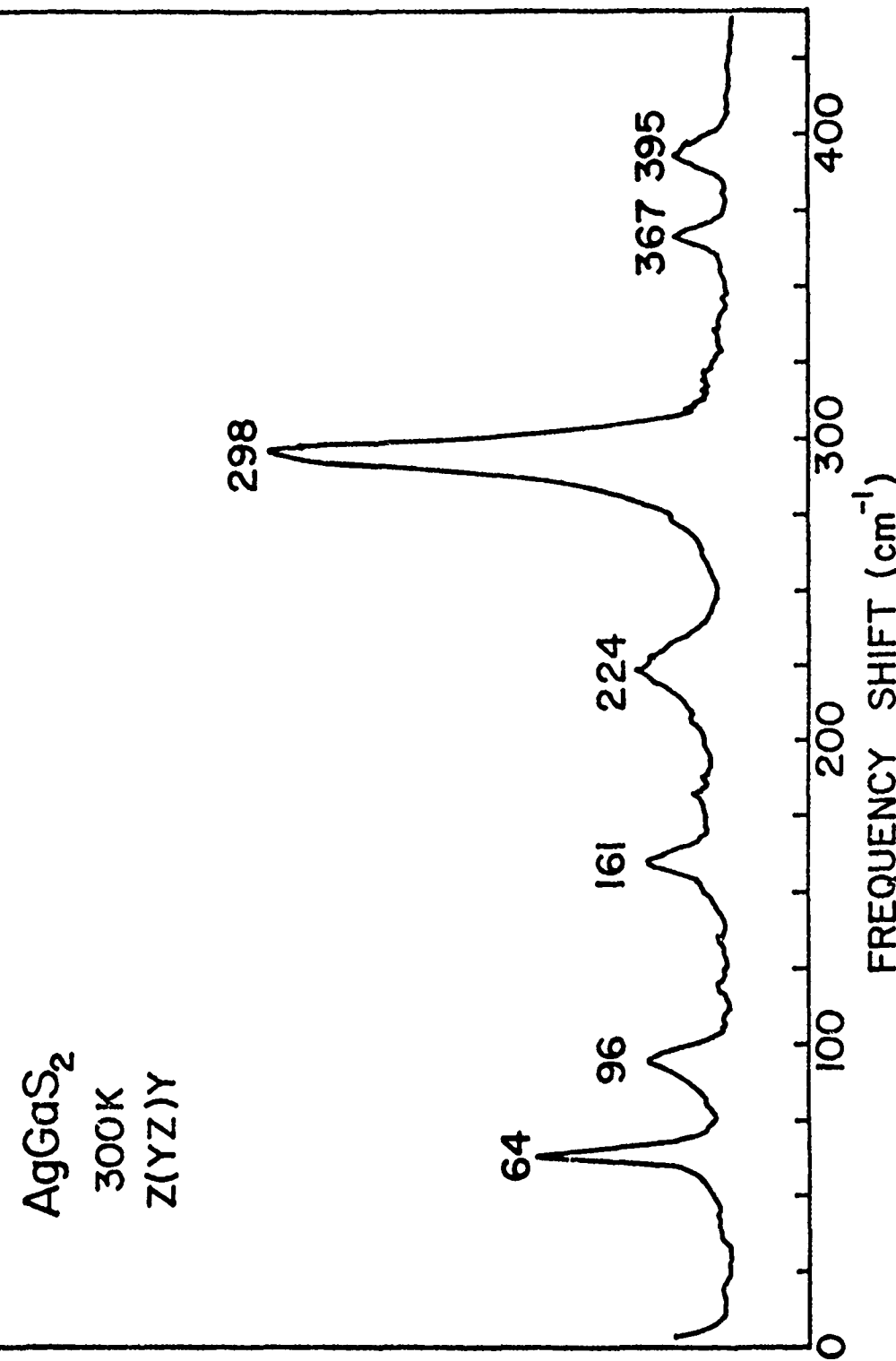


Figure 20. Raman scattering from AgGaS₂

3. OPTICAL ROTATION⁵⁵ IN AgGaS₂

In comparison to birefringence, optical activity is a relatively weak effect, thus optical rotatory dispersion has not been measured before along a birefringent axis. Using the nomenclature of Hobden⁵⁶, the fractional transmitted intensity, I/I_0 , passed by the sample, placed between crossed polarizers, is

$$\frac{I}{I_0} = \frac{(G/\bar{n})^2}{(n_e - n_o)^2 + (G/\bar{n})^2} \sin^2 (1/2 L\Delta), \quad (5.)$$

where

$$G = n\phi\lambda_0/\pi, \Delta = 2\pi[(n_e - n_o)^2 + (G/\bar{n})^2]^{1/2}/\lambda_0,$$

\bar{n} is the mean refractive index of the two modes, ϕ is the rotatory power, λ_0 is the free space wavelength, L is the crystal thickness and n_e and n_o are the refractive indices of the extraordinary and ordinary polarization modes respectively. It is interesting to note that when $|n_e - n_o| \gg |G/\bar{n}|$, the positions of the peaks in the I/I_0 curve are determined mainly by the birefringence while the amplitude of the peaks depends predominantly on the optical activity. This characteristic makes possible calculating the optical activity and birefringence as a function of wavelength.

Fig. 21 is the fractional transmitted intensity for a 0.13 mm thickness, 5 K temperature, AgGaS₂ sample from the 4th to the 10th fringe labeling the peak of zero birefringence with zero as shown. The optical activity at 0.4979 μ was 608°/mm measured by rotating the analyzing polarizer until the intensity was extinguished (also indicating zero birefringence). The birefringence at each peak was

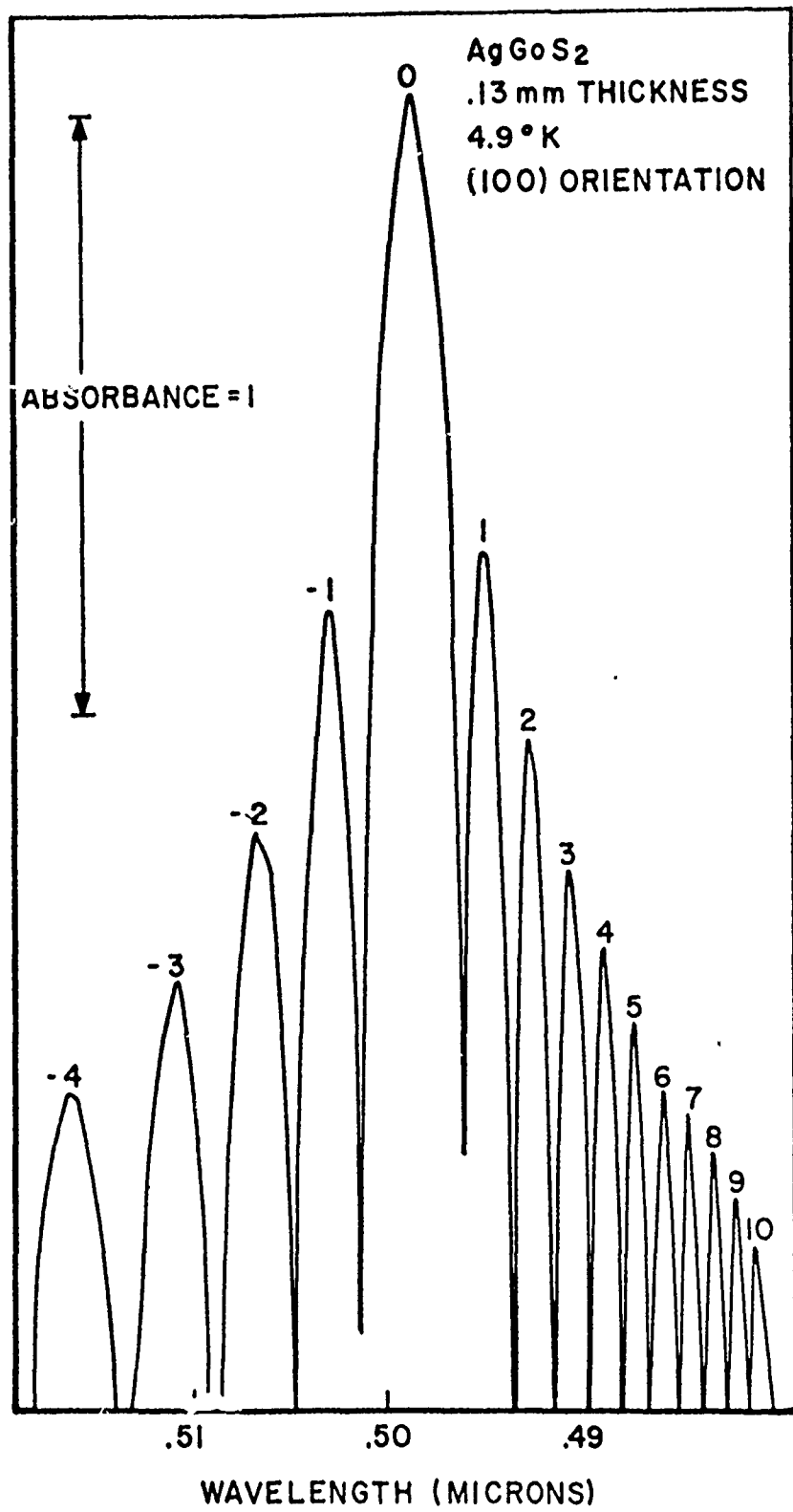


Figure 21. The absorption of a Ag₃GeS₂ sample 0.13 mm thick placed between crossed polarizers at 4.9 °K

calculated from

$$L\Delta/2 = (2n + 1)\pi/2, \quad n = 0, 1, 2, \dots \quad (6)$$

and assuming a constant rotatory power of $608^{\circ}/\text{mm}$. Except for the region from peak -1 to $+1$ the birefringence agreed within a few percent of the published values.^{9,57}

The amplitude ratio of each peak to the zeroth peak was then used to calculate the optical rotatory dispersion in Fig. 21 by assuming

$$I/I_0 \approx (G/\bar{n})^2 / (n_e - n_o)^2. \quad (7)$$

A small correction had to be made to compensate for the difference between the absorption coefficients for the two polarization modes. The interference spectrum was measured first by setting the polarizer perpendicular and then parallel to the optic axis. The two measurements were averaged to obtain the peak ratios. The maximum difference in peak amplitude between the two measurements was $\approx 10\%$ for the high energy side of the interference spectrum decreasing to zero at the low energy side. Fig. 22 also contains the optical rotatory dispersion curves for 125 K and 300 K measured in the same way. The method for measuring the optical rotatory dispersion discussed is useful when there is a point of zero birefringence.

4. DONOR-ACCEPTOR PAIR BAND IN CuInSe₂

We discuss broad-band emission⁵⁸ dominating at 4.2°K in p-type crystals grown from an excess Se atmosphere. Luminescence spectra were obtained for the samples at temperatures ranging from 4.2 to 100°K . For fixed-temperature measurements the samples were immersed directly

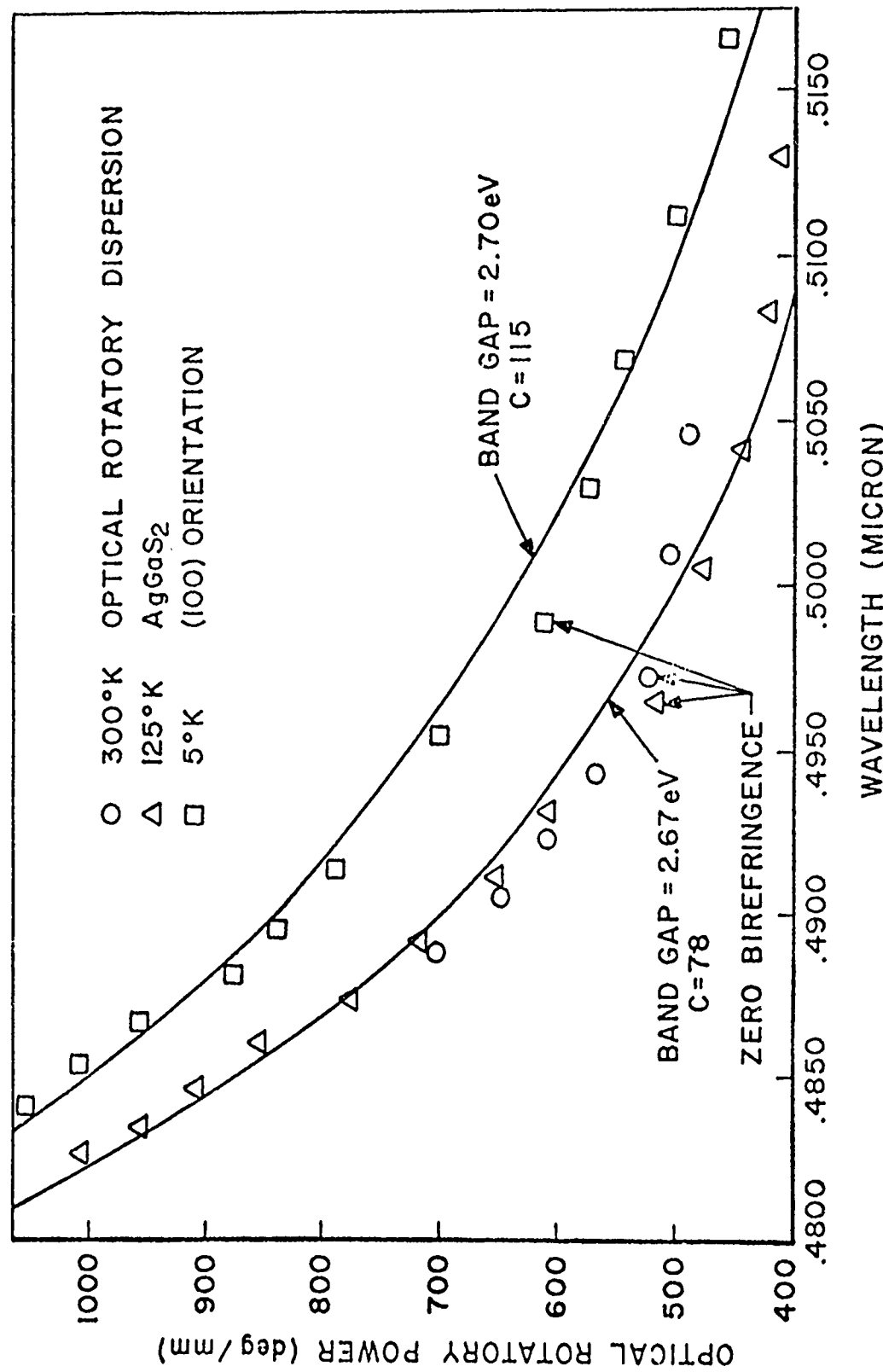


Figure 22. The optical rotatory dispersion for AgGaS₂ sample used in Fig. 21.

into liquid helium. A Heli-Tran Dewar was used for variable temperatures. A Kr laser operating at the wavelength of 6471 Å, with maximum power of ~240 mW, was used for excitation. The emission spectra were analyzed by a 3/4-m grating Czery-Turner spectrometer (11 Å/mm) and detected with a room-temperature PbS cell.

Generally, the observation of sharp pair lines⁵⁹ in the emission spectrum is direct evidence of the presence of a donor-acceptor pair recombination. When sharp lines are not observed, several alternative indicators are usually employed to identify donor-acceptor pair emission. Such indications are; (1) changes in band shape and band-peak energy as a function of excitation intensity, and (2) band shift to higher energy (generally) with an increase in temperature and eventual dominance of a higher-energy band. We employed the above techniques to see the behavior of the low-temperature broad-band emission spectrum of p-type CuInSe₂ with change in temperature and excitation intensity.

The crystals were p-type with a hole concentration ranging from 2×10^{16} to 2×10^{17} cm⁻³ at room temperature. The emission spectrum of the as-grown p-type crystals was dominated by a broad band at 4.2 °K. The peak energies of the band of most samples were in the range 0.93-0.95 eV. However, the peak energy was changed by heat-treating in vacuum and heavy doping. All peaks observed lay in the broad range of energy of ~0.87-0.95 eV at 4.2 °K.

Figure 23 shows spectra taken at 4.2 °K with changing excitation intensity for a typical as-grown p-type sample having a broad band. It is evident that his emission band moves to lower energies as the

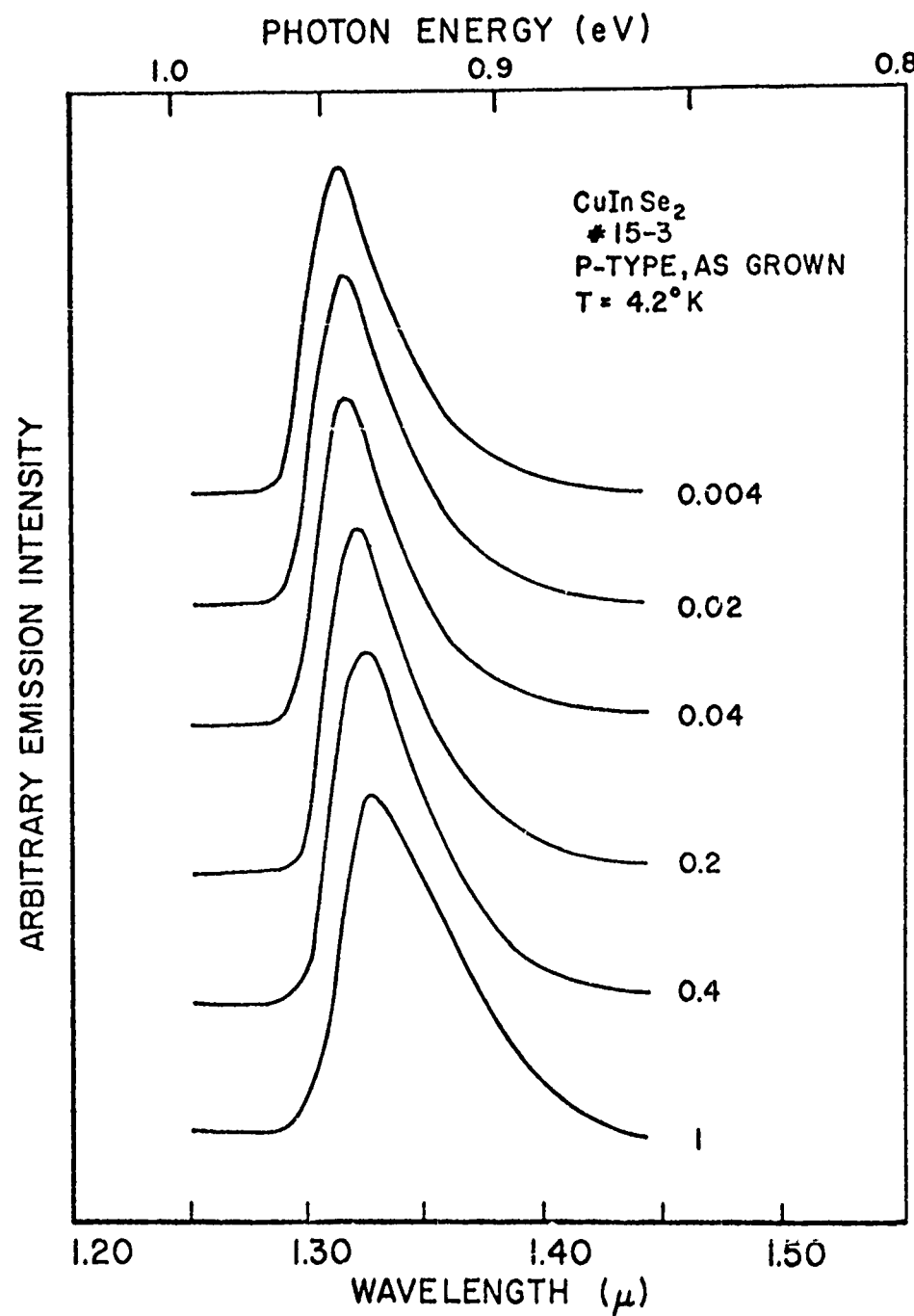


Figure 23. Effect of excitation intensity on the band position at 4.2 °K. The fractional excitation intensities are shown on each spectrum. Maximum power is 240 mW from the 6471 Å line of a Kr laser. Emission intensity decreases with the intensity of excitation. Each emission spectrum has been normalized.

excitation intensity is reduced. The half-width of the band also increases with attenuation of the excitation intensity. In Fig. 24 the excitation intensity L is plotted as a function of peak energy E_p for the same sample. It is clear that L varies exponentially with E_p , i.e.

$$L = L_0 \exp (E_p / \beta), \quad (8)$$

where β is the coefficient which represents the energy shift per decade of excitation. This number was observed to vary from sample to sample depending upon the band-peak energy. This effect can be explained by an increase of the Coulomb term in the acceptor-donor pair-energy relation when the increase of excitation intensity favors the closer pairs. A similar peak shift with excitation has been taken as evidence of a donor-acceptor pair band in many semiconductors such as GaP^{60} , $(\text{Al, Ga})\text{P}^{61}$, $(\text{In, Ga})\text{P}^{62}$, GaAs^{63} , ZnSe^{64} , and InP^{65} .

Figure 25 shows the emission spectra obtained using the same excitation intensity but an increase in temperature to 110°K for the as-grown p-type crystal. The band remains at the same energy up to $\sim 35^{\circ}\text{K}$. With an increase in temperature, the band shifts to higher energies; with further increase, a second band begins to emerge on the higher-energy side and the first band begins to diminish. This can be easily understood under the assumption that a single recombination mechanism is responsible for the band; at higher temperature the carriers released thermally from their original sites move to energetically more favorable sites, which reduces the distance r in the pair-energy relation

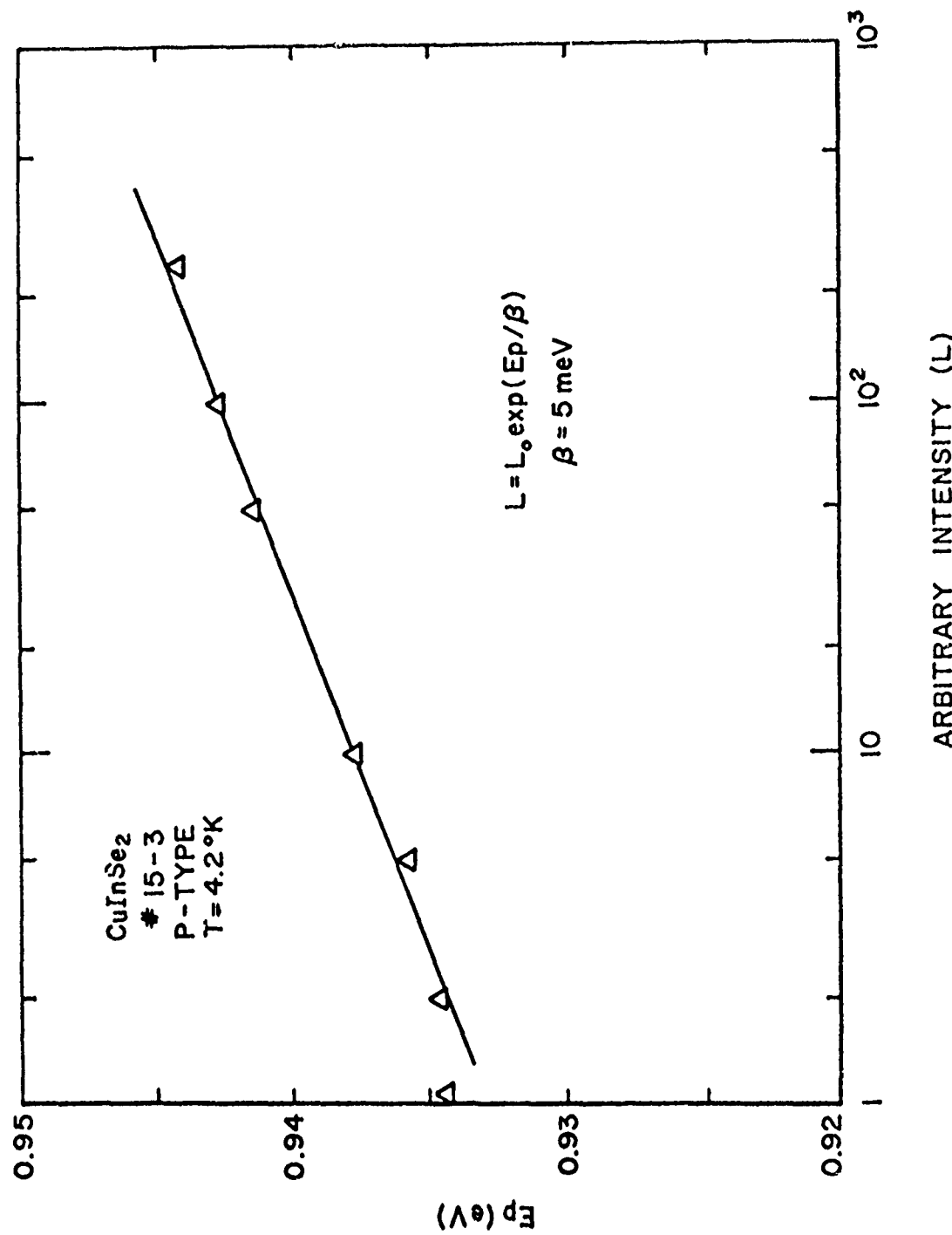


Figure 24. Excitation intensity vs. band peak energy. β is the energy change per decade of excitation intensity.

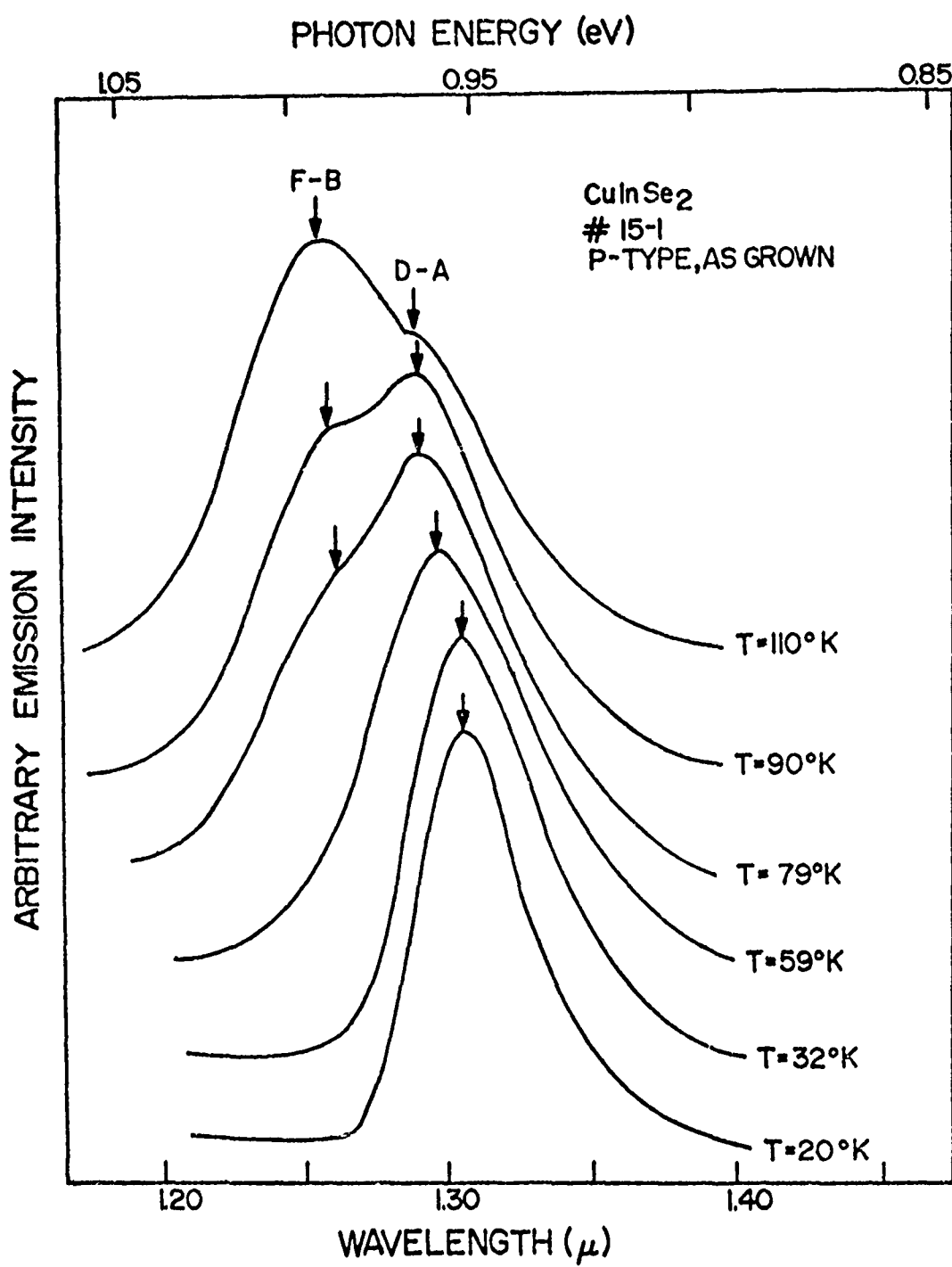


Figure 25. Effect of temperature on the band. D-A \equiv donor-acceptor pair band. F-B \equiv free electron to bound hole to acceptor transition.

$$E = E_g - (E_A + E_D) + \frac{e^2}{\epsilon r^2} \quad (9)$$

where E_g is the band gap, E_A and E_D are the acceptor and donor ionization energy, respectively, and ϵ is the dielectric constant.

A similar band shift with temperature for the donor-acceptor pair band was observed in GaAs⁶³ and InP.⁶⁵ From the present study of the effect of excitation intensity and temperature on the band energy, we find that the broad band dominating at 4.2 °K in the crystals grown under excess Se atmosphere is due to the radiative recombination of donor and acceptor pairs.

When the second band in Fig. 25 is attributed to the recombination of free electrons with holes bound to acceptors ("free-to-bound" recombination), the acceptor ionization energy E_A is found to be 85 ± 2 meV using the relation

$$hv = E_g - E_A + kT \quad (10)$$

and E_g (77 °K) = 1.060 eV, which was determined in Section (III. 1. B) by taking the free exciton binding energy to be 18 meV. The E_A was also obtained from a free-to-bound radiative recombination observed at 4.2 °K (the band "A" in Fig. 16(b)), which yields the same value for E_A . If band "N" in n-type samples in Fig. 16(c) is explained in a similar way as the band "A", $E_D = 65 \pm 2$ meV. Acceptors and donors are Cu and Se vacancies, respectively.

The band-peak energy was influenced by heat-treatment in vacuum and by the presence of a large amount of compensating Cd. Table 6 illustrates the influence by heat-treatment and Cd-doping, β vs the band peak position (ΔE) and β vs the half-width (ΔE) of the band.

TABLE 6. BAND-PEAK ENERGY VS. THE HALF-WIDTH AND THE ENERGY SHIFT PER DECADE OF CHANGE OF EXCITATION INTENSITY (B) IN P-TYPE CRYSTALS GROWN UNDER AN EXCESS Se ATMOSPHERE. ($T = 4.2^\circ\text{K}$).

Sample No.	Crystal	Maximum of Band Peak E_{mp} (eV)	Half-width (eV) ΔE	Energy Change β (meV)
15-1-A	As grown	0.956	0.029	4.1
15-3	As grown	0.944	0.030	5.0
15-3-B	As grown	0.942	0.031	6.4
15-2	As grown	0.931	0.036	8.3
15-F	As grown	0.925	0.040	12
15-2-1	Vacuum Annealing of #15-2, 350 $^\circ\text{C}$, 30 min	0.915	0.04~	14
18-4	Cd-doped ($1 \times 10^{19} \text{ cm}^{-3}$)	0.898	0.064	25

The crystals used were all p-type. Some trends are apparent in Table 6. The energy shift per decade of excitation β becomes larger as E_{mp} shifts to lower energies. ΔE shows a linear increase proportional to β .

Heat treatment causes mainly compensation and uncompensation between the intrinsic defects, and heat-treatment in vacuum may cause an increase in Se vacancies over Cu vacancies in CuInSe_2 . Also, p-type conduction in the Cd-doped crystals indicates that the concentration is larger than that of two types of donors since Cd is known to act as a donor in CuInSe_2 from our work (see Section III. 5). Therefore, it is evident that the broad band in the annealed crystal is involved with more Se vacancies than that in the as-grown crystal. The compensation increases as the band-peak goes to lower energy. β increases with the compensation. The effect of excitation intensity and temperature upon the broad band has been discussed in terms of Eq. (9). However, β was 5 meV for sample no. 15-3. The broader bands in the lower energies have larger values of β . It is apparent that Eq. (9) can not be applied for the bands having $\beta > 10$.

In order to understand the significance of an increase in β with an increase in ΔE , the energy levels expected in heavily doped and compensated materials must be considered. Inversely charged impurities, due to the presence of acceptors and donors, and their fluctuation in concentration create a randomly distributed electrostatic potential in the crystal. The fluctuation of the local potential from place to place in the crystal not only represents the spatially different energy levels of the band edge but also converts

the well-defined deep energy of the impurity centers to a broad energy state. The shape could be represented by the Gaussian function as evidenced by Morgan.⁶⁶ The presence of the fluctuation⁶⁷ leads to localization of carriers in the potential well and influences the position of the Fermi level in compensated materials. The localized carriers should play important roles in the radiative recombination. In p-type CuInSe₂ crystals having a broad pair-emission, when there is no compensation, the Fermi level falls just below the acceptor level. With a gradual increase in compensation, the hole Fermi level should be above the center of acceptor band. Under the above mentioned circumstances, radiative recombination should involve certain tunneling of carriers for the possible donor-acceptor pair band transition. The high-energy edge of the emission spectrum can be expected to be influenced by the position of electron and hole quasi-Fermi levels, while the band shape generally resembles the acceptor band.⁶⁶

The high-energy edge was observed to taper gradually as the emission peak shifted to lower energy; the lower-energy bands are related to higher doping and compensation. This indicates that the electrons do not have a quasi-Fermi level characterized by one electron energy and that the electrons must be in the broad range of energy. The localized electrons in the potential well will be in broader energy states as compensation and doping increase. This clearly explains the large β and the tapering of the high-energy edge as the band shifts to lower energy. The excitation intensity should influence not only the quasi-Fermi level but also the tunneling

distance in the distorted energy band which is due to compensation and doping.

5. ELECTROLUMINESCENCE¹⁸ AND PHOTOVOLTAIC DETECTION^{17,18} IN CuInSe₂

CuInSe₂ can be made usefully both p- and n-type, in contrast to their II-VI analogs. The usefulness of this material is evidenced in the area of solar cells¹⁶ and near-infrared^{14,15} detectors and emitters. We fabricated junction diodes by both diffusion and ion-implantation techniques. The prepared junctions exhibited efficient photovoltaic detection characteristics and efficient electroluminescence. The crystals were grown from an excess Se atmosphere. The crystals having flat as-grown (112) faces were chosen for substrates. Hall measurements showed room temperature mobility of $\sim 9 \text{ cm}^2/\text{V}\cdot\text{sec}$ and hole concentrations $2 \times 10^{16} - 7 \times 10^{16} \text{ cm}^{-3}$. Substrates were etched with a hot solution of HCl:HNO₃ (1:1) before diffusion and ion-implantation. The dopants were Cd for the diffusion and Br, Cl, Cd and Zn for the ion-implantation. Impurity atoms of group-II (Cd, Zn) and group-VII (Br, Cl) acted as donors by replacing Cu and Se on the lattice sites in CuInSe₂. We found out that the ion implantation is better doping technique over the thermal diffusion method. This is also evident when we compared the properties of diffused junctions prepared in p-CuInSe₂:In⁶⁸, n-CuInSe₂:Se¹⁵ and n-CuInSe₂:Cu⁶⁹ by other workers.

A. Cd-diffused CuInSe₂ Junction Diodes

For the diffusion the substrate was placed at one end of an evacuated quartz capsule, and Cd metal shots were placed at the other end. In the fabrication of the junction diodes, p-type substrates

were heat treated for 6-8 min at 400 °C. A p-type crystal ~0.5 mm thick can be readily converted to n-type by annealing for 1 h at 400 °C. For a typical (type-converted) sample, the electron concentration was $2 \times 10^{17} \text{ cm}^{-3}$ and the mobility was $220 \text{ cm}^2/\text{V sec}$. If N_A^0 is the substrate acceptor concentration and at the junction N_A^0 is equal to N_D^0 for a diffusing donor, then the diffusion coefficient D can be obtained from the relation $N_A^0 = N_D^S \text{ erfc} [b/2(Dt)^{1/2}]$, where t is the diffusion time, b is the junction depth, and N_D^S is the surface concentration of the donor being diffused. A diffusion coefficient of $D \approx 5 \times 10^{-7} \text{ cm}^2 \text{ sec}^{-1}$ at 400 °C was calculated for Cd in CuInSe₂ by measuring the junction depth b. Similar rapid diffusion rates have been observed in several II-VI compounds.⁷⁰

The diffused substrate was lapped, except for the naturally grown (112) face, to remove n layers. Then, a mesa structure was made by etching the substrate in a hot HCl:HNO₃ (1:1) solution for a few minutes, the p layer being protected by wax. In order to make the n layer thin, it was etched briefly with the solution after removal of the wax. The ohmic contact was made by sputtering gold onto the p side and In-Sn onto the n side. A rectification ratio of ~1000:1 can be observed at room temperature for forward and reverse voltages at 1 V, as shown in Fig. 26. Also shown is the logarithmic plot of the forward current I versus bias voltage V for the temperature 235-300 °K. The current increases with the Ohmic relation $I \propto V$ in the lower current range. This region is followed by a region closely approximated by $I \propto V^3$, which is

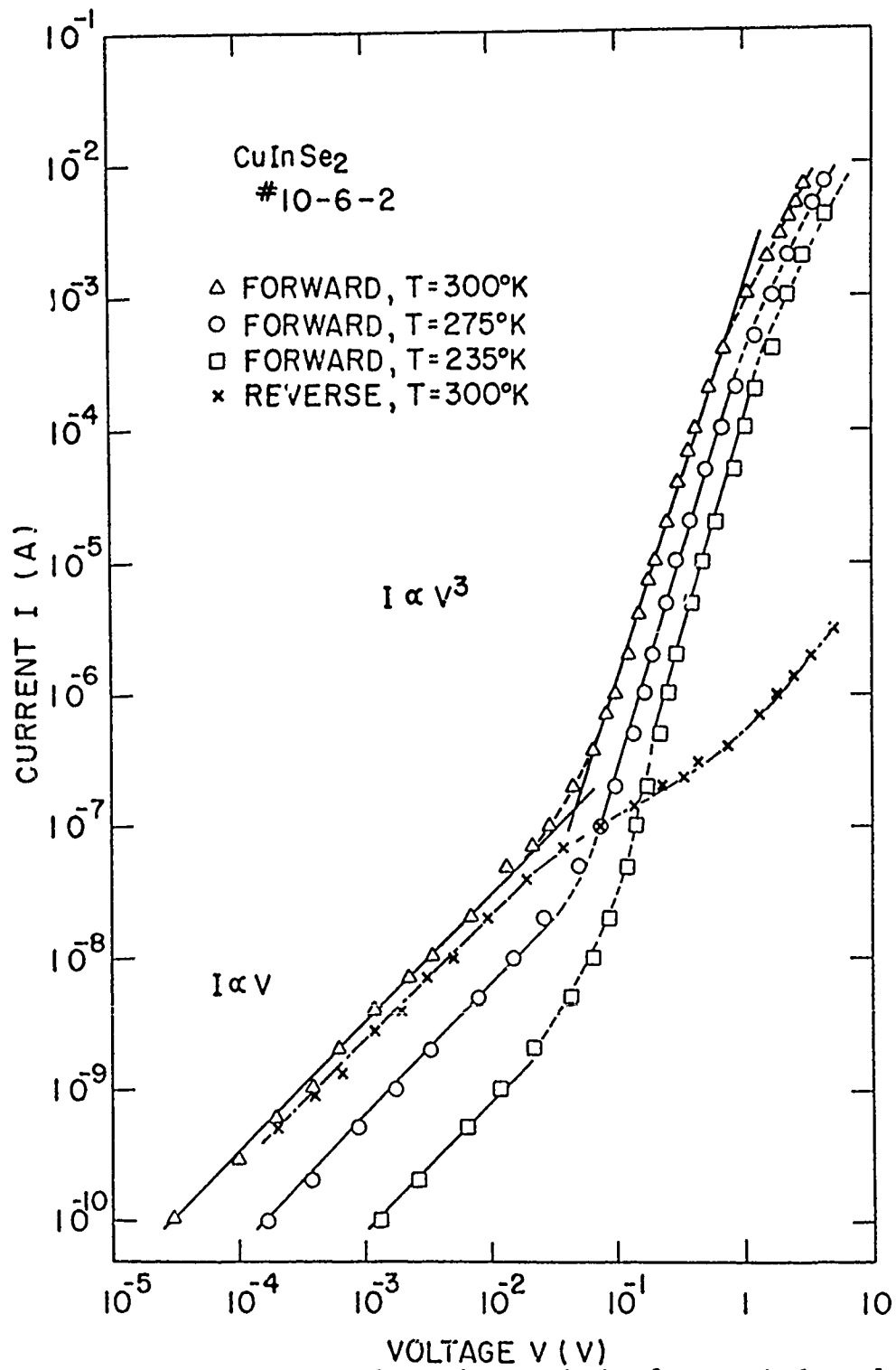


Figure 26. Logarithmic current-voltage characteristics for a typical sample at T = 300, 275, 235 °K for both forward and reverse bias. Solid lines are the fitted curves for the relations $I \propto V^m$ for the forward bias, where $m = 1$ for the low-voltage region and $m = 3$ for the high-voltage region.

characteristic of the two-carrier space-charge-limited current.⁷¹

As the current increases further, the cubic-law region is followed by another short region of an apparent $I \propto V^2$ law. These devices exhibited reverse-bias breakdown voltages of ~60-90 V. The junction capacitance of most diodes at 1 MHz was measured at room temperature. The reverse-bias capacitance is nearly independent of voltage (within ~5%) for voltages up to 10 V. The nondependence of the capacitance upon the applied reverse-bias voltage and the $I \propto V^3$ law for the forward bias indicate that these devices have an intrinsic or highly compensated layer between the highly conducting p and n regions. The magnitude of the capacitance indicates a high-resistivity region of ~13 μ .

The absolute photovoltaic quantum efficiency of these devices for light incident upon the n layer was measured with a calibrated Si solar cell. The efficiency peaks at a wavelength of ~1.2 μ and decreases slowly with decreasing wavelength due to the absorption of the CuInSe₂ n layer. The less efficient diodes show an impurity or intrinsic-defect-related peak at a wavelength of ~1.31 μ . The efficiency shown in Fig. 27 was obtained for typical diodes with a reverse-bias voltage of ≥ 3 V. The efficiency can be made comparable to that of Si by proper controlling of the n-layer thickness.

B. Br, Cl, Cd and Zn Implanted Junctions

Ion implantation was performed at room temperature at an energy of 135 keV to a dose level of 10^{14} to 10^{16} cm^{-2} . Annealing was carried out at 400 °C for 30 min in vacuum in order to reduce the lattice damage through the bombardment and to allow Br, Cl and Zn to substitute for Cu and Se.

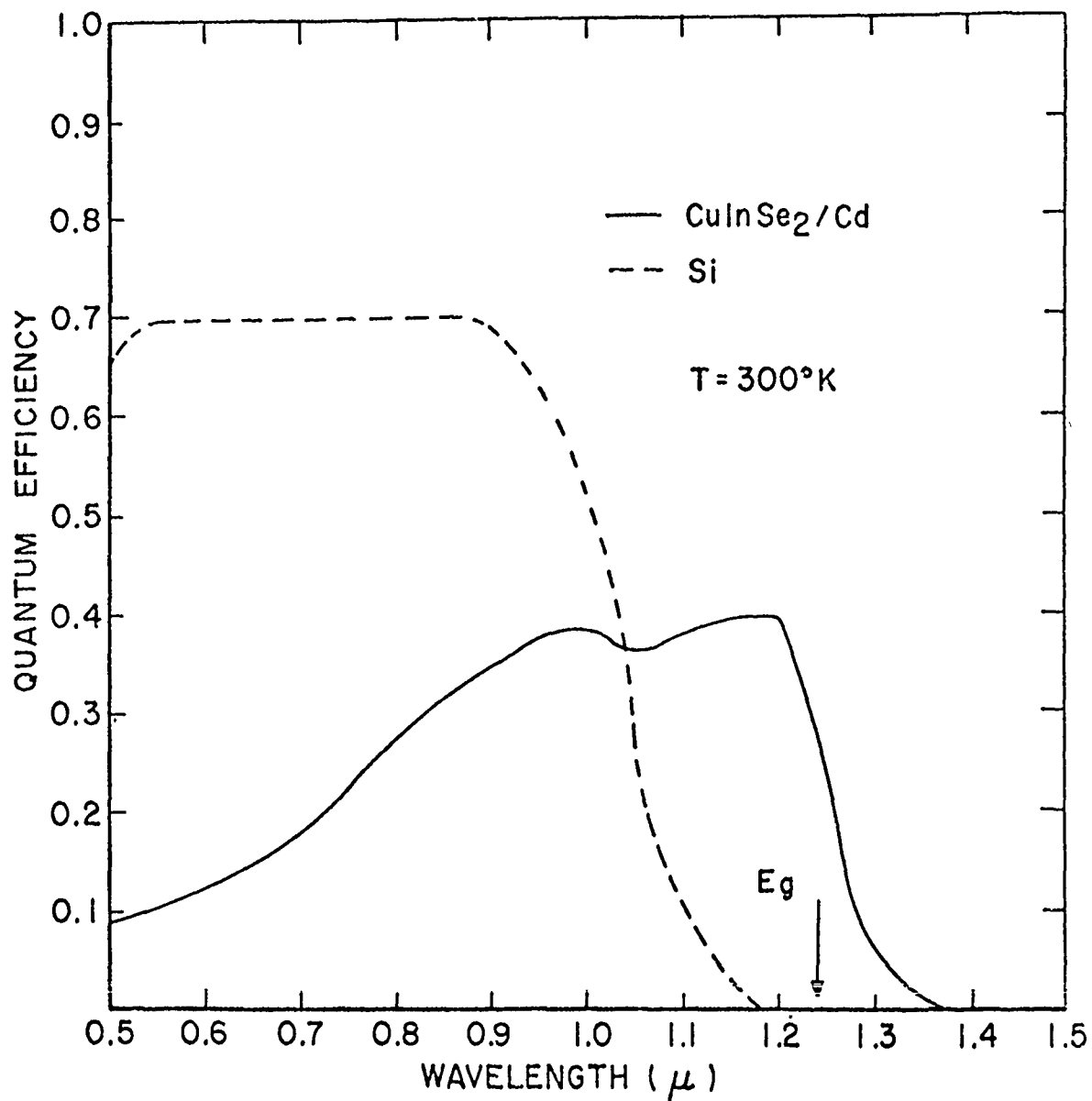


Figure 27. Spectral dependence of the photovoltaic quantum efficiency for a CuInSe₂:Cd homojunction. For comparison purposes, the efficiency of a commercial Si detector is presented.

Hall measurements were carried out on Zn implanted layers, p-i-n structures were made in order to confine the current to the implant layers. Heavy implantation and lower temperature annealing ($<400^{\circ}\text{C}$) were necessary. Implantation was performed to a dose of $1 \times 10^{16} \text{ cm}^{-2}$. Annealing was made at 350°C for 30 min in vacuum. The junction capacitance at 1 MHz was measured at room temperature. The reverse-bias capacitance is nearly independent of voltage up to 10 V. The forward current-voltage relation showed a region closely approximated by $I \propto V^3$. The magnitude of the capacitance indicates an insulating layer of $\sim 30 \mu$. For a typical sample, the implanted layer had a room temperature sheet resistivity of $140\Omega/\square$, an electron concentration of $3.4 \times 10^{14} \text{ cm}^{-2}$, and the mobility of $130 \text{ cm}^2 \text{ V sec.}$

The concentration profile of Zn atoms implanted into p-type CuInSe_2 has been measured by using Auger electron spectroscopy combined with continuous surface layer removal by Ar-ion sputtering at 2 keV. The implantation was performed to a dose of $1 \times 10^{16} \text{ cm}^{-2}$, the samples not being annealed. The thickness of the implanted layer was measured relative to the Ta_2O_5 sputtering rate. The experimentally measured projected range was found to be $\sim 160 \text{ \AA}$. Using LSS theory without channeling, however, the projected range⁷² of Zn in CuInSe_2 can be estimated as $\sim 540 \text{ \AA}$ with a straggling of $\sim 260 \text{ \AA}$ at 135 keV. It can be expected that there is a difference in sputtering rates between CuInSe_2 and Ta_2O_5 , but the relative sputtering rates are unknown. It is possible that the difference between theory and experiment is due to different sputtering rates. Measurements using 100-600 eV Ar ions show that Cu has a sputtering rate about four times greater than Ta.⁷³ The shape of the leading edge of the experimental

concentration profile is in fair agreement with a Gaussian distribution.

However, the concentration profile exhibits an asymmetry as often observed in GaAs⁷⁴ showing a deeper tail in the trailing edge.

The current-voltage characteristics of junctions prepared by implanting Br, Cl, Cd and Zn are shown in Fig. 28. The forward current-voltage characteristics of these diodes can be expressed by $I - I_0 [\exp(eV/nkT) - 1]$ over a considerable range at room temperature. The parameter n is 1.9 for the junctions prepared with Br, Cd and Zn and 2.3 for the junction prepared with Cl. This indicates the formation of p-n junctions. The parameter $n = 2$ shows that the dominant recombination takes place in the space-charge region via deep levels. The rectification ratio at 1 V is 3×10^5 :1, 2×10^5 :1, 2×10^{14} :1 and 8×10^3 :1 for p-n junctions prepared by implanting Br, Zn, Cd and Cl, respectively, as shown in Fig. 28. The series resistances limiting the current flow under forward bias of greater than 0.8 V are generally $\sim 16 \Omega$. The reverse-breakdown voltages were observed to be 4-7 V. Reverse bias capacitance measured at 1 MHz exhibited C^{-3} vs-V relation in the reverse bias range of 0-7 V, which is characteristic of a linearly graded junction.

Efficient electroluminescence was obtained at 77 °K from the forward current of the p-n junctions. Figure 29 shows the electroluminescence spectra obtained with a forward current of 10 mA. The electroluminescence spectra were dominated by a broad-band emission peaking in the wavelength range ~ 1.3 - 1.4μ . However, the peaks of the spectra obtained with p-n junctions prepared even with same ion were observed to change with different substrates. As discussed in

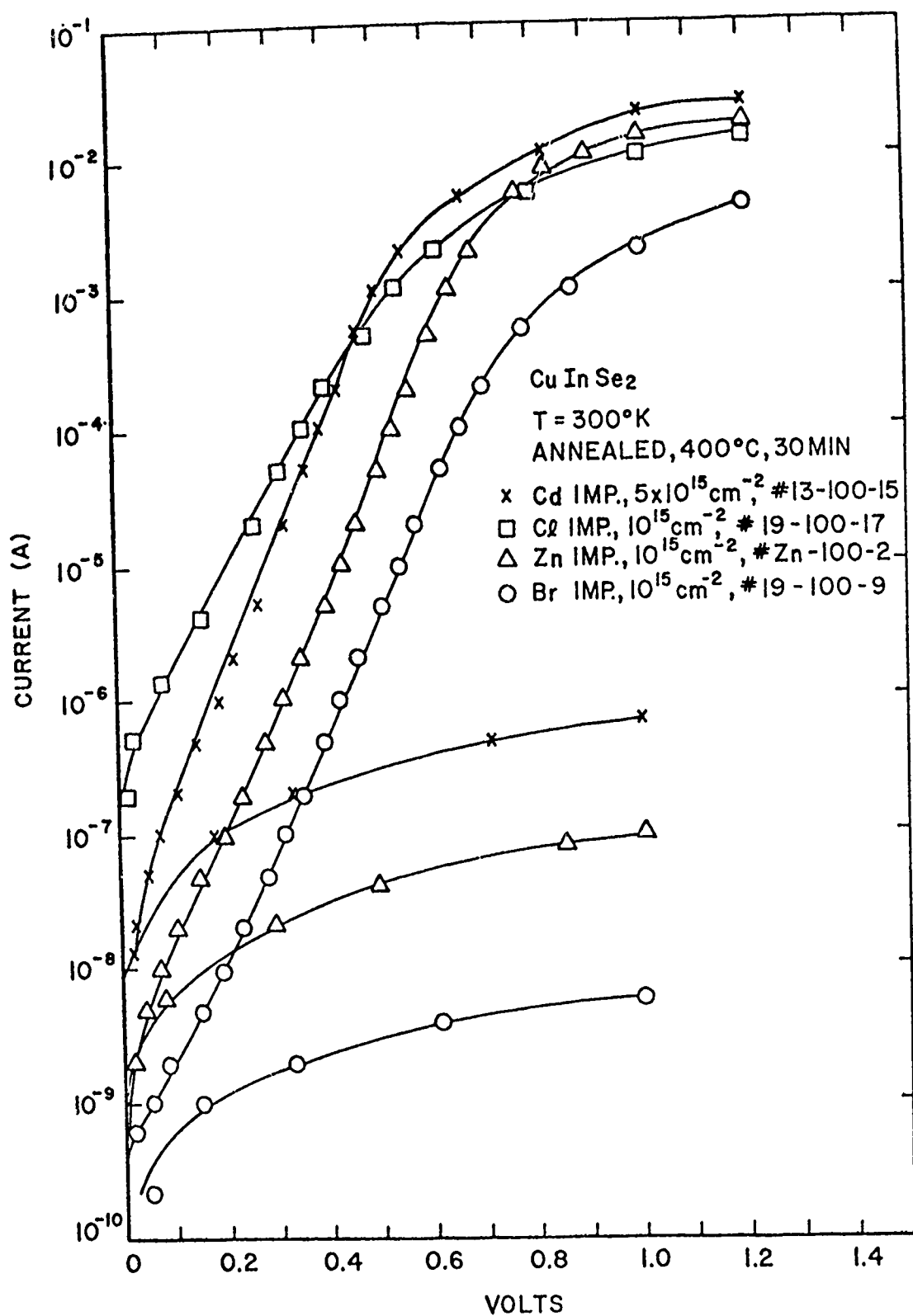


Figure 28. The room-temperature current-voltage characteristics of the p-n junctions prepared by implanting Br, Cl, Cd and Zn.

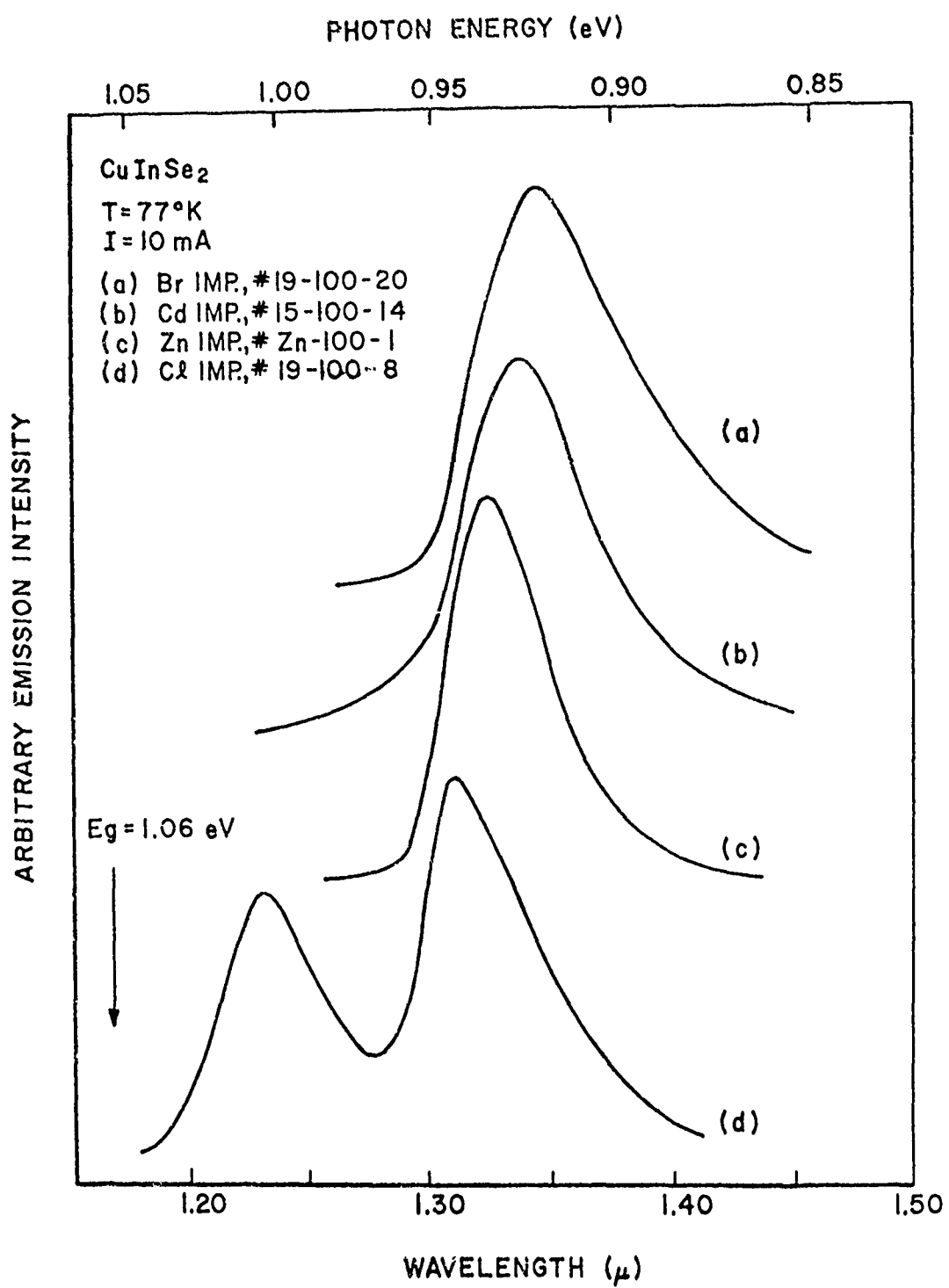


Figure 29. Electroluminescence spectra obtained from the p-n junctions prepared by implanting Br, Cd, Cl and Zn for a current of 10 mA at 77°K.

Section III. 4, broad band emission dominating at low temperatures was attributed to donor-acceptor mechanism with a compensation-dependent band shift. Therefore, the difference in the band-peak energy in junctions made with same-ion implantation can be explained with the different Fermi levels which are determined by the degree of compensation between donor and acceptor. Figure 29(d) shows another emission band peaking $\sim 1.23 \mu$ which lies at shorter wavelength than the pair band. It is believed that this emission is due to Cl donor-to-valence-band transition.

The internal quantum efficiency was measured with a correction being made for the small escape cone at the CuInSe_2 - liquid nitrogen and CuInSe_2 - air interfaces. The internal efficiency was calculated to be 20% at 77°K and $\sim 0.1\%$ at room temperature. The external quantum efficiency was 0.8% at 77°K . The relative light intensity L from the junctions was measured with the forward current I . L - I characteristics can be approximated in the form of $L \propto I^n$ with $n = 2$ in the observed range before a saturation reaches as shown in Fig. 30. This indicates⁷⁵ that the current is mainly due to the recombination of the injected carriers in the space-charge region.

A photovoltaic effect was also observed across the diodes. The implanted layer had a negative voltage with respect to the bulk material. The absolute photovoltaic quantum efficiency of these devices for light incident upon the n-layer was measured for both types of junctions. As shown in Fig. 31, the efficiency is rather uniform at 60-70% for the wavelength between 0.7 and 1.1μ . The efficiency at wavelengths shorter than 0.7μ appears to be influenced

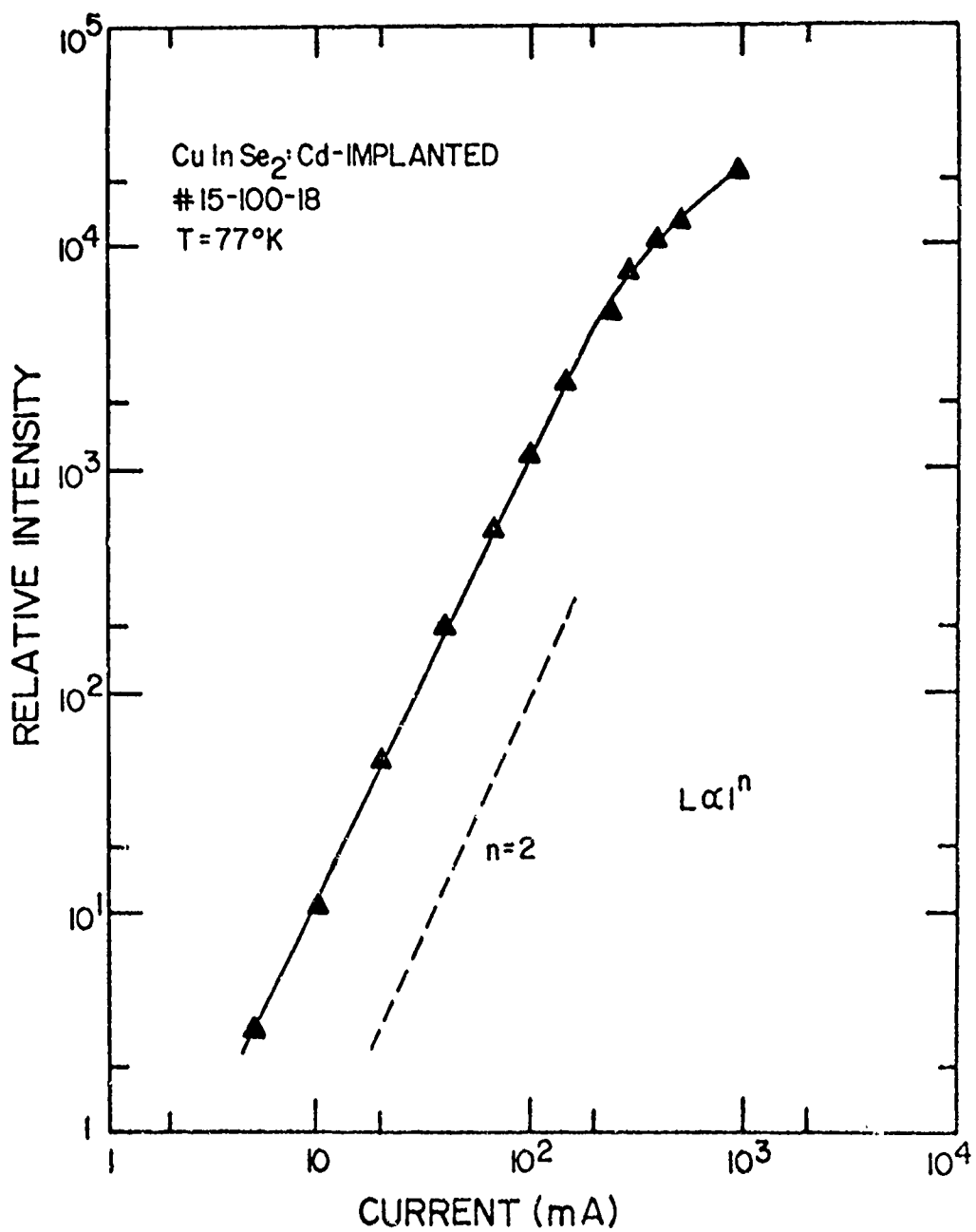


Figure 30. Dependence of relative electroluminescence intensity upon the forward current. The dotted line indicates the relation $L \propto I^n$, with $n = 2$.

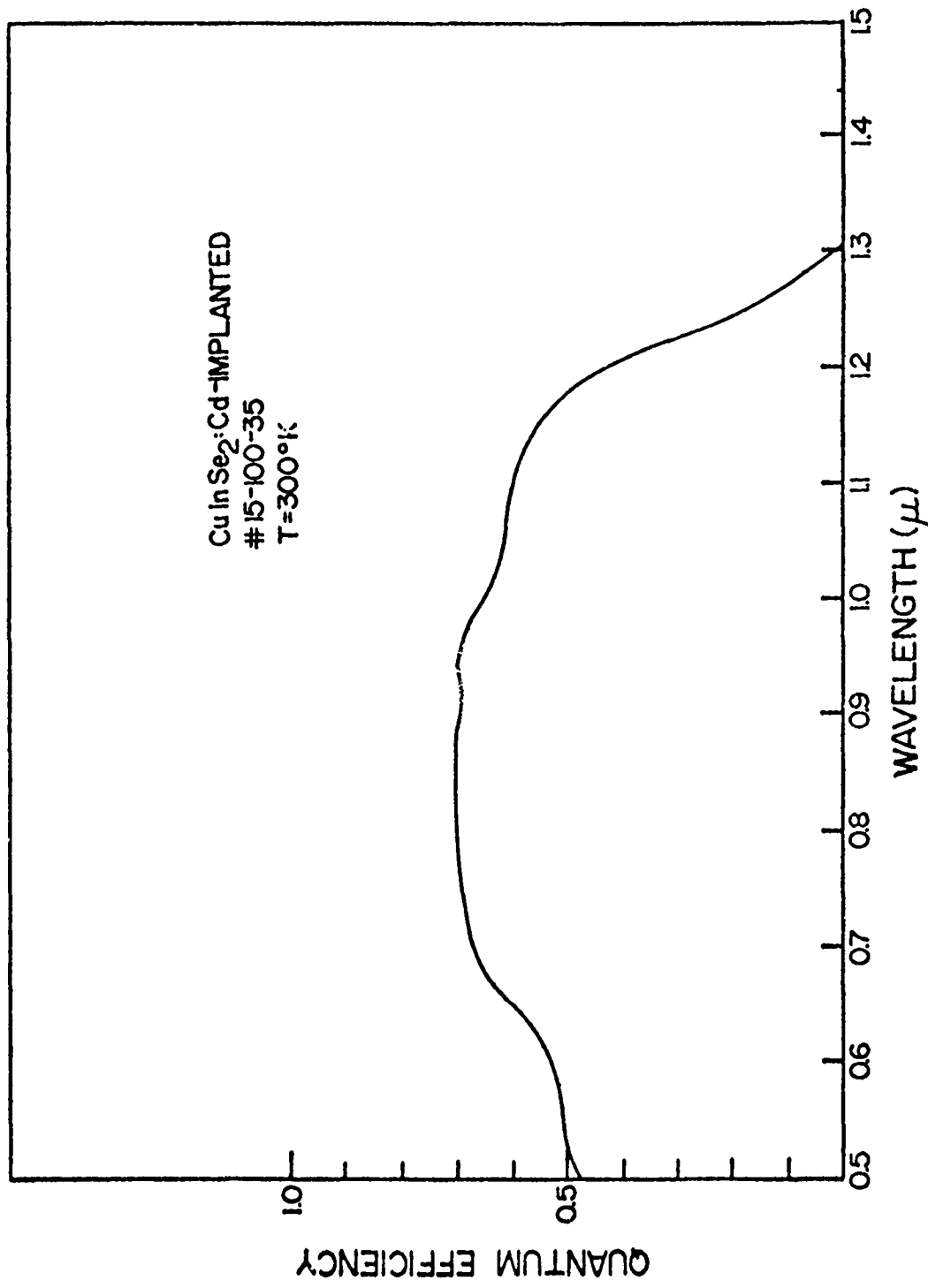


Figure 31. Spectral dependence of the photovoltaic quantum efficiency for a CuInSe₂: Cd homojunction having a reverse bias of 5 V.

by the surface states of the implanted layers. The efficiency shown was obtained for typical diodes having a reverse-bias voltage of ≥ 3 V.

In CuInSe₂ we have found that the ion implantation method has certain advantages over thermal diffusion technique in producing the junctions because the thermal diffusion method has difficulties in controlling diffusion rates and selecting diffusing impurities mainly because of fast diffusion rates at lower temperatures 400-600 °C. This is possibly true for all I-III-VI₂ materials.

6. PHOTOCONDUCTIVITY⁷⁶ IN SEMIINSULATING GaAs

Cr-doped semiinsulating GaAs is widely used as a substrate material in GaAs technology. We discuss the photoconductivity technique as a tool looking into deep levels in semiinsulating GaAs.

The new type of oscillatory photoconductivity here involves a localized phonon. The effect has been observed at T = 18-23 °K in three samples of semiinsulating GaAs, obtained from three different sources. The samples were etched in 5H₂O: 1H₂O₂: 1H₂SO₄ and ultrasonically bonded with pure In. Figure 32 shows the photoconductive spectral response per unit photon for a crystal of semiinsulating GaAs at T = 23 °K. In Fig. 33 we have plotted the energies of the minima of three samples vs the number of the minimum.

The straight line intercept gives an ionization energy of 6075 cm⁻¹ or 0.753 \pm 0.004 eV and a period of 168 cm⁻¹ or 20.5 meV.

There is considerable evidence that the 0.75 eV in GaAs is due to oxygen. It has been commonly seen in most melt-grown and VPE epitaxial crystals.⁷⁷ Ionization energies of approximately 0.75 eV have also

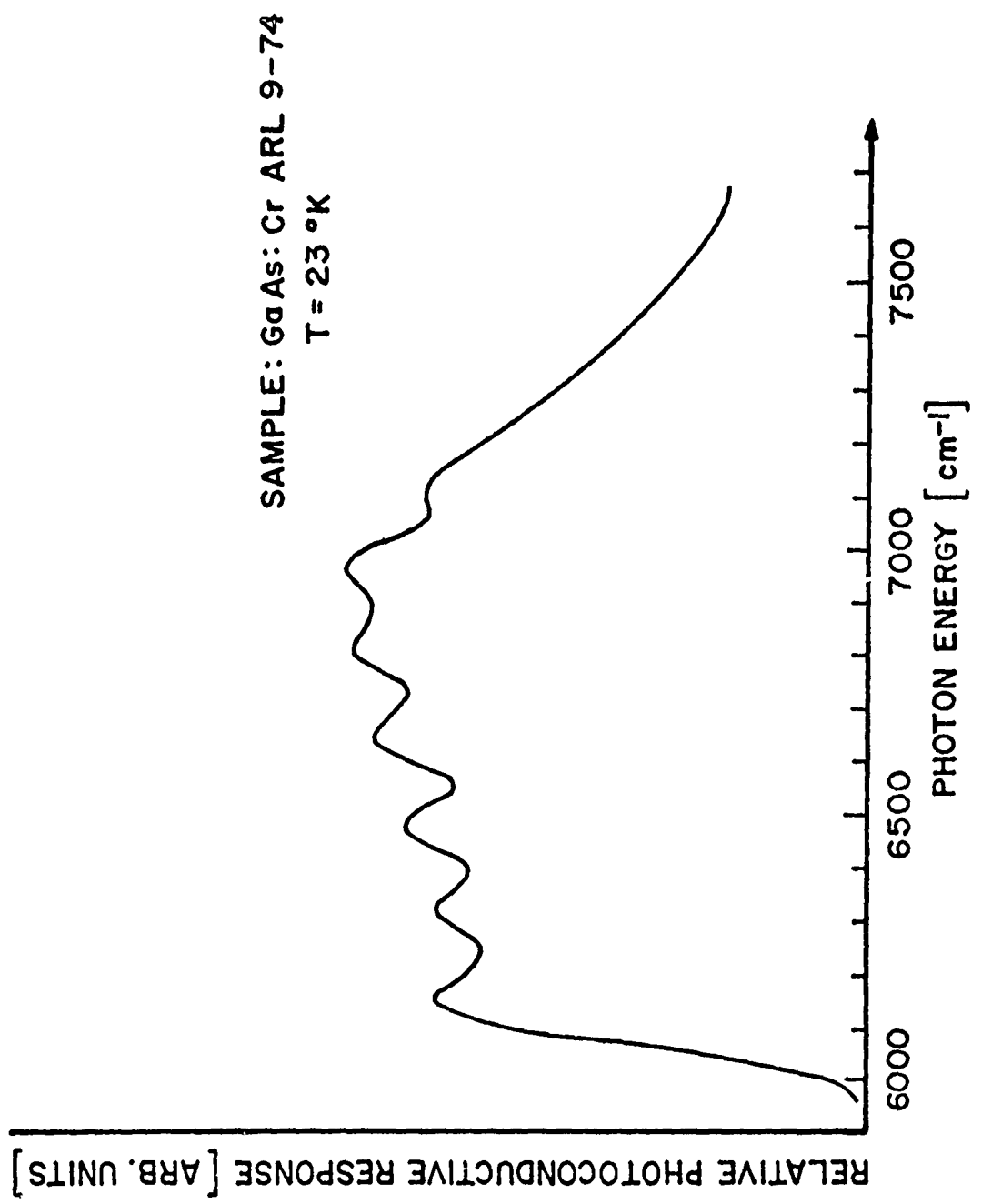


Figure 32. Photoconductive spectral response per unit photon for a sample of semimetallic GaAs.

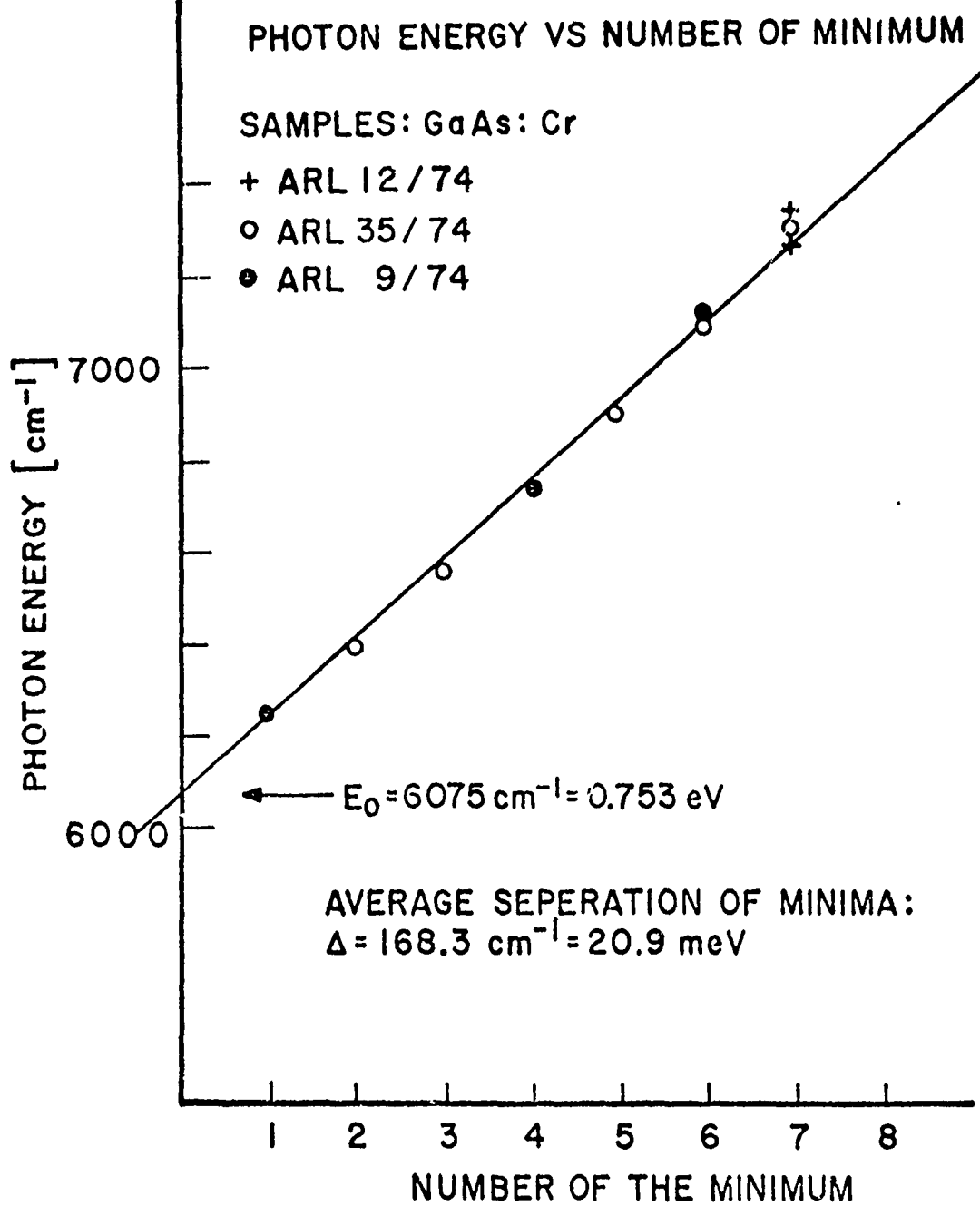


Figure 33. Wavenumber of the minima vs the number of the minima for three samples of semiinsulating GaAs.

been observed in GaAs deliberately doped with oxygen.⁷⁸ It also has been clearly identified by deep level transient spectroscopy.⁷⁹ Even though the exact nature of the 0.75 eV level is not known with certainty, we therefore follow the notation of Ref. 79 and call this level GaAs:0. Our samples were analyzed mass-spectrographically and showed the presence of Cr in two of the three samples. In these two samples an additional broad peak at 0.87 eV superimposed on the oscillations shown in Fig. 32, was observed in the photoconductive spectral response. We believe that the 0.87 broad peak⁸⁰ is due to Cr, while the 0.75 eV level is either due to oxygen or possibly is more complex defect. Our photoconductivity results show this peak to be quite sharp, considerably less broad than other deep centers in GaAs. Near infrared photoconductivity at liquid He temperatures thus seem to be an excellent diagnostic tool for the study of GaAs:0.

The period of 20.9 meV is slightly larger than 1/2 of the $k = 0$ LO phonon energy, $\hbar\omega_0 = 36.75$ meV (296.456 cm^{-1}). This energy does not correspond to any other zone boundary phonon,⁸¹ in fact it falls approximately into the region where the frequency distribution $G(\omega)$ has a minimum.⁸² Simple theory⁸² predicts that there might be a localized mode of energy higher than $\hbar\omega_0$ but none lower for GaAs:0. Gross et al.⁸³ have recently studied localized vibrations associated with the $V_{\text{As}}\text{Cu}_{\text{Ga}}$ and $\text{Cu}_{\text{Ga}}V_{\text{As}}\text{Cu}_{\text{Ga}}$ complexes in GaAs by luminescence techniques and found vibrational lines corresponding to 3.57 and 5.13 meV. These appear to be resonance modes of these complexes.

TABLE 7. SAMPLES OF Cr-DOPED GaAs

SAMPLE	SOURCE	MASS SPECTROSCOPIC ANALYSIS DISLOCATION			REMARKS
		PPM Cr	PPM Fe	DENSITY (EPD)	
ARL 2-74	MIT (LDL 1099)	0.6	0.04	1.3x10 ⁵	
ARL 9-74	McDD (Bell & Howell #3675	-1	-0.4	<10	
ARL 12-74	MONSANTO	<0.03	0.7	3x10 ⁵	
ARL 35-74	TI	0.5	0.05	4x10 ⁵	
ARL 43-74	LASER DIODES LDL #2782	1	0.05	8x10 ³	
ARL 44-74	LASER DIODES LDL #418	1	0.1	2x10 ⁵	
ARL 48-74	LASER DIODES LDL #2656				Substrate Only
ARL 49-74	RCA #1886				5 μ m Cr - doped Epilayer on LDL 2656
ARL 50-74	RCA	Unknown	Unknown	Unknown	1 μ m n-type Epilayer on LDL 2656
ARL 51-74	RCA	Unknown	Unknown	Unknown	1 μ m n-type Epilayer on 5 μ m Cr Epilayer

Figure 34 shows the photoconductive spectrum of six semiinsulating samples at $T = 20^{\circ}\text{K}$. It clearly shows the sharp threshold at 0.75 eV which we attribute to oxygen in the five of the six samples. Properties of various kind of Cr-doped GaAs are listed in Table 7. We see the oscillation in these samples.

7. D. C. ELECTROLUMINESCENCE IN ZnS

We have observed that it is possible to produce D. C. electroluminescence in a variety of powders that were copper coated. Light output of the better cells is estimated to be 20-30 ft-lamberts, typically at 150 volts and 10 millamps/cm² current. We have also determined that luminescence occurs only at the anode. If the polarity is reversed, the light output diminishes at the side which previously was the anode and "reappears" at the other side. In a few seconds light is emitted by from the new anode side.

We have shown that it is not necessary to make sandwich type cells to check the suitability of a phosphor. The D. C. electroluminescence can in fact be observed on a large "pile" of phosphor simply by making contact to one end with a wire or piece of metal used as the cathode and using a tin oxide coated glass slide as the anode. This simple technique works well, and, so far at least, we have not observed any case where the sandwich structure gave clearly better light output. For high resistance phosphors, no light output is observed sometimes, but this is true for both "pile" and "cell" structures.

A typical spectrum of the D. C. luminescence of a Mn-doped ZnS-powder is shown in Fig. 35. The light output, which peaks at 5800

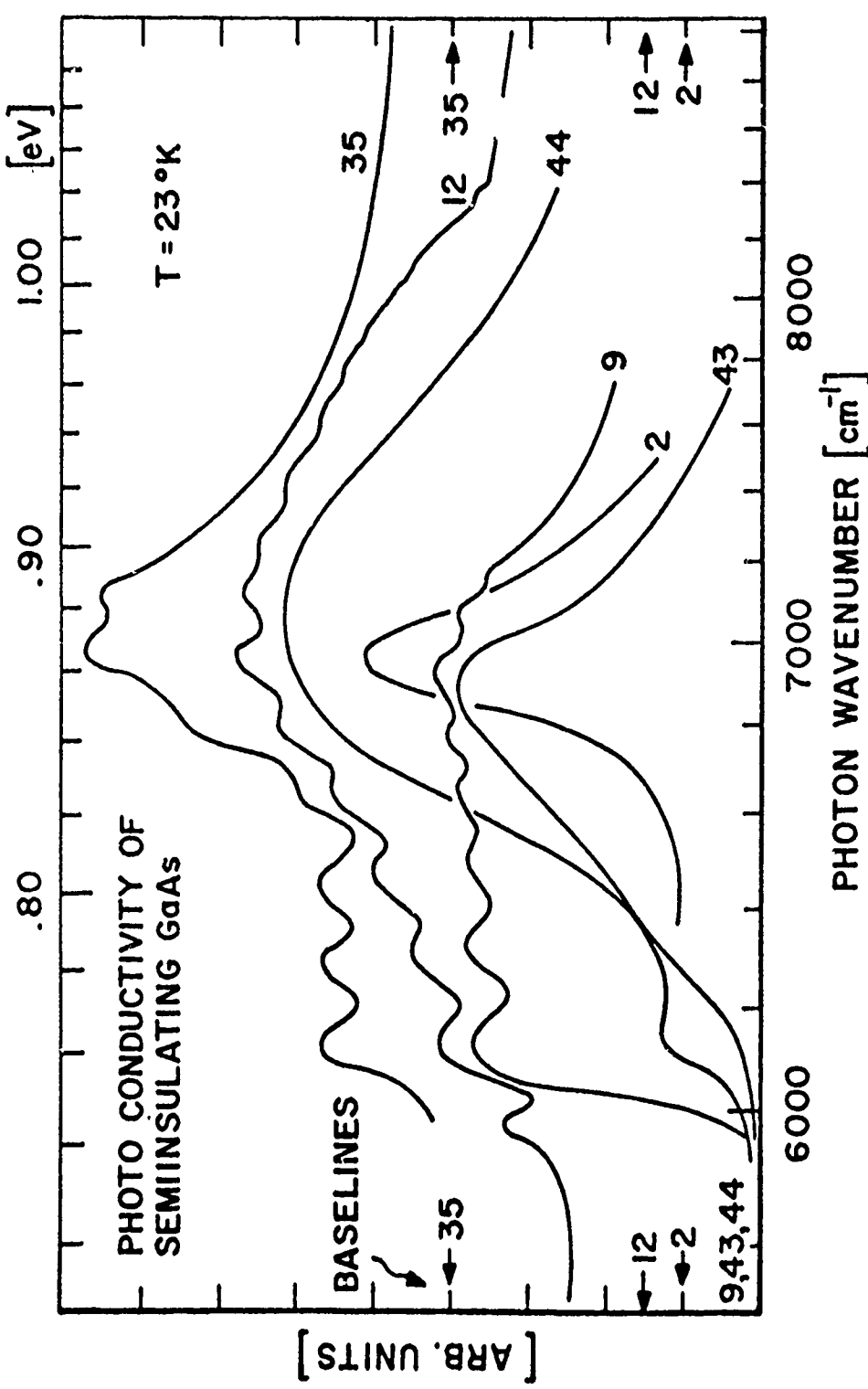


Figure 34. Photoconductive response of six samples at $T = 23^{\circ}\text{K}$.

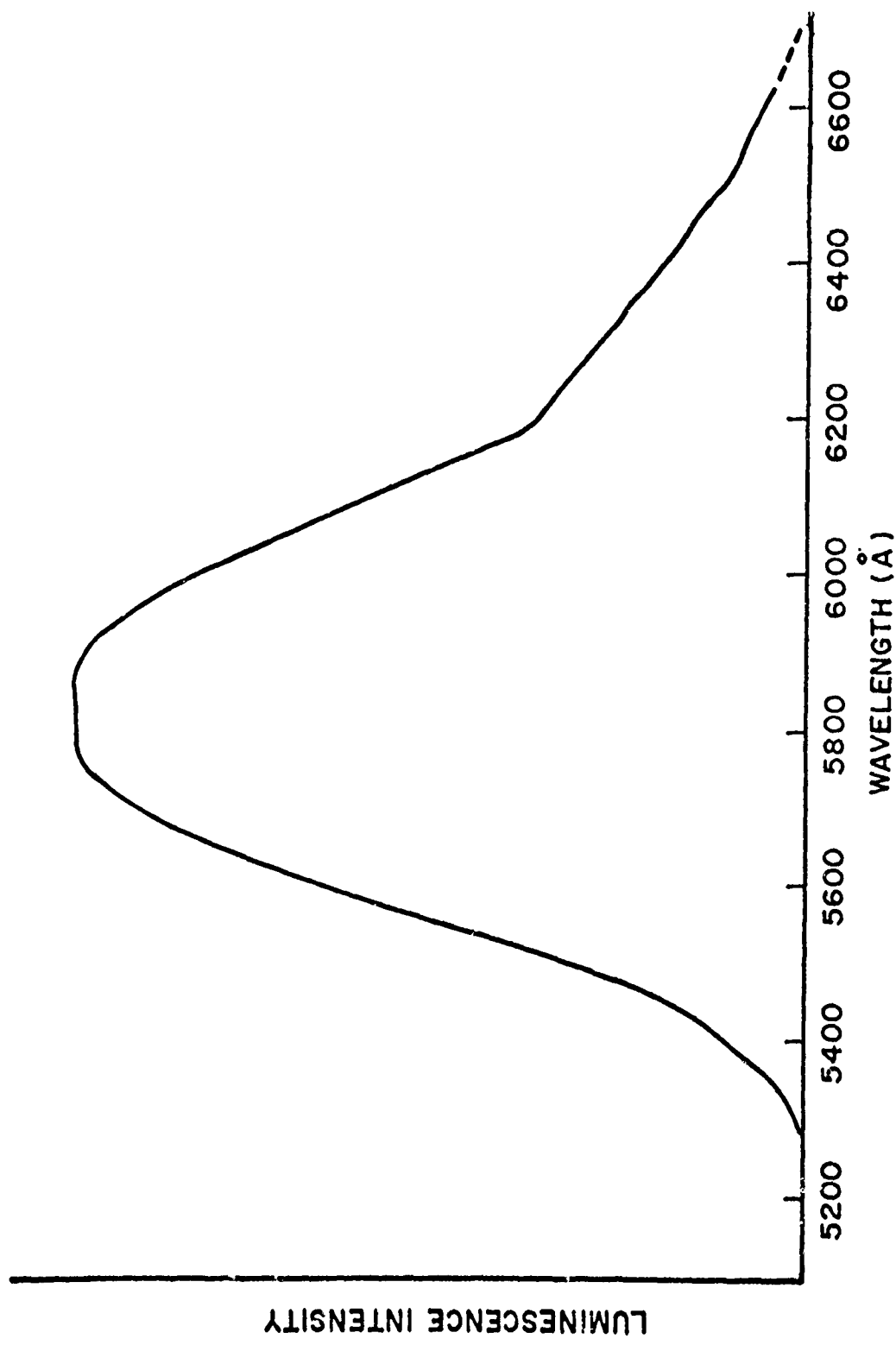


Figure 35. D. C. Electroluminescence spectrum of Mn-doped ZnS.

Angstroms, appears yellow to the eye. Our efforts to develop phosphors with different colors have so far not been successful. This is not surprising in view of the similarly unsuccessful search by Vecht and other researchers. While different spectra have been observed, the efficiency of these phosphors is usually three orders of magnitude lower than that of Mn-doped ZnS.

We have established a strong correlation of luminescence efficiency and particle size by a number of experiments. Since it is desirable to have particles of much smaller size than the approximately 10 micron diameter size of commercial phosphors, we have initiated a twofold attack on this problem:

- 1) by further pulverization of present powders by a commercial firm and
- 2) by precipitation of ZnS powders directly from solution.

The latter process can be described by the following steps: After dissolving pure Zn in acetic acid, NH_4OH (Ammonium Hydroxide) is added and H_2S is passed through solution to precipitate ZnS.

SECTION IV

ELECTRICAL TRANSPORT PROPERTIES

1. HIGH RESISTIVITY HALL SYSTEM

High resistivity values are commonly encountered when the electrical properties of semiconducting compounds such as Cr-doped GaAs and III-VI compounds. In order to characterize these materials, a knowledge of the various transport properties is essential to the understanding of the processes responsible for its behavior. Apparatus necessary to measure resistivity and Hall effect was built for application to those materials. Three electrometers (Keithley Model No. 610 CR, input impedance not less than $\sim 10^{14} \Omega$) were used as unity gain amplifiers as shown in Fig. 36. These amplifiers function as impedance matching devices so that the time constant can be reduced for the measurements. Between the Dewar and the unity gain amplifier inputs, triaxial cables are used with the outer shield common to the Dewar and circuit ground. The guard is connected into Dewar by means of several isolated coaxial feed throughs.⁸⁴

Temperature is controlled by a calibrated platinum or Ge sensor. The coaxial feed throughs are connected to a Heli-tran Dewar.⁸⁵ A magnetic field of 7000 G was usually used in the Hall measurements.

2. ELECTRICAL PROPERTIES⁸⁶ OF CuGaS₂

This section describes electrical transport properties of CuGaS₂ crystals produced by two different methods, melt-growth

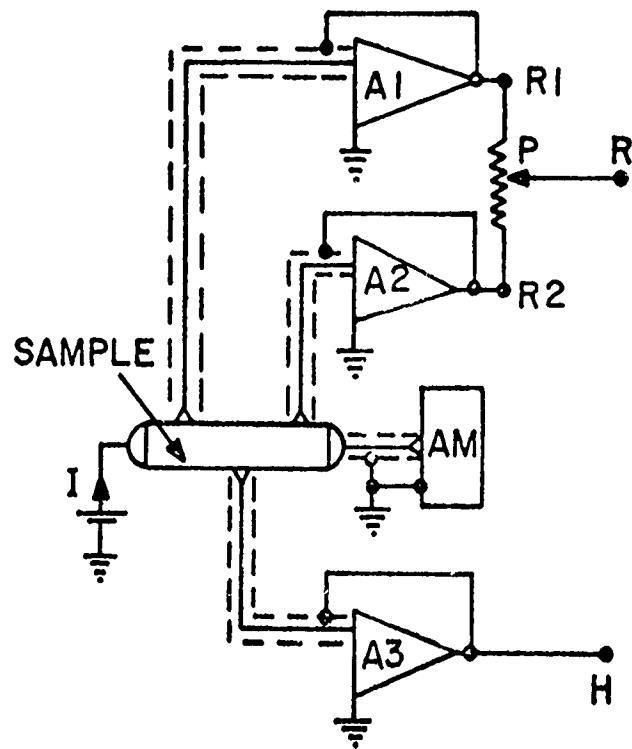


Figure 36. Guarded Hall system employing three unity gain amplifiers A_1 , A_2 , and A_3 . AM is an electrometer ammeter operated in a feedback mode.

and vapor-phase transport. Since intrinsic defects are involved in conduction mechanism all the samples were annealed in excess Sulfur atmosphere. Heat-treatment was done at a temperature of 400-600 °C for 2-7 days.

A. Resistivity and Hall Coefficient

Table 8 summarizes room temperature electrical characteristics. Figures 37 and 38 show the temperature dependence of resistivity and hole concentration. Hall-effect data were analyzed on the assumption that $p \sim 1/R_H$ and the well-known expression for nondegenerate statistics of a single level,

$$p(p + N_D)/(N_A - N_D - p) = (N_V/g) \exp(-E_A/kT), \quad (11)$$

gives optimized values of N_A , N_D , E_A , and m^* , where the hole concentration p is related to the acceptor density N_A , activation energy E_A , acceptor impurity degeneracy g , and the compensating donor density N_D . The quantity R_H is the Hall coefficient, and N_V is the density of state of the valence band, given by $2(2\pi m^* kT/h^2)^{3/2}$, where m^* is the valence-band density-of-state mass. This model neglects the impurity excited states. The degeneracy factor g is given by the impurity state and the valence-band structure of the material. CuGaS₂ is a direct-band-gap material with an energy gap of 2.53 eV at 2 °K and 2.40 eV at 298 °K.⁸ The highest valence bands of CuGaS₂ consist of A and B, C bands separated by the influence of a noncubic crystalline field and spin-orbit interactions. The A and B, C bands are separated by an energy of ~0.12 eV. The B and C bands are almost superimposed.

TABLE 8. SOME ROOM-TEMPERATURE ELECTRICAL CHARACTERISTICS
OF THE SAMPLES MEASURED AT DIFFERENT HEAT-
TREATMENT TEMPERATURE.

Sample No.	Method of growth	Heat-treatment temperature (°C)	ρ (Ω cm)	p (cm^{-3})
MAS	melt	as-grown	3.2×10^6	4.2×10^{11}
IAS	vapor	as-grown	1.0×10^2	2.9×10^{15}
I40	vapor	400	7.4×10^1	3.9×10^{15}
M42	melt	420	5.5×10^1	5.6×10^{15}
I50	vapor	500	5.2	6.0×10^{16}
M59	melt	590	1.9	1.9×10^{17}
I66	vapor	660	5.8×10^{-1}	5.4×10^{17}
M66	melt	660	6.4×10^{-1}	5.4×10^{17}

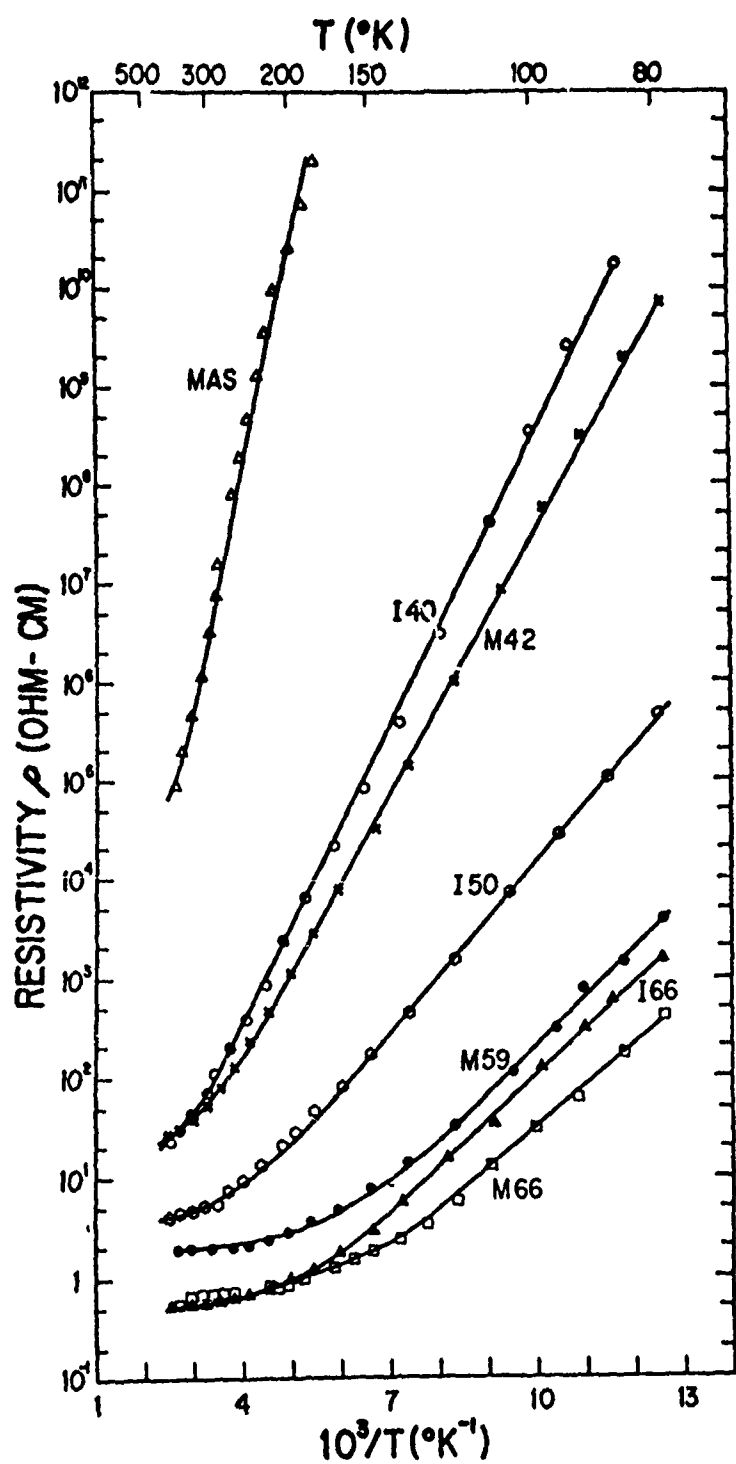


Figure 37. Temperature dependence of the resistivity of the samples heat treated at different temperatures as shown in Table 8. M, indicates the melt-grown crystals, I, is for the crystals grown from the vapor.

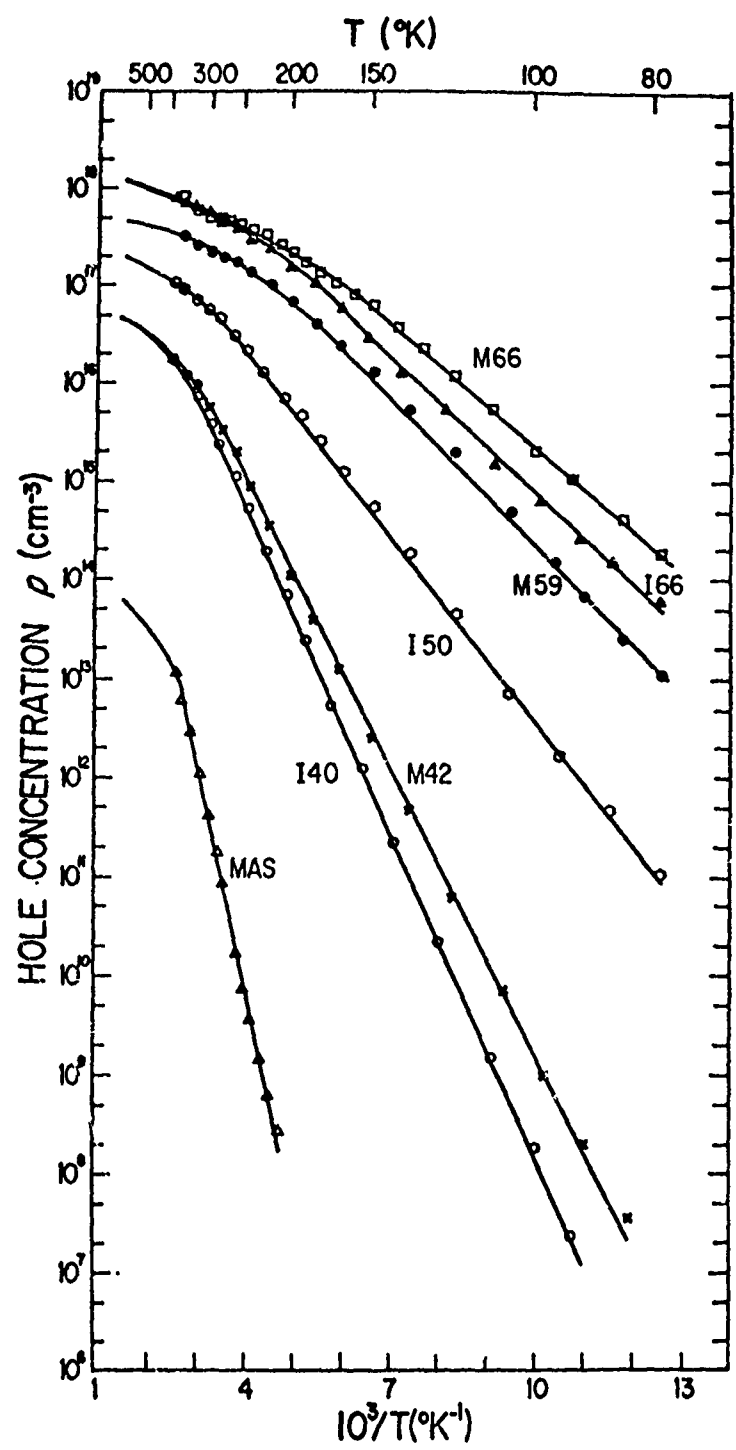


Figure 38. Temperature dependence of the hole concentration of the samples heat treated at different temperatures as shown in Table 8. The symbols represent experimental points while the solid lines represent the fit as discussed in text.

The parameters N_A , N_D , E_A and m^* were obtained from the fitted data with Eq. 11. $m^* = 0.69$ me was obtained by averaging for all the samples in Tab¹ 8. The computer fit was made with the fixed value $m^* = 0.69$ me in obtaining E_A , N_A , and N_D . Table 9 lists the parameters E_A , N_A , and N_D . The solid lines in Fig. 38 represents the respective computer fit to the data.

The acceptor activation energy strongly depends on the acceptor density. The acceptor concentration ranged from $\sim 10^{15}$ to 10^{18} cm^{-3} , depending on the temperature of the heat treatment with the excess sulfur pressure. As-grown samples from the melt show lower hole concentration than those from the vapor transport. Iodine incorporation in the crystals can be expected as a replacement for sulfur, which could give a donor due to its lower negative valence; however, no n-type CuGaS_2 was obtained. Two types of crystals showed almost the same behavior with the heat treatment.

The impurities for extrinsic acceptors could be the ones which belong to columns II, V, and VIII, substituting for the host atoms. Our crystals were not doped with any p-type impurities intentionally. Our acceptor concentration increased with increasing annealing temperature. If foreign impurities are involved, the concentration should be independent of the heat-treating temperature. The acceptor is, therefore, from intrinsic stoichiometric origin. Cu vacancies are probably the intrinsic acceptors, as indicated by Tell and Kasper.⁸⁷ Compensating donors also increase with the increase of the temperature. However, the compensation ratio $k = N_D/N_A$ shows the general tendency of decreasing with the increase

TABLE 9. LEAST-SQUARES-FITTED VALUES FOR IMPURITY DENSITY, ACTIVATION ENERGY, AND COMPENSATION RATIO.

Sample No.	E_A (eV)	N_A (cm^{-3})	N_D (cm^{-3})	$K = (N_D/N_A)$
MAS	0.39	5.6×10^{14}	4.7×10^{14}	0.84
IAS	0.20	1.4×10^{17}	6.8×10^{16}	0.49
I40	0.20	8.7×10^{16}	3.7×10^{16}	0.43
M42	0.17	1.2×10^{17}	5.8×10^{16}	0.49
I50	0.11	4.2×10^{17}	1.7×10^{17}	0.40
M59	0.092	6.4×10^{17}	1.5×10^{17}	0.23
I66	0.078	2.4×10^{18}	4.2×10^{17}	0.18
M66	0.073	1.7×10^{18}	1.9×10^{17}	0.11

of the heat-treating temperature. The vacancies of sulfur atom may have two charged states, one of which appears to be a compensating donor. This may be responsible for the increase of resistivity with heating in vacuum or under minimum sulfur atmosphere.

It may be possible to speculate on various possible reactions explaining the heat treatment as studied on various materials by Kroger.⁸⁸ The concentration of Cu vacancies can be approximated with the following expression:

$$V_{Cu} = A \exp(-\Delta H/kT), \quad (12)$$

where A is a factor related to the heat-treating temperature and sulfur pressure. The $\ln N_A$ versus the reciprocal of the heat-treatment temperature curve gives ~0.68 eV as the Cu vacancy formation energy in $CuGaS_2$ as shown in Fig. 39.

B. Concentration Dependence of Activation Energy

Shallow, hydrogenlike impurity levels show a decrease in activation energy with an increase of acceptor concentration. With an acceptor-type impurity, the decrease should vary as the cube root of the acceptor concentration, as proposed by Pearson and Bardeen⁸⁹ and Debye and Conwell.⁹⁰

$$E_A = E_{A0} - \beta N_A^{1/3}, \quad (13)$$

where E_{A0} is the activation energy at the dilute limit of acceptor concentration and β is a proportional constant which depends on E_{A0} , the radius of the acceptor ground states, and the average

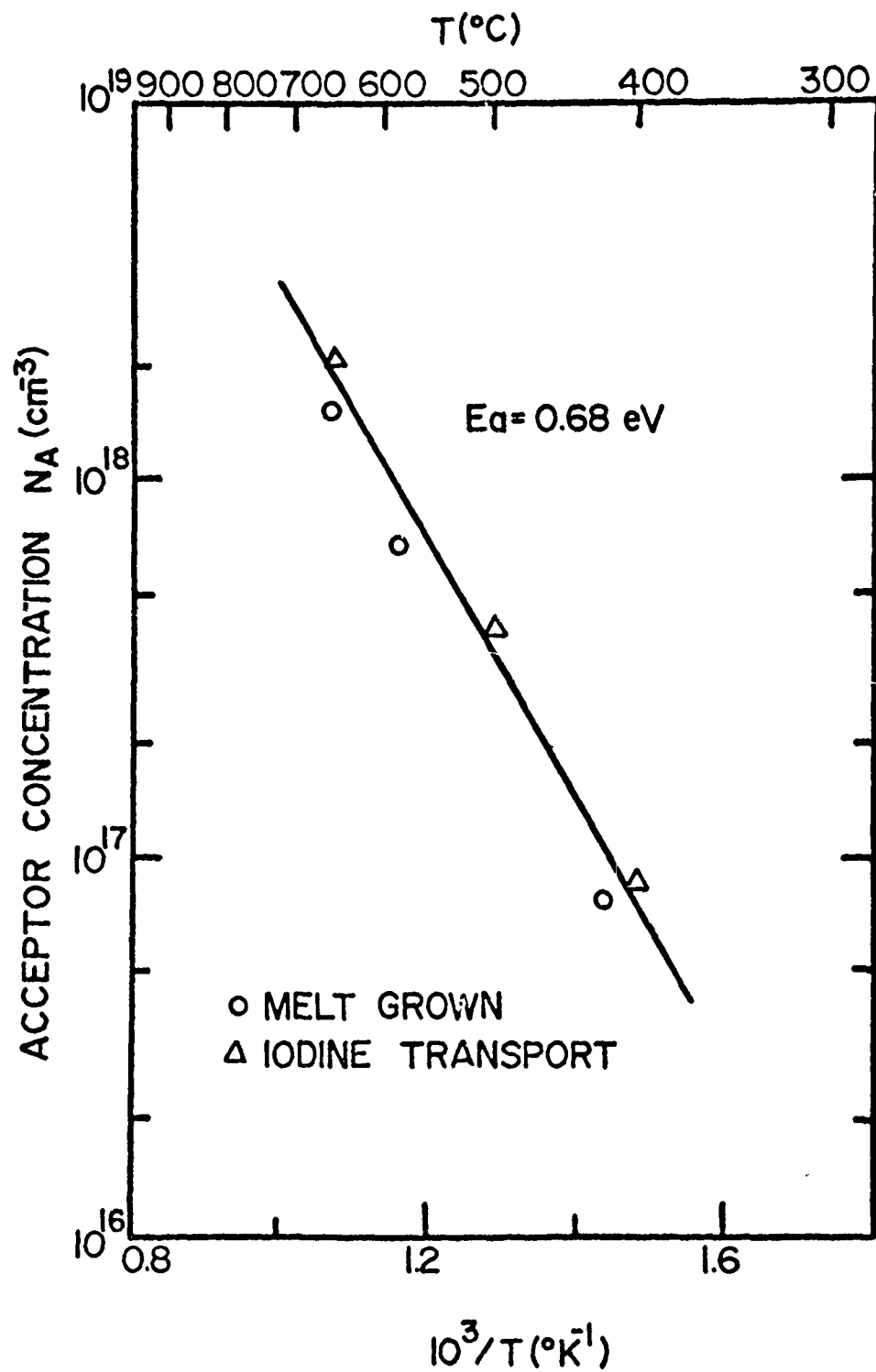


Figure 39. The acceptor concentration vs the inverse of heat-treatment temperature. The solid line yields ~ 0.68 eV as a formation energy of Cu vacancies.

acceptor separation. The β is $\sim 2.4 \times 10^{-8}$ eV cm in Ge.⁹⁰ This value was confirmed for a rather deep Cu acceptor in Ge with a relation similar to Eq. (13) by Norton and Levinstein.⁹¹

The value of E_{A0} at the dilute limit can be obtained from an estimate of the effective mass by using the hydrogen model

$$E_{A0} = 13.6(m^*/m_e)/\epsilon^2 \text{ (eV).} \quad (14)$$

The activation energy for p-CuGaS₂ is ~ 0.13 eV with $\epsilon = 8.5$ (Ref. 92) and $m^* = 0.69 m_e$. The activation energy versus the cube of the acceptor concentration is presented in Fig. 40. The activation energy generally increases with a decrease of acceptor concentration and increases with an increase in the compensation ratio $k = N_D/N_A$. The dotted line in Fig. 40 shows the curve fitted with $\beta = 2.4 \times 10^{-8}$ eV cm for activation energies lower than the hydrogenlike acceptor activation energy. This line gives ~ 0.11 eV as the thermal activation energy for a situation of infinite impurity dilution. The mean activation energy of a Cu \backslash cancy acceptor may, therefore, be estimated as ~ 0.12 eV. However, our data show a higher slope as indicated by the solid line in the activation energy range larger than ~ 0.12 eV. This may be due to the fact that the holes liberated from the uncompensated acceptors concentrate in the deepest wells of the potential resulting from the large-scale fluctuation in the charged distribution due to heavy compensation. Shklouskii and Efros,⁹³ for example, have shown that for a compensated semiconductor with compensation near unity, the Fermi level falls below the hydrogenic impurity level.

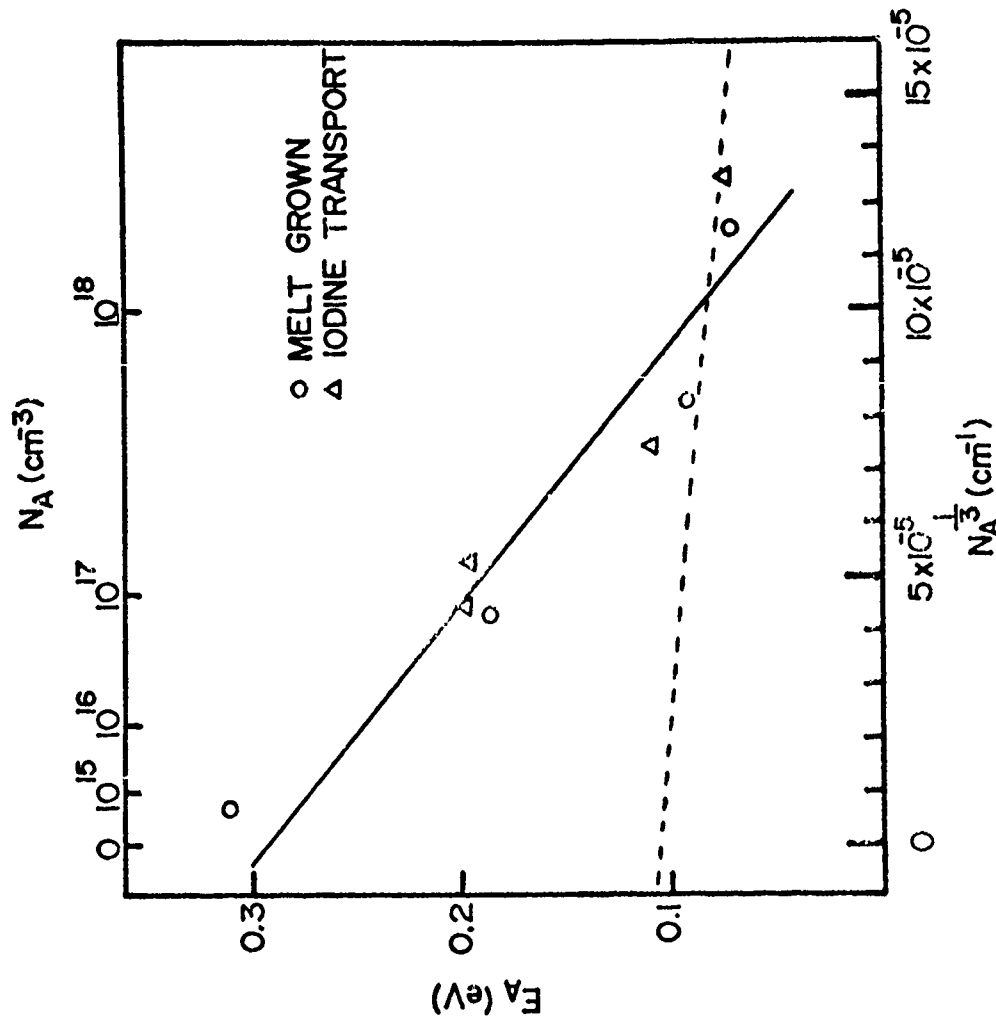


Figure 40. The acceptor ionization energy vs the cube of acceptor concentration. The dotted line is fitted for the lower activation energies than the hydrogenic acceptor level (~ 0.12 eV) with $\beta = 2.4 \times 10^{-8}$ eV cm as discussed in text.

C. Mobility

Figure 41 summarizes the variation of mobility with temperature as obtained from R_H/ρ . Most of the samples measured show almost the same values and same temperature dependence.

Several scattering processes should be taken into account for the analysis of hole mobility in p-CuGaS₂ on the basis of the experimental mobility. The temperature dependence of the mobility up to ~110 °K varies approximately at $T^{-1.5}$. The expression for scattering by acoustic phonons leads to a mobility

$$\mu_L = 2(2\pi)^{1/2} e\hbar^{-4} \rho C^2 / 3(m^*)^{5/2} (kT)^{3/2} E_1^2 \quad (\text{Ref. 94}) \quad (15)$$

where $\rho = 4.45 \text{ g/cm}^3$ is the density,⁹⁵ $C \sim 3 \times 10^5 \text{ cm/sec}$ is the longitudinal velocity of sound⁹⁶ estimated from the other I-III-VI₂ material. The volume deformation potential E_1 is generally estimated from the expression $E_1 \approx (1/\kappa)(\partial E_g / \partial p)$, where κ is the volume compressibility and $(\partial E_g / \partial p)$ is the coefficient for the pressure dependence of the energy gap. The values⁹⁷ of $(\partial E_g / \partial p)$ for II-IV-V₂ compounds were measured and compared to those of III-V compounds which are the binary analogs of II-IV-V₂ compounds. Their values $[(7 - 10) \times 10^{-6} \text{ eV/bar}]$ are similar to those of the closest III-V analogs⁶⁸ with direct gaps. The pressure coefficient⁹⁸ of ZnS is $\sim 7 \times 10^{-6} \text{ eV/bar}$. The compressibility of CuGaS₂ can be assumed to be $\sim 10^{-6} \text{ bar}^{-1}$. These values give $\sim 7 \text{ eV}$ as a deformation potential constant in CuGaS₂. The experimental data for the sample No. 166 and IAS are shown in Figs. 42 and 43. These samples were chosen because they presented maximum and minimum heat-treated samples in our experiment. The calculated

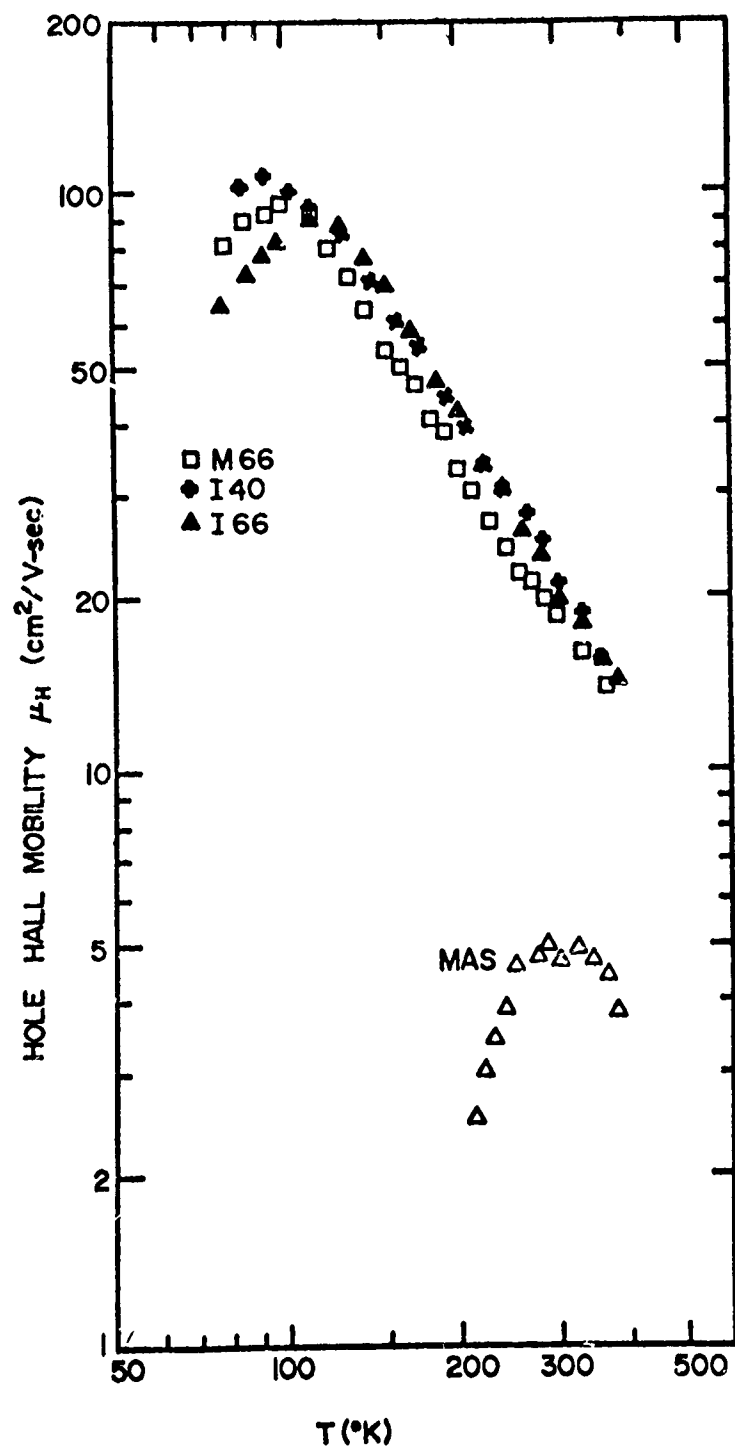


Figure 41. The temperature dependence of the experimental Hall mobility for selected samples.

mobilities μ_L are shown as solid lines in Figs. 42 and 43. The best-fitted value to experimental mobility was $E_1 = 17$ eV with $m^* = 0.69 m_e$. There are some discrepancies between the fitted and estimated values of E_1 ; however, the experimental mobility shows $\sim T^{-1.5}$ dependence. It appears that a dominant scattering mechanism at higher temperature than $\sim 110^{\circ}\text{K}$ is lattice scattering through a deformation potential.

To determine the role of ionized and neutral impurity scattering, and space-charge scattering in limiting lower-temperature mobility, their mobilities were considered. Ionized and neutral impurity scattering usually have their greatest influence on mobility at lower temperature. For scattering by ionized impurity, the mobility is given by the Brooks-Herring formula,⁹⁹

$$\mu_I = 2^{7/2} \epsilon^2 (kT)^{3/2} / [(\pi)^{3/2} e^3 (m^*)^{1/2} N_I g(x)] \quad (16)$$

where $N_I = p + 2N_D$, $g(x) = \ln(1 + Z) - Z/(1 + Z)$, $Z = 6 \epsilon m^* (kT)^2 / (\pi e^2 \hbar^2 p^*)$, and $p^* = p + (p + N_D) [1 - (p + N_D/N_A)]$.

The expression for neutral impurity scattering was given by Erginsoy.¹⁰⁰

$$\mu_N = m^* e^3 / (20eN_N \hbar^3), \quad (17)$$

where $N_N = (N_A - N_D) - p$. The mobilities were calculated with $\epsilon = 8.5$ and N_A and N_D obtained from the Hall data analysis.

The scattering due to the large space-charge region due to local inhomogeneity was proposed by Weisberg.¹⁰¹ The mobility with space-charge scattering is given by

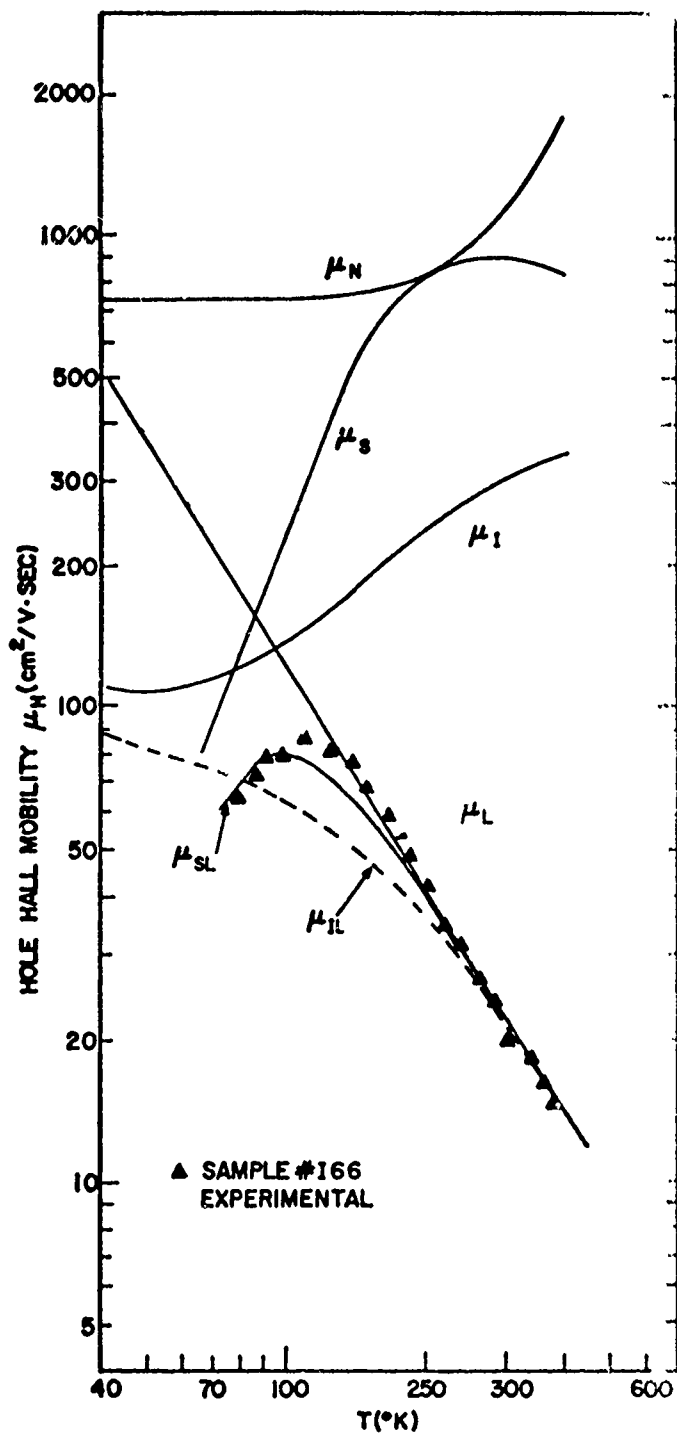


Figure 42. The Hall mobility vs temperature for the sample No. 166 with various scattering mechanisms, $N_A = 2.4 \times 10^{18} \text{ cm}^{-3}$ and $N_D = 4.2 \times 10^{17} \text{ cm}^{-3}$.

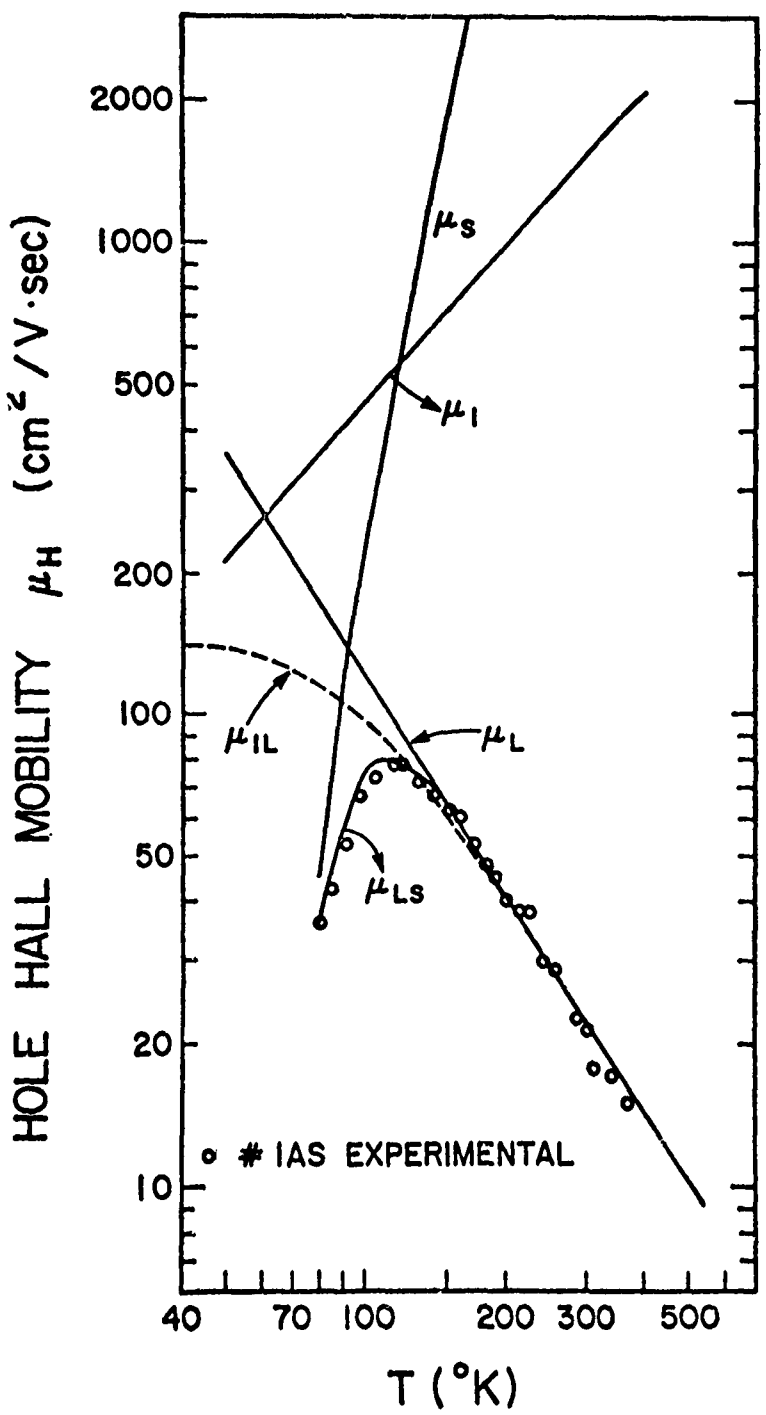


Figure 43. The Hall mobility vs temperature for the sample No. IAS with various scattering mechanisms, $N_A = 1.4 \times 10^{17} \text{ cm}^{-3}$ and $N_D = 6.8 \times 10^{16} \text{ cm}^{-3}$.

$$\mu_s = A(F/p_{300})^{1/3} (T/300)^{-5/6}, \quad (18)$$

where A is a constant which contains the space-charged effective radius, concentration, and numerical constants, and p_{300} is the hole concentration at 300 °K.

The mobility for the different mechanisms has been combined by the usual expression,

$$1/\mu = \sum 1/\mu_i. \quad (19)$$

The combined mobility μ_{IL} , taking into account both acoustical phonon and ionized scattering, is shown in Figs. 42 and 43. It does not explain well the mobility at lower temperature than ~100 °K. The observed mobility rises more rapidly with temperature than the $T^{3/2}$ law predicts. The space-charge scattering mobility was also combined with the lattice mobility. The numerical constant A was fitted to experimental data for the combined mobility μ_{LS} . The values of A were 9×10^2 for sample No. I66 and 2×10^4 for samples No. IAS. The combined mobility μ_{LS} provides a rather good fit, as indicated in Figs. 42 and 43, but it would be desirable to extend the mobility data for a better understanding at lower temperatures.

The mobility of the melt-as-grown sample shows an unusual behavior in comparison with the other samples. The mobility rapidly decreases from room temperature. The room-temperature mobility is $5 \text{ cm}^2/\text{V sec}$, while the other samples show $\sim 20 \text{ cm}^2/\text{V sec}$. This reduction of mobility may be attributed to the confinement of the carriers in states of lower mobility due to the heavy compensation.

3. ELECTRICAL PROPERTIES¹⁰² OF AgGaS₂

As-grown crystals grown either from the melt or by vapor transport exhibited semi-insulating behavior. Although Hall-effect measurements have shown most samples to have p-type conductivity, it was difficult to determine the conductivity type for some crystals due to experimental limitation (mobility $< 0.5 \text{ cm}^2/\text{V sec}$). This may be explained by sample inhomogeneity which occurred during the crystal growth process. However, the crystal resistance was approximately the same over the temperature range 300-380 °K. The activation energy deduced from the reciprocal-temperature-vs-resistivity curve was ~0.72 eV. Values of resistivity, hole concentration, and mobility for a typical as-grown sample grown from the melt are shown in Fig. 44, together with the data for the successive heat treatment of the same sample in vacuum and sulfur. The crystals grown by vapor transport showed similar electrical characteristics. The nature of this deep acceptor level is not clear at present, but it is well known that the intrinsic defects in II-VI compounds strongly influence the electrical characteristics. The deep level in p-type AgGaS₂ may be due to the presence of Ag vacancies.

Heat-treatment in vacuum at the temperatures 700-900 °C for 24-48 h resulted in a change of the conductivity type. All vacuum heat-treated samples showed n-type conductivity and measurable mobility in the temperature range 300-380 °K. The activation energy determined from the resistivity curve was ~0.70 eV. The crystal resistance, however, remained almost the same as for the as-grown

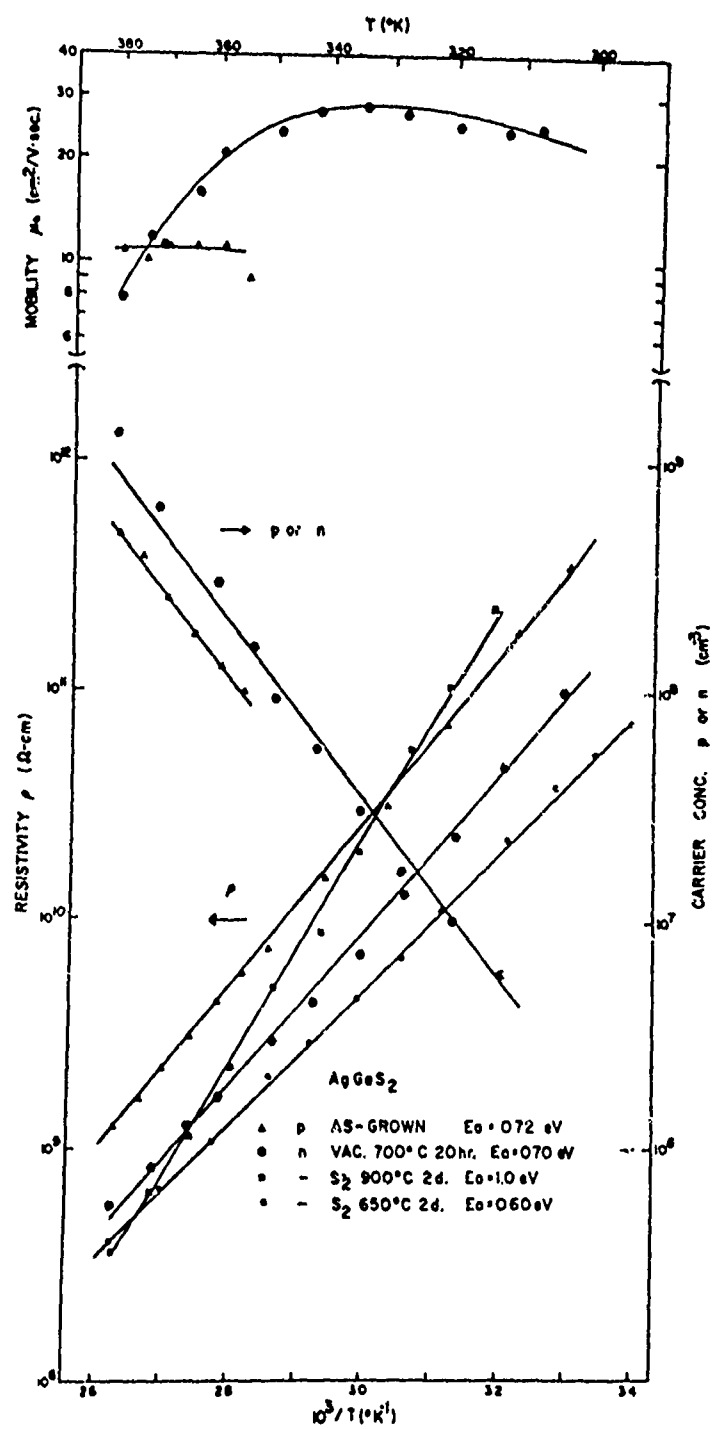


Figure 44. Resistivity, carrier concentration, and mobility as a function of reciprocal temperature for a typical as-grown p-type $AgGaS_2$ specimen. The electrical parameters were also measured on the same specimen subsequent to vacuum annealing and sulfur baking.

crystals. Heat-treatment under sulfur pressure was done in the temperature range 500-900 °C for 24-48 h for the as-grown p-type crystals in an attempt to produce high conductivity p-type and vacuum-baked n-type crystals in order to convert from n to p-type.

The resistivity remained almost the same before and after heat-treatment. Determination of conductivity type was sometimes difficult because of the low mobility ($<0.5 \text{ m}^2/\text{V sec}$) encountered.

In certain p-type crystals, shallow acceptor levels were observed in addition to the deep levels as described above. Observation of shallow levels in the crystal is difficult when strong compensation occurs between a deep donor level and two acceptor levels. In Fig. 45 the resistivity versus reciprocal temperature of an as-grown AgGaS_2 crystal grown from the melt is plotted. The activation energy determined from the curve is ~0.11 eV. The curve also shows the deep level along with this shallow level. The conductivity type of the shallow level was observed to be p-type at ~150 °K (mobility, $2-5 \text{ cm}^2/\text{V sec}$), even though determination of the conductivity type at room temperature was difficult because of low mobilities. This clearly shows that a shallow acceptor level exists together with the deep p-type level in AgGaS_2 . The shallow level was observed usually in homogeneous clear melt-grown samples; it remains even after heat treatment in vacuum at 700 °C for 20 h and is due either to impurities or defects.

4. P-TYPE CONDUCTION¹⁰³ IN UNDOPED ZnSe

P-type conduction in undoped ZnSe is discussed in this section. All the samples were heat-treated in Se atmosphere about 24 h at 700-900 °C.

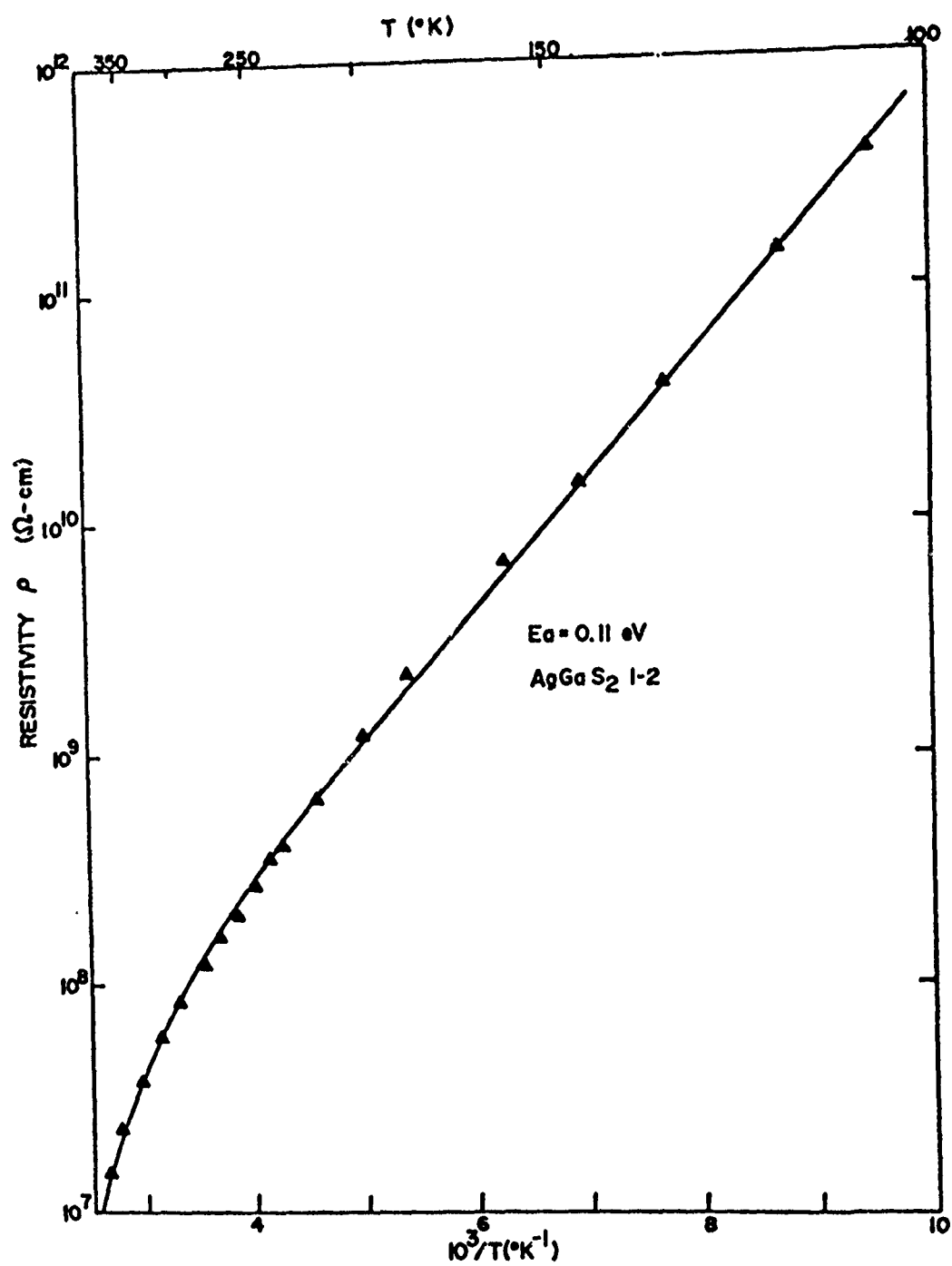


Figure 45. Resistivity as a function of reciprocal temperature for p-type as-grown AgGaS_2 grown from the melt having a shallow acceptor level.

The undoped crystals before the heat treatment showed n-type conduction. The resistivity was $10^{10} - 10^{12} \Omega \text{ cm}$ and the carrier concentration was $\leq 10^7 \text{ cm}^{-3}$ in the temperature range $320-380^\circ\text{K}$. The activation energy deduced from the resistivity versus the inverse of temperature is 0.92 eV from the bottom of the conduction band as shown in Fig. 46. No shallow level corresponding to the known n-type dopants was observed from these crystals in this temperature range. The deep n-type level may be due to an intrinsic defect in ZnSe, possibly the Se vacancy.

All the samples prepared under the vapor heat treatment showed p-type conduction in the observed temperatures.

Figure 47 shows the hole concentration and the resistivity of one sample heat treated at 700°C over the temperature range $250-380^\circ\text{K}$. Mobilities were $21-30 \text{ cm}^2/\text{V sec}$, as shown in Fig. 48. The hall data were analyzed using Eq. 11. The parameters involved are shown in Fig. 47.

The activation energy was obtained from several samples. Their values were 0.65-0.75 eV from the valence band edge, as shown in Fig. 49. Most samples show only such deep levels. However, in some samples we were able to observe shallow acceptor levels in addition to the deep level. Figure 50 shows the resistivity as a function of temperatures of two samples. The slope of the curves yields two activation energies, 0.66 and 0.15 eV for sample No. 2, and 0.71 and ~ 0.098 eV for sample No. 3. These shallow energy levels were also observed from the temperature dependence of photoconductivity in temperature ranges lower than

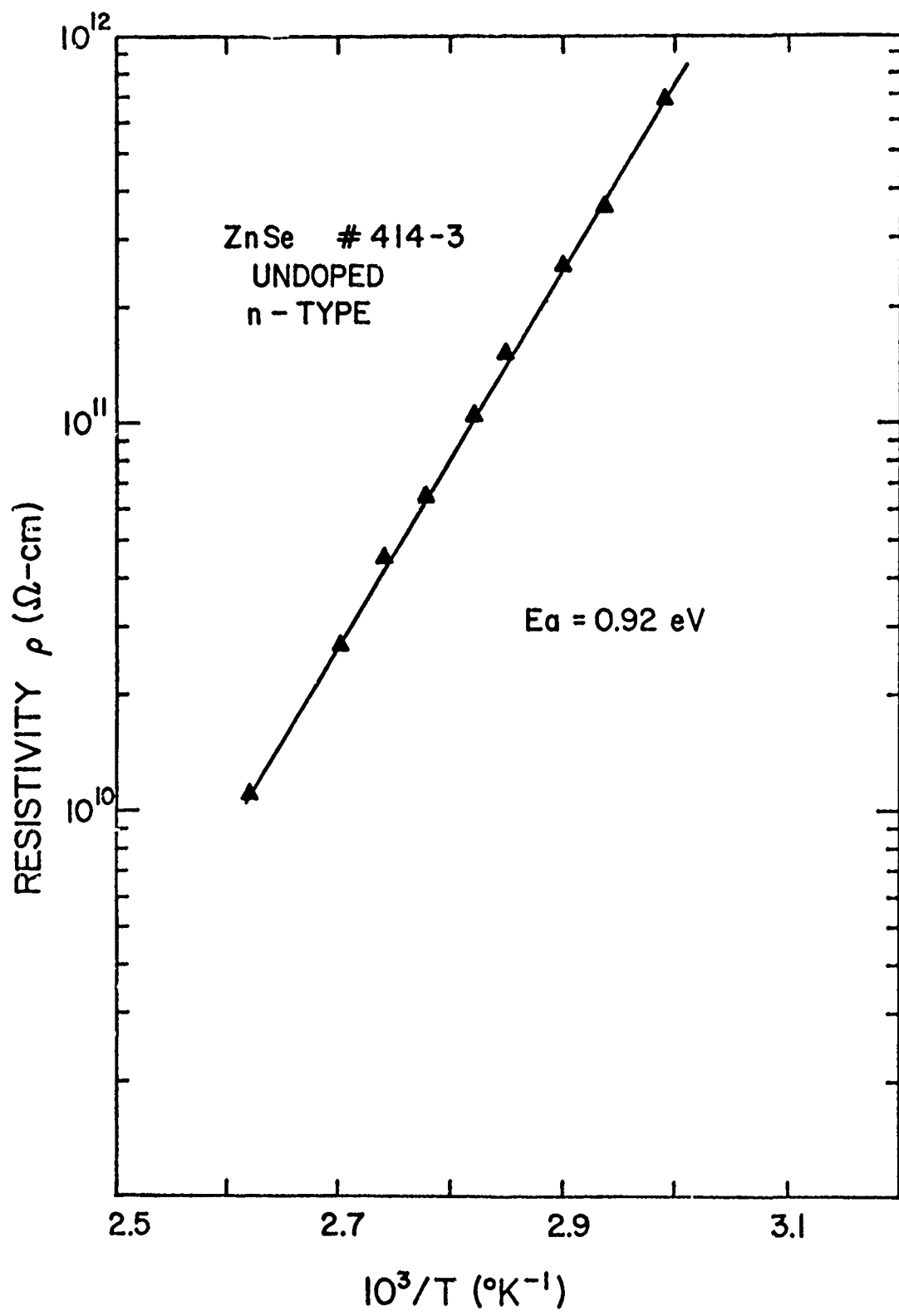


Figure 46. Resistivity vs the inverse of temperature for a n-type sample before the heat-treatment.

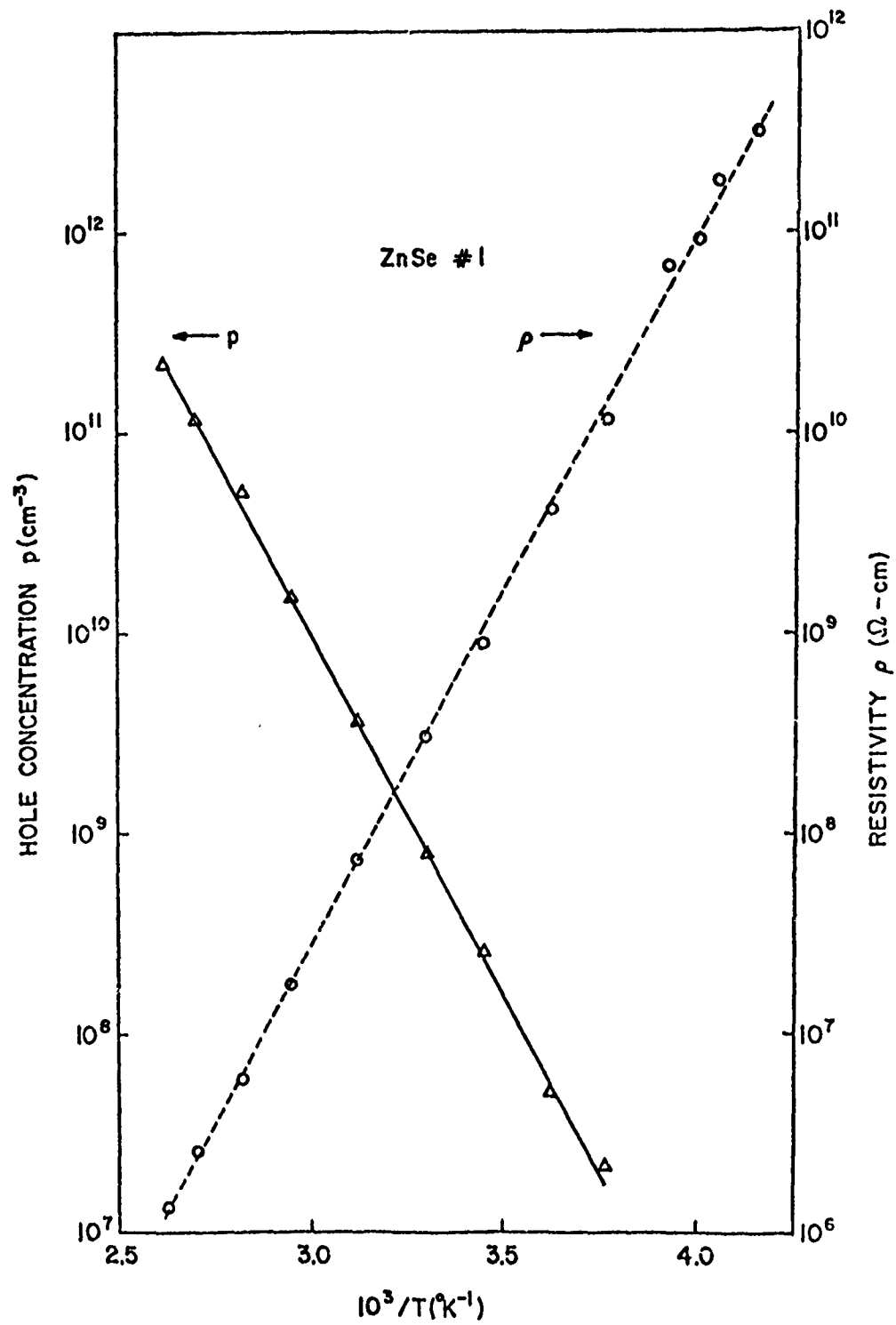


Figure 47. Hole concentration and resistivity vs the inverse of temperature for sample No. 1. The solid line shows the fitted values with $E_A = 0.67 \text{ eV}$, $N_A = 3.7 \times 10^{15} \text{ cm}^{-3}$, $N_D = 1.3 \times 10^{14} \text{ cm}^{-3}$, and $N_V/g = 7.2 \times 10^{14}$.

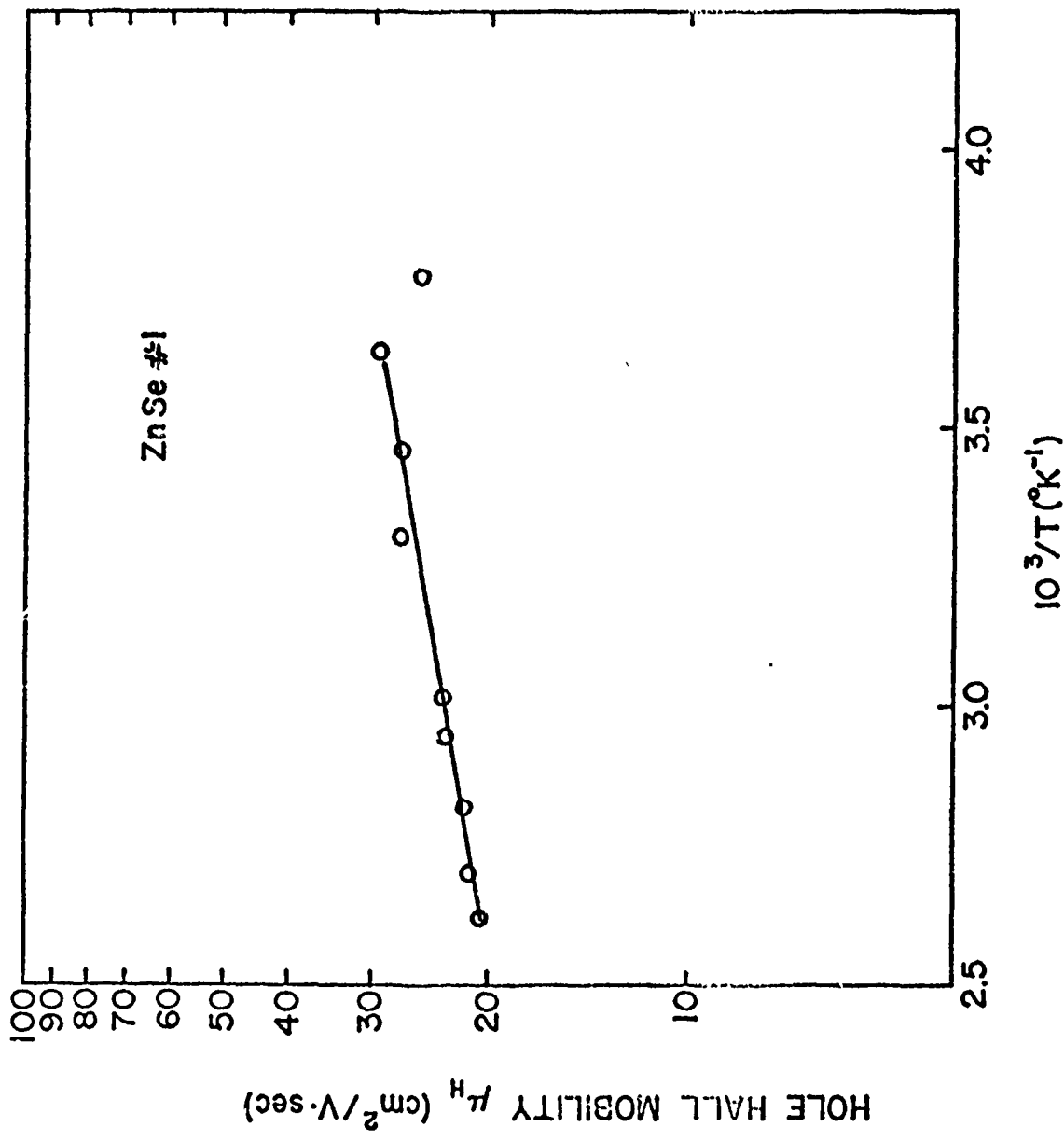


Figure 48. Hole Hall mobility vs the inverse of temperature after the heat treatment.

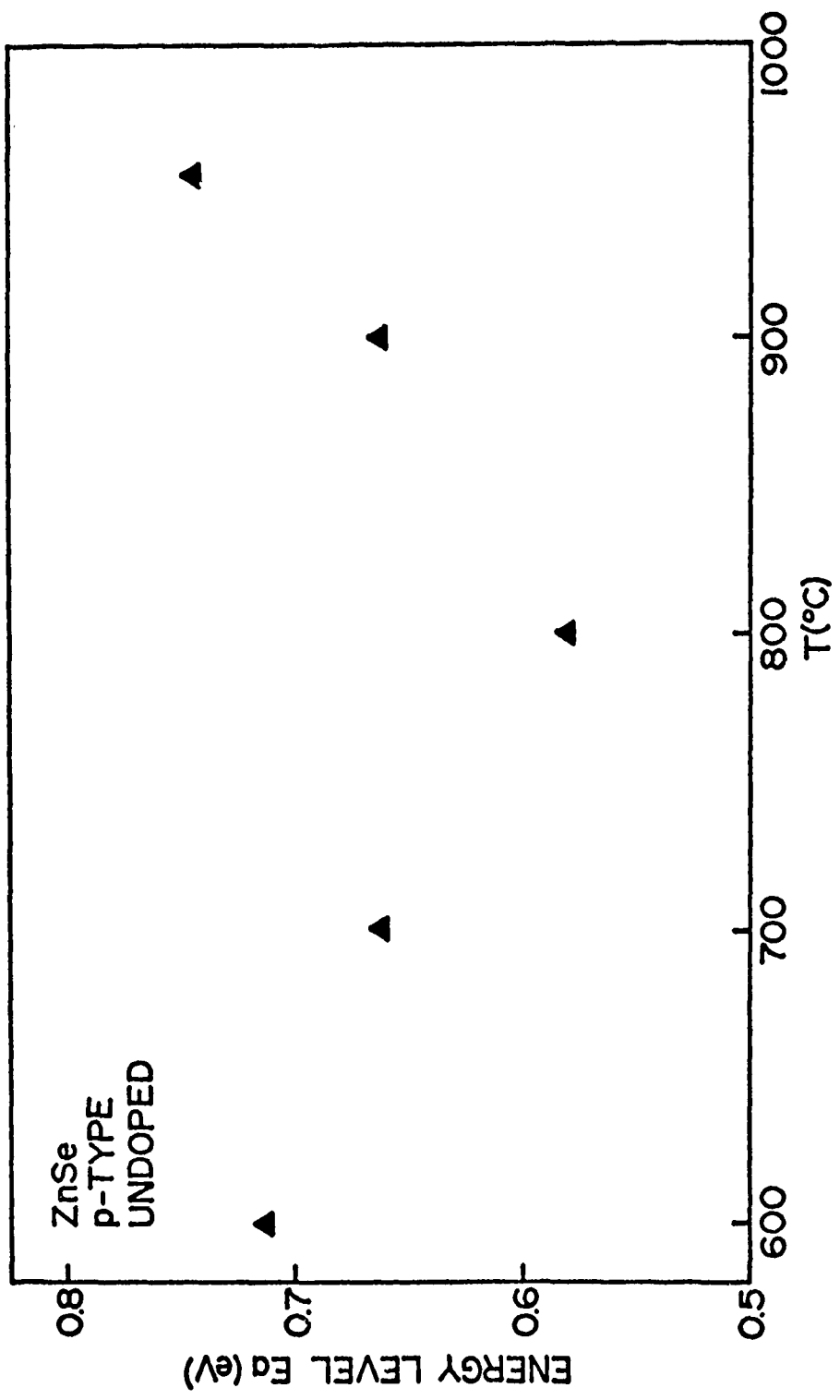


Figure 49. Acceptor level vs the heat treating temperature.

250 °K. The photoconductivity was excited by less-than-band-gap radiation. The origin of the shallow levels is not clear at present. P-type conduction in the undoped ZnSe crystals is dominated by the deep acceptor level. The energy level was observed to change depending upon the heat treatment temperature. The hole concentration and resistivity were also dependent on the temperature. The acceptor energies obtained so far from p-type ZnSe crystals containing the possible p-type dopants¹⁰⁴⁻¹⁰⁷ are in the same range of values as obtained from the present work for undoped p-type ZnSe crystals. The heat treatment with Se vapor will enhance uncompensated acceptors by filling in the possible Se vacancies acting as deep donors, which were observed from the as-grown undoped samples. Double heat treatment under Zn vapor and then Se vapor brought the increase of the resistivity compared with the crystal baked with Se vapor only. Therefore, we believe that the deep acceptor level, which was observed in the present work and the other works, could be due to intrinsic defects in ZnSe-i.e., zinc vacancy or zinc vacancy complexes.

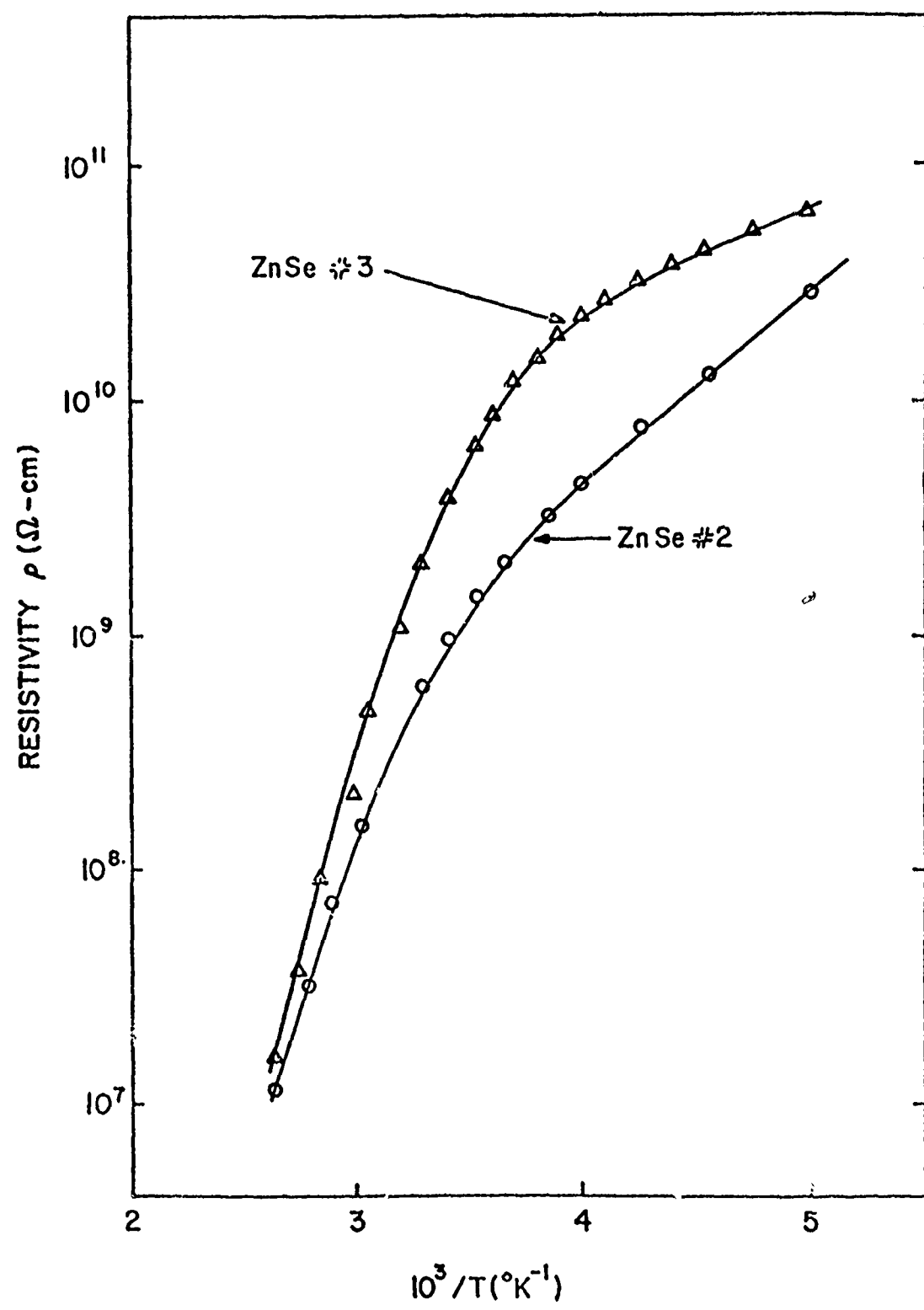


Figure 50. Resistivity vs the inverse of temperature for samples Nos. 2 and 3.

APPENDIX A

COMPUTER PROGRAM; POWDER DIFFRACTION PATTERNS

```
10 DIM S(500), T(500), Z(500), H(500), K(500), L(500)
15 PRINT "WHICH COMPOUND IS THIS CALCULATION FOR";
16 PRINT "[1=CU; 2=AG; 3=AL; 4=GA; 5=IN; 6=TL; 7=S; 8=SE; 9=TE]";
17 INPUT E1, E2, E3
20 PRINT "WHAT ARE THE TETRAGONAL LATTICE PARAMETERS, A AND C";
30 INPUT A0, C0
40 PRINT
50 A9=1/(A0*A0)
60 C9=1/(C0*C0)
70 PRINT "WHAT RADIATION IS TO BE USED (1=CU KAL, 2=CR KAL)";
80 INPUT L8
85 PRINT
90 IF L8=2 THEN 120
100 L9=1.54051
110 GO TO 130
120 L9=2.2896
130 N=0
140 FOR K=0 TO 9
150 FOR H=0 TO 9
160 FOR L=0 TO 15
170 IF K>H THEN 1340
180 IF H+K+L=0 THEN 1330
190 IF (H+K+L)/2<>INT((H+K+L)/2) THEN 1330
200 IF H<>0 THEN 230
210 IF (K+L)/2<>INT((K+L)/2) THEN 1330
220 GO TO 330
230 IF H<>K THEN 300
240 IF L=0 THEN 280
250 IF 1/2<>INT(L/2) THEN 1330
260 IF ((2*H+L)/4)<>INT((2*H+L)/4) THEN 1330
270 GO TO 330
280 IF H/2<>INT(H/2) THEN 1330
290 GO TO 330
300 IF (K+L)=0 THEN 320
310 GO TO 330
320 IF H/2<>INT(H/2) THEN 1330
330 E=(H*H+K*K)*A9+L*L*C9
340 IF E<.08 THEN 1330
350 IF E>1.68 THEN 1330
360 D=SQR(1/E)
370 T=ATN(L9/SQR(4*D*D-L9*L9))
380 L1=(1+COS(2*T)*COS(2*T))/(SIN(T)*SIN(T)*COS(T))
390 IF H=0 THEN 510
400 IF H=K THEN 460
410 IF L=0 THEN 440
420 P=16
430 GO TO 580
440 P=8
450 GO TO 580
460 IF L=0 THEN 490
470 P=8
480 GO TO 580
```

```

490 P=4
500 GO TO 580
510 IF L<>0 THEN 540
520 P=4
530 GO TO 580
540 IF K=0 THEN 570
550 P=8
560 GO TO 580
570 P=2
580 S=1/(2*D)
590 S2=S*S
600 S3=S↑3
610 S4=S↑4
620 S5=S↑5
630 S6=S↑6
640 G1=27.9891+5.00657*S-314.25*S2+965.242*S3-1227.49*S4+575.907*S5
650 G2=45.9971+5.53287*S-441.104*S2+1348*S3-1723.7*S4+816.772*S5
660 G3=10.137-46.18*S+1012.8*S2-8117.8*S3+28203*S4-44460*S5+26004*S6
670 G4=27.9886+2.82056*S-174.435*S2+325.422*S3-185.38*S4
680 G5=46.0648-5.10809*S-411.575*S2+1361.48*S3-1842.11*S4+913.218*S5
690 G6=78.075-.327835*S-382.913*S2-734.793*S3-434.098*S4
700 G7=17.9845+12.1897*S-693.793*S2+3513.84*S3-7713.74*S4+7973.47*S5
710 G8=36.0346-3.04855*S-430.229*S2+1608.57*S3-2365.67*S4+1231.26*S5
720 G9=54.0678-5.38379*S-455.475*S2-1485.7*S3-1995.38*S4+985.072*S5
730 IF E1=2 THEN 760
740 F1=G1
750 GO TO 770
760 F1=G2
770 IF E2>4 THEN 830
780 IF E2=4 THEN 810
790 F2=G3
800 GO TO 870
810 F2=G4
820 GO TO 870
830 IF E2=6 THEN 860
840 F2=G5
850 GO TO 870
860 F2=G6
870 IF E3>8 THEN 930
880 IF E3=8 THEN 910
890 F3=G7
900 GO TO 940
910 F3=G8
920 GO TO 940
930 F3=G9
940 P0=3.14159
950 P2=3.14159/2
960 P4=3.14159/4
970 X0=(2*H+L)*P2
980 X1=(2*K+3*L)*P2
990 X2=(H+K)*P0
1000 X3=L*P0
1010 X4=(2*H+3*L)*P2
1020 X5=(2*K+L)*P2
1030 X6=(2*(H+K)+L)*P4
1040 X7=(6*(H+K)+L)*P4
1050 X8=(6*H+2*K+3*L)*P4

```

```

1060 X9=(2*H+6*K+3*L)*P4
1070 Y0=(2*(H+K)+5*L)*P4
1080 Y1=(6*(H+K)+5*L)*P4
1090 Y2=(6*I+2*K+7*L)*P4
1100 Y3=(2*I+6*K+7*L)*P4
1110 A1=F1*(2+COS(X0)+COS(X1))
1120 A2=F2*(COS(X2)+COS(X3)+COS(X4)+COS(X5))
1130 A3=F3*(COS(X6)+COS(X7)+COS(X8)+COS(X9))
1140 A4=F3*(COS(Y0)+COS(Y1)+COS(Y2)+COS(Y3))
1150 A5=A3+A4
1160 A=A1+A2+A5
1170 B1=F1*(SIN(X0)+SIN(X1))
1180 B2=F2*(SIN(X2)+SIN(X3)+SIN(X4)+SIN(X5))
1190 B3=F3*(SIN(X6)+SIN(X7)+SIN(X8)+SIN(X9))
1200 B4=F3*(SIN(Y0)+SIN(Y1)+SIN(Y2)+SIN(Y3))
1210 B5=B3+B4
1220 B=B1+B2+B5
1230 F=SQR(A*A+B*B)
1240 Z=F*F*P*L1
1250 N=N+1
1260 I=N
1270 S(I)=E
1280 T(I)=D
1290 Z(I)=Z
1300 H(I)=H
1310 K(I)=K
1320 L(I)=L
1330 NEXT L
1340 NEXT H
1350 NEXT K
1360 FOR I=1 TO N-1
1370 FOR J=I+1 TO N
1380 IF S(I)<=S(J) THEN 1570
1390 X=S(I)
1400 X1=H(I)
1410 X2=K(I)
1420 X3=L(I)
1430 X4=T(I)
1440 X5=Z(I)
1450 S(I)=S(J)
1460 H(I)=H(J)
1470 K(I)=K(J)
1480 L(I)=L(J)
1490 T(I)=T(J)
1500 Z(I)=Z(J)
1510 S(J)=X
1520 H(J)=X1
1530 K(J)=X2
1540 L(J)=X3
1550 T(J)=X4
1560 Z(J)=X5
1570 NEXT J
1580 NEXT I

```

```
1590 PRINT " H  K  L      1/D*D      D(H,K,L)      INTENSITY
1600 FOR I=1 TO N
1610 S(I)=INT(S(I)*1E4+.5)/1E4
1620 T(I)=INT(T(I)*1E4+.5)/1E4
1630 Z(I)=INT(Z(I)*.01)
1640 Q=INT((Z(I)/Z(1))*1E3)/10
1650 PRINT H(I); K(I); L(I), S(I),T(I), Z(I),Q
1660 NEXT I
1670 PRINT
1680 PRINT "ARE THERE NEW LATTICE PARAMENTERS";
1690 INPUT A$
1700 IF A$="YES" THEN 20
1710 END
*
```

APPENDIX B

CALCULATED POWDER X-RAY DIFFRACTION PATTERN FOR CuGaS₂

WHICH COMPOUND IS THIS CALCULATION FOR
[1=CU; 2=AG; 3=AL; 4=GA; 5=IN; 6=TL; 7=S; 8=SE; 9=TE]

? 1, 4, 7
WHAT ARE THE TETRAGONAL LATTICE PARAMETERS, A AND C? 5.351, 10.484

WHAT RADIATION IS TO BE USED (1=CU KAL, 2=CR KAL)?1

H	K	L	1/D*D	D(H,K,L)	INTENSITY	I/10
1	1	2	.1062	3.068	110506	100
1	0	3	.1168	2.9259	58	0
2	0	0	.1397	2.6755	16721	15.1
0	0	4	.1456	2.621	3989	3.6
2	0	2	.1761	2.383	0	0
2	1	1	.1837	2.333	50	0
2	1	3	.2565	1.9745	39	0
1	0	5	.2624	1.9523	38	0
2	2	0	.2794	1.8919	21972	19.8
2	0	4	.2853	1.8723	84878	76.8
3	0	1	.3234	1.7584	30	0
0	0	6	.3275	1.7473	0	0
3	1	0	.3492	1.6921	0	0
3	1	2	.3856	1.6103	29192	26.4
3	0	3	.3962	1.5887	21	0
1	1	6	.3974	1.5863	13855	12.5
2	1	5	.4021	1.5771	21	0
2	2	4	.425	1.534	3136	2.8
3	2	1	.4631	1.4694	16	0
2	0	6	.4672	1.463	0	0
1	0	7	.4807	1.4423	15	0
3	1	4	.4948	1.4216	0	0
3	2	3	.5359	1.366	12	0
3	0	5	.5418	1.3586	11	0
4	0	0	.5588	1.3377	13536	12.2
0	0	8	.5823	1.3105	3163	2.8
4	0	2	.5952	1.2962	0	0
4	1	1	.6028	1.288	9	0
2	1	7	.6204	1.2696	8	0
3	3	2	.665	1.2262	5772	5.2
4	1	3	.6756	1.2166	7	0
3	1	6	.6768	1.2156	11236	10.1
3	2	5	.6815	1.2114	6	0
4	2	0	.6985	1.1965	1169	1
4	0	4	.7044	1.1915	2302	2
2	0	8	.722	1.1769	2201	1.9

4	2	2	.7349	1.1665	0	0
3	0	7	.7601	1.147	5	0
1	0	9	.7719	1.1382	5	0
4	1	5	.8212	1.1035	4	0
4	2	4	.8441	1.0885	14968	13.5
2	2	8	.8617	1.0773	7324	6.6
5	0	1	.8822	1.0647	4	0
4	3	1	.8822	1.0647	4	0
4	0	6	.8863	1.0622	0	0
3	2	7	.8998	1.0542	3	0
5	1	0	.908	1.0494	0	0
0	0	10	.9098	1.0484	0	0
2	1	9	.9116	1.0474	3	0
3	1	8	.9315	1.0361	0	0
5	1	2	.9444	1.029	7511	6.7
5	0	3	.955	1.0233	3	0
4	3	3	.955	1.0233	3	0
3	3	6	.9562	1.0227	3722	3.3
1	1	10	.9796	1.0103	3665	3.3
5	2	1	1.0219	.9892	3	0
4	2	6	1.026	.9872	0	0
4	1	7	1.0395	.9808	3	0
2	0	10	1.0495	.9761	0	0
3	0	9	1.0513	.9753	3	0
5	1	4	1.0536	.9742	0	0
5	2	3	1.0947	.9558	3	0
5	0	5	1.1006	.9532	3	0
4	3	5	1.1006	.9532	3	0
4	4	0	1.1176	.9459	3195	2.8
1	0	11	1.1358	.9383	3	0
4	0	8	1.1411	.9361	12823	11.6
5	3	0	1.1874	.9177	0	0
3	2	9	1.191	.9163	4	0
5	3	2	1.2238	.9039	7325	6.6
5	1	6	1.2356	.8996	7377	6.6
5	2	5	1.2403	.8979	4	0
6	0	0	1.2573	.8918	715	.6

3	1	0	1.259	.8912	7499	6.7
4	4	4	1.2632	.8898	718	.6
2	1	11	1.2755	.8854	4	0
4	2	8	1.2808	.8836	1454	1.3
6	0	2	1.2937	.8792	0	0
6	1	6	1.3013	.8766	4	0
0	0	12	1.301	.8737	186	.1
5	0	7	1.3189	.8707	5	0
4	3	7	1.3189	.8707	5	0
4	1	9	1.3307	.8669	5	0
5	3	4	1.333	.8661	0	0
6	1	3	1.3741	.8531	5	0
6	2	0	1.397	.8461	7948	7.1
6	0	4	1.4028	.8443	16046	14.5
3	0	11	1.4152	.8406	6	0
6	2	2	1.4334	.8353	0	0
5	4	1	1.441	.833	7	0
2	0	12	1.4498	.8305	17489	15.8
5	2	7	1.4586	.828	7	0
4	0	10	1.4686	.8252	0	0
5	1	8	1.4903	.8191	0	0
5	4	3	1.5138	.8128	9	0
5	3	6	1.515	.8125	11316	10.2
6	1	5	1.5197	.8112	9	0
3	3	10	1.5384	.8062	6094	5.5
6	2	4	1.5425	.8052	2298	2
3	2	11	1.5549	.802	10	0
1	0	13	1.5725	.7975	11	0
6	3	1	1.5807	.7954	12	0
6	0	6	1.5848	.7943	0	0
2	2	12	1.5895	.7932	1398	1.2
4	2	10	1.6083	.7885	0	0
4	3	9	1.6101	.7881	15	0
5	0	9	1.6101	.7881	15	0
6	3	3	1.6535	.7777	23	0
5	4	5	1.6594	.7763	26	0
3	1	12	1.6594	.7763	0	0

APPENDIX B (cont'd)

CALCULATED POWDER X-RAY DIFFRACTION PATTERN FOR AgGaS₂

WHICH COMPOUND IS THIS CALCULATION FOR
[1=CU; 2=AG; 3=AL; 4=GA; 5=IN; 6=TL; 7=S; 8=SE; 9=TE]

?2,4,7

WHAT ARE THE TETRAGONAL LATTICE PARAMETERS, A AND C? 5.7566, 10.301

WHAT RADIATION IS TO BE USED (1=CU KAL, 2=CR KAL)? 1

H	K	L	1/D*D	D(H,K,L)	INTENSITY	I/10
1	1	2	.098	3.1936	198523	100
1	0	3	.115	2.9489	7261	3.6
2	0	0	.1207	2.8783	52904	26.6
0	0	4	.1508	2.5752	10140	5.1
2	0	2	.1584	2.5126	0	0
2	1	1	.1603	2.4976	4500	2.2
2	1	3	.2357	2.0598	2504	1.2
2	2	0	.2414	2.0353	42709	21.5
1	0	5	.2658	1.9397	2075	1
2	0	4	.2715	1.9192	141117	71
3	0	1	.281	1.8864	1901	.9
3	1	0	.3018	1.8204	0	0
0	0	6	.3393	1.7168	0	0
3	1	2	.3395	1.7163	61188	30.8
3	0	3	.3564	1.6751	1303	.6
2	1	5	.3865	1.6085	1146	.5
2	2	4	.3922	1.5968	9734	4.9
1	1	6	.3996	1.5819	23189	11.6
3	2	1	.4017	1.5778	1078	.5
3	1	4	.4526	1.4865	0	0
2	0	6	.46	1.4745	0	0
3	2	3	.4771	1.4477	823	.4
4	0	0	.4828	1.4391	26843	13.5
1	0	7	.492	1.4257	785	.3
3	0	5	.5072	1.4042	749	.3
4	0	2	.5205	1.3861	0	0
4	1	1	.5224	1.3835	716	.3
3	3	2	.5809	1.3121	12255	6.1
4	1	3	.5978	1.2933	587	.2
0	0	8	.6031	1.2876	4653	2.3
4	2	0	.6035	1.2872	4421	2.2
2	1	7	.6127	1.2776	566	.2
3	2	5	.6279	1.262	547	.2
4	0	4	.6336	1.2563	8104	4
3	1	6	.641	1.249	20892	10.5
4	2	2	.6412	1.2488	0	0
2	0	8	.7238	1.1754	6467	3.2
3	0	7	.7334	1.1677	447	.2
4	1	5	.7486	1.1558	436	.2
4	2	4	.7543	1.1514	26787	13.4
5	0	1	.7638	1.1442	426	.2
4	3	1	.7638	1.1442	426	.2

5	1	0	.7846	1.129	0	0
1	0	9	.7935	1.1226	409	.2
4	0	6	.8221	1.1029	0	0
5	1	2	.8223	1.1028	14734	7.4
5	0	3	.8392	1.0916	386	.1
4	3	3	.8392	1.0916	386	.1
2	2	8	.8446	1.0881	11704	5.8
3	2	7	.8541	1.0821	380	.1
3	3	6	.8824	1.0645	6835	3.4
5	2	1	.8845	1.0633	369	.1
3	1	8	.9049	1.0512	0	0
2	1	9	.9142	1.0459	360	.1
5	1	4	.9354	1.034	0	0
0	0	10	.9424	1.0301	0	0
4	2	6	.9428	1.0299	0	0
5	2	3	.9599	1.0207	349	.1
4	4	0	.9656	1.0176	5224	2.6
4	1	7	.9748	1.0129	346	.1
4	3	5	.99	1.005	344	.1
5	0	5	.99	1.005	344	.1
1	1	10	1.0028	.9986	6231	3.1
5	3	0	1.026	.9872	0	0
3	0	9	1.0349	.983	339	.1
2	0	10	1.0631	.9699	0	0
5	3	2	1.0637	.9696	12226	6.1
4	0	8	1.086	.9596	20072	10.1
6	0	0	1.0864	.9594	2159	1
5	2	5	1.1107	.9489	336	.1
4	4	4	1.1164	.9464	2157	1
5	1	6	1.1239	.9433	12210	6.1
6	0	2	1.124	.9432	0	0
6	1	1	1.126	.9424	337	.1
3	2	9	1.1556	.9302	339	.1
1	0	11	1.1705	.9243	340	.1
5	3	4	1.1768	.9218	0	0
6	1	3	1.2013	.9124	344	.1
4	2	8	1.2067	.9103	4416	2.2
6	2	0	1.2071	.9102	10326	5.2
4	3	7	1.2162	.9068	346	.1
5	0	7	1.2162	.9068	346	.1
6	0	4	1.2371	.8991	21025	10.5
3	1	10	1.2442	.8965	12819	6.4

6	2	2	1.2448	.8963	0	0
5	4	1	1.2467	.8956	352	.1
4	1	9	1.2764	.8851	360	.1
2	1	11	1.2912	.88	364	.1
5	4	3	1.3221	.8697	375	.1
5	2	7	1.3369	.8649	381	.1
6	1	5	1.3521	.86	387	.1
0	0	12	1.3571	.8584	628	.3
6	2	4	1.3578	.8582	5030	2.5
5	3	6	1.3653	.8558	14492	7.2
6	3	1	1.3674	.8552	395	.1
5	1	8	1.3877	.8489	0	0
3	0	11	1.4119	.8416	421	.2
4	0	10	1.4252	.8376	0	0
6	0	6	1.4256	.8375	0	0
6	3	3	1.4428	.8325	444	.2
5	4	5	1.4728	.824	472	.2
2	0	12	1.4778	.8226	29346	14.7
3	3	10	1.4856	.8204	9056	4.5
7	0	1	1.4881	.8198	489	.2
7	1	0	1.5088	.8141	0	0
4	3	9	1.5178	.8117	529	.2
5	0	9	1.5178	.8117	529	.2
3	2	11	1.5326	.8078	553	.2
4	2	10	1.5459	.8043	0	0
6	2	6	1.5463	.8042	0	0
7	1	2	1.5465	.8041	21734	10.9
5	5	2	1.5465	.8041	10866	5.4
7	0	3	1.5635	.7998	619	.3
4	4	8	1.5688	.7984	19618	9.8
6	4	0	1.5692	.7983	4131	2
6	1	7	1.5783	.796	660	.3
6	3	5	1.5935	.7922	713	.3
2	2	12	1.5985	.7909	4779	2.4
6	4	2	1.6069	.7889	0	0
7	2	1	1.6088	.7884	781	.3
1	0	13	1.6229	.785	865	.4
5	3	8	1.6291	.7835	0	0
5	2	9	1.6385	.7812	1000	.5
4	1	11	1.6533	.7777	1211	.6
3	1	12	1.6588	.7764	0	0
7	1	4	1.6596	.7762	0	0

REFERENCES

1. V. A. Chaldyshev and G. F. Karavaev, 12v VUZ. Fiz. 5, 103 (63).
2. A. S. Borschchevskii, N. A. Goyunova, F. P. Kesamanly, D. N. Nosledov, Phys. Stat. Sol. 21, 9 (1967).
3. J. L. Shay, in: Proc. Eleventh Intern. Conf. on the Physics of Semiconductors, Warsaw, 1972 (Polish Scientific Publishers, Warsaw, 1972), p 788.
4. J. L. Shay, E. Buehler, and J. H. Wernick, Phys. Rev. Lett. 24, 1301 (1970).
5. J. E. Rowe and J. L. Shay, Phys. Rev. B3, 451 (1971).
6. J. L. Shay, B. Tell, H. M. Kasper and L. M. Schiavone, Phys. Rev. B5, 5003 (1972).
7. J. L. Shay and H. M. Kasper, Phys. Rev. Lett. 29, 1162 (1972).
8. J. L. Shay and B. Tell, Surface Science 37, 748 (1973).
9. G. D. Boyd, N. M. Kasper, and J. H. McFee, IEEE, J. Quantum Electr. QE-7, 563 (1971).
10. G. D. Boyd, H. M. Kasper, J. H. McFee, and F. G. Storz, IEEE, J. Quantum Electr. QE-8, 900 (1972).
11. D. C. Hanna, V. V. Rampal, and R. C. Smith, Opt. Commun. 8, 151 (1973).
12. R. L. Byer, M. M. Choy, R. L. Herbst, P. S. Chelma, and R. S. Feigelson, Appl. Phys. Lett. 24, 65 (1974).
13. S. W. Wagner, J. L. Shay, B. Tell and H. M. Kasper, Appl. Phys. Lett. 22, 351 (1973).

14. S. Wagner, J. L. Shay, and P. Migliorato, and H. M. Kasper, Appl. Phys. Lett. 25, 434 (1974).
15. P. Migliorato, B. Tell, J. L. Shay, and H. M. Kasper, 24, 227 (1974).
16. J. L. Shay, S. Wagner and H. M. Kasper, Appl. Phys. Lett. 27, 89 (1975).
17. P. W. Yu, S. P. Faile, and Y. S. Park, Appl. Phys. Lett. 26, 384 (1975).
18. P. W. Yu, Y. S. Park, S. P. Faile, and J. E. Ehret, Appl. Phys. Lett. 26, 717 (1975).
19. P. M. Bridenbaugh and P. Migliorato, Appl. Phys. Lett. 26, 459 (1975).
20. W. N. Honeyman, J. Phys. Chem. Solids 30, 1935 (1969).
21. H. M. Kasper, Solid State Chemistry, Proceeding of the 5th Materials Research Symposium, July 1972, p 671.
22. W. N. Honeyman and K. H. Wilkinson, J. Phys. D: 4, 1182 (1971).
23. N. Yamanoto and T. Miyachi, Jap. J. Appl. Phys. 11, 1383 (1972).
24. L. S. Lerner, J. Phys. Chem. Solids, 27, 1 (1966).
25. V. P. Zhuze, V. M. Sergeeva, and E. L. Shtrum, Soviet Phys Tech. Phys. 3 (10), 1925 (1958).
26. J. G. Austin, C. H. L. Goodman and A. E. Pengelly, J. Electrochem. Soc. 103, 609 (1956).
27. J. Sapriel, Appl. Phys. Lett. 19, 533 (1971).
28. J. Sapriel, L. Rivollan, and J. L. Ribet, J. de Physique, 33, c6-150 (1972).

29. J. Sapriel and R. Lancon, Proc. IEEE, 61, 678 (1973).
30. R. Zallen, in II-VI Semiconducting Compounds, edited by D. G. Thomas (Benjamin, New York, 1967), p 877.
31. D. R. Hamilton, Brit. J. Appl. Phys. 9, 103 (1958).
32. D. C. Reynolds and S. J. Czyzack, Phys. Rev. 79, 543 (1950).
33. W. D. Harken, J. Chem. Phys., 10, 628 (1942).
34. O. J. Curtis, J. Appl. Phys. 33, 2461 (1962).
35. E. H. Carlson, J. Cryst. Growth, 1, 271 (1967).
36. M. M. Kreitman, S. P. Faile, C. W. Litton, and D. C. Reynolds, in the 1975 issue of the Proceedings of the Conference on "Optical Properties of Highly Transparent Solids", editors, S. S. Mitra and E. Bendow, Plenum Press.
37. K. E. Spear, J. Chem. Ed. 49, 81 (1972).
38. S. P. Faile and P. W. Yu, Bull. Am. Phys. Soc., 19, 821 (1974).
39. T. Ohmiya, J. Appl. Cryst. 7, 396, 1974.
40. Y. Toudic and R. Aumont, J. Cryst. Growth, 10, 170 (1971).
41. P. W. Yu, W. J. Anderson, and Y. S. Park, Sol. State Commun. 13, 1883 (1973).
42. D. G. Thomas and J. J. Hopfield, Phys. Rev. 116, 573 (1959).
43. J. L. Shay, E. Buehler, and J. H. Wernick, Phys. Rev. B2, 4104 (1970).
44. L. A. Feldkamp, G. Venkataraman, and J. S. King, Solid State Commun. 7, 157 (1969).

45. D. Long, Energy Bands in Semiconductors, p 50FF, Interscience, New York, (1968).
46. F. Bassani, B. S. Knox and V. B. Fowler, Phys. Rev. 137A, 1217 (1965).
47. J. L. Shay, B. Tell, H. M. Kasper, and L. M. Schavone, Phys. Rev. B7, 4485 (1973).
48. R. G. Wheeler and J. O. Dimmock, Phys. Rev. 125, 1805 (1962).
49. B. Segall and D. T. F. Marples, in Physics and Chemistry of II-VI Compounds, edited by M. Avens and J. S. Prener (Wiley-Interscience, New York, 1967), p 335.
50. P. W. Yu and Y. S. Park, J. Appl. Phys. 45, 823 (1974).
51. J. L. Merz, Phys. Rev. 176, 961 (1968).
52. T. N. Morgan, B. Welber, and R. N. Bhargava, Phys. Rev. 166, 751 (1968).
53. R. E. Nahory, J. Shah, R. C. C. Leite, E. Euehler, and J. H. Wernick, Phys. Rev. B1, 4677 (1970).
54. G. D. Holah, Opt. Commun. 5, 10 (1972).
55. W. J. Anderson P. W. Yu and Y. S. Park, Opt. Commun. 11, 392 (1974).
56. M. V. Hobden, Acta. Cryst. A24, 676 (1968).
57. C. Schwartz, D. S. Chemla, B. Ayrault and R. C. Smith, Opt. Commun. 5, 244 (1972).
58. P. W. Yu, to be published in Solid State Commun.
59. See, for example, J. J. Hopfield, D. G. Thomas, and M. Gershenson, Phys. Rev. Lett. 10, 162 (1963).
60. K. Maeda, J. Phys. Chem. Solids. 26, 595 (1965).

61. J. L. Merz and R. T. Lynch, *J. Appl Phys.* 39, 1988 (1968).
62. E. W. Williams, A. Ashford, P. Porteous and A. M. White, *Solid State Commun.* 8, 501 (1970).
63. R. Dingle, *Phys. Rev.* 84, 788 (1969).
64. P. J. Dean and J. L. Merz, *Phys. Rev.* 178, 1310 (1969).
65. R. C. T. Leite, *Phys. Rev.* 157, 672 (1967).
66. T. N. Morgan, *Phys. Rev.* 139, A343 (1965).
67. B. I. Shklovskii and A. L. Efros, *Sov. Phys. -JETP* 33, 468 (1971).
68. J. Parkes, R. D. Tomlin, and M. J. Hampshire, *Solid-State Electron.* 16, 773 (1973).
69. R. D. Tomlinson, E. Elliot, J. Parkes, and M. J. Hampshire, *Appl. Phys. Lett.* 26, 3836 (1975).
70. H. H. Woodbury, Physics and Chemistry of II-VI Compounds, edited by H. Aven and J. S. Prener (North-Holland, Amsterdam, 1967), pp 223-264.
71. For instance, see M. A. Lampert, R. B. Schilling, R. Baron, and J. W. Mayer, in Semiconductors and Semimetals, Vol. 6, edited by R. K. Williardson and A. C. Beer (Academic, New York 1970), pp 1-96, 201-313.
72. R. J. Smith, *Atomic Energy Research Establishment Report*, No. R6660, 1971 (Unpublished).
73. N. Laegreid and G. K. Wehner, *J. Appl. Phys.* 32, 365 (1961).
74. T. Itoh and Y. Kushira, *J. Appl. Phys.* 42, 5120 (1971).
75. S. Mayburg and J. Black, *J. Appl. Phys.* 34, 1521 (1963).
76. H. J. Stocker, *Solid State Commun.* 16, 525 (1975).

77. C. H. Gooch, C. Hilsum and B. R. Holeman, *J. Appl. Phys.* 32, 2069 (1961).
78. W. J. Turner, C. D. Petit and N. G. Ainslie, *J. Appl. Phys.* 34, 3274 (1963).
79. C. H. Henry and D. V. Lang, Proc. 12th Int. Conf. Phys. Semicond. Stuttgart, 1974.
80. A. T. Govelemov, B. V. Tsaremkov, and N. G. Chiabrishvili *Sov. Phys. - Semicond.*, 5, 95 (1971).
81. J. L. T. Waugh and G. Dalling, *Phys. Rev.* 132, 2410 (1963).
82. S. P. Gaur, J. F. Vetelino and S. S. Mitra, *J. Phys. Chem. Solids* 32, 2737 (1971).
83. E. F. Gross, V. I. Safarov, V. E. Sedov and V. A. Maruschak, *Sov. Phys. - Solid State* 11, 277 (1969).
84. The Deutsch Company, Banning Calif., Model DM5606-3719 receptacle and RS07-37195-059 plug.
85. Heli-tran Dewar is available commercially from Air Products and Chemical, Inc.
86. P. W. Yu, D. L. Dowling and Y. S. Park, *J. Appl. Phys.* 45, 5287 (1974).
87. B. Tell and H. M. Kasper, *J. Appl. Phys.* 44, 4988 (1973).
88. F. A. Kroger, The Chemistry of Imperfect Crystals, (North-Holland, Amsterdam, 1964).
89. G. L. Pearson and J. Bardeen, *Phys. Rev.* 75, 865 (1949).
90. P. Debye and E. M. Conwell, *Phys. Rev.* 93, 693 (1954).
91. P. Norton and H. Levinstein, *Phys. Rev.* B6, 470 (1972).
92. J. Boars and W. H. Koschel, *Solid State Commun.* 11, 1513 (1972).

93. I. S. Shlimak and V. V. Emtzev, Phys. Status Solid. B 47, 325 (1971).
94. J. Bardeen and W. Shockley, Phys. Rev. 80, 72 (1950).
95. S. C. Abrahams and J. L. Bernstein, J. Chem. Phys. 52, 5415 (1973).
96. L. I. Berger and A. E. Balaneuskaya, Inorg. Mater. 2, 1294 (1966).
97. R. Bendorius, N. D. Prochukhan, and A. Sileika, Phys. Status Solid B53, 745 (1972).
98. D. L. Camphusen, G. A. N. Connell, and W. Paul, Phys. Rev. Lett. 26, 184 (1971).
99. F. J. Blatt, Solid State Physics, 4, 344 (1957).
100. C. Erginsoy, Phys. Rev. 79, 1013 (1950).
101. L. R. Weisberg, J. Appl. Phys. 33, 1817 (1964).
102. P. W. Yu, J. Manthuruthil, and Y. S. Park, J. Appl. Phys. 45, 3694 (1974).
103. P. W. Yu and Y. S. Park, Appl. Phys. Lett. 32, 345 (1973).
104. J. H. Haeanstra and J. Dielman, Electrochem. Soc. Ext. Abstr. 14, 2 (1965).
105. G. B. Stringfellow and R. H. Bube, Phys. Rev. 171, 903 (1968).
106. A. R. Reinberg, W. C. Holton, M. de Wit and R. K. Watts, Phys. Rev. B3, 410 (1971).
107. Y. S. Park, P. M. Hemenger and C. H. Chung, Appl. Phys. Lett. 18, 45 (1971).

BIBLIOGRAPHY

1. P. W. Yu and Y. S. Park, "p-type Conduction in Undoped ZnSe", *Appl. Phys. Lett.* 22, 345 (1973).
2. P. W. Yu, W. J. Anderson, "Anomalous Temperature Dependence of the Energy Gap of AgGaS_2 ", *Solid State Commun.* 13, 1883 (1973).
3. P. W. Yu and Y. S. Park, "Sharp Line and Broad-band Emission in AgGaS_2 Crystals", *J. Appl. Phys.* 45, 820 (1974).
4. P. W. Yu, J. Manthuruthil and Y. S. Park, "Some Electrical Properties of AgGaS_2 ", *J. Appl. Phys.* 45 3694 (1974).
5. W. J. Anderson, P. W. Yu and Y. S. Park, "Optical Rotary Dispersion of AgGaS_2 ", *Opt. Commun.* 11, 3924 (1974).
6. P. W. Yu, D. L. Downing and Y. S. Park, "Electrical Properties of CuGaS_2 Single Crystals", *J. Appl. Phys.* 45, 5283 (1974).
7. P. W. Yu, S. P. Faile and Y. S. Park, "Cadmium-diffused CuInSe_2 Junction Diode and Photovoltaic Detection", *Appl. Phys. Lett.* 26, 384 (1975).
8. H. J. Stocker, "Probable Observation of Unusual Vibrational Modes in the Oscillatory Photoconductivity of Semiinsulating GaAs", *Solid State Commun.* 16, 525 (1975).
9. P. W. Yu, Y. S. Park, S. P. Faile, and J. E. Ehret", "Electroluminescence and Photovoltaic Detection in Cd-implanted CuInSe_2 p-n Junction Diode", *Appl. Phys. Lett.* 26, 717 (1975).

10. M. M. Kreitman, S. P. Faile, C. W. Litton and D. C. Reynolds, "Optical Transmission in Iodine Transported α -HgS", in 1975 Issue of the Proceedings of the Conference on "Optical Properties of Highly Transparent Solids", editors; S. S. Mitra and E. Bendow, Plenum Press.
11. Phil Won Yu, Y. S. Park, and J. T. Grant, "Electroluminescence in Br, Cl, and Zn Implanted CuInSe₂ p-n Junction Diodes", Appl. Phys. Letters, 28, 214 (1976).
12. Phil Won Yu, "Radiative Recombination in Melt-Grown and Cd-Implanted CuInSe₂", J. Appl. Phys. 47, 677 (1976).
13. Phil Won Yu, "Evidence for a Donor-Acceptor Pair Band in CuInSe₂", Solid State Commun., 18, 395 (1976).